Realistic Frequency Coded Chipless RFID: Physically Modulated Tags and Refectarray Readers

Von Der Fakultät für Ingenieurwissenschaften,
Abteilung Elektrotechnik und Informationstechnik
der Universität Duisburg-Essen

zur Erlangung des akademischen Grades

Doktor der Ingenieurwissenschaften (Dr.-Ing.)

genehmigte Dissertation

von

Maher Ahmed

aus

Kalyobiya, Egypt

Gutachter:
Erster Gutachter: Prof. Dr.-Ing. Thomas Kaiser
Zweiter Gutachter: Prof. Dr.-Ing. Klaus Solbach

Tag der mündlichen Prüfung
13.12.2016

Fachgebiet Digitale Signalverarbeitung (DSV)
Universität Duisburg-Essen
Bismarckstrasse 81
47057 Duisburg
Germany
Tel.: +49 (203) 3 79-32 87
Fax : +49 (203) 3 78-34 98

Referent: Prof. Dr.-Ing. Thomas Kaiser
Co-Referent: Prof. Dr.-Ing. Klaus Solbach
Vorsitzende: Univ. Prof. Dr.-Ing. habil. I. Erlich
Tag der Promotion: 13.12.2016

Mit Unterstützung des Deutschen
Akademischen Austauschdienstes

ACKNOWLEDGMENT

First and foremost, praises and thanks to the God Almighty for all blessings. He always give me the power to believe in myself and pursue my dreams. This thesis would not have been possible without the faith i have in you, the Almighty.

I would like to express my sincere gratitude to my supervisor Prof. Dr.-Ing. Thomas Kaiser, for his encouragement, creative suggestions, enormous knowledge, and patience through the course of my doctoral research. I can only call myself lucky to be one of his Ph.D. students. I appreciate all his contributions of time, ideas, and funding to make my own Ph.D. Therefore, i solemnly submit my honest and humble thanks to him for bringing my dreams into reality.

I am also thankful to Prof. Dr.-Ing. Klaus Solbach, for being my second supervisor, for his insightful comments, and for keeping his office door always open whenever I needed his support.

My deepest (heartfelt) appreciation goes to Prof. Hadia Elhennawy – Ain Shams University, Egypt for her generous support, constructive comments, and warm encouragement.

I have great pleasure in acknowledging my research group at DSV, and our group leader Dr.-Ing. Mohamed El-Hadidy for his insightful guidance and appreciated support. I am especially thankful to the group members (Abdelfattah Fawky and Ahmed El-Awamry) who have contributed immensely to my personality. The group has been a source of friendships as well as good advice and collaboration.

I take pride in acknowledging all DSV members particularly Sabine Jankowski, Marc Hoffman, and Rolf Küppers. They have supported me with their individual skills and abilities, helping me to acheive my goals.

There are no words to express my love and gratitude towards the most important person in my life, my wife Noura and our kids. Thank you for being always beside me, without you, there would be no meaning to any of this.

I am speechless! I can barely find words to express all the wisdom, love and support given me for that I am eternally grateful to my beloved parents for their unconditional love, and

endurance. They had always been my well wishers, prayers and constant enthusiasm.

My heartfelt gratitude to my brother Ahmed and sisters Zeinab and Asmaa for their great support and love.

I would also like to express my gratitude to the German Academic Exchange Service - Deutscher Akademischer Austausch-Dienst - (DAAD) for their financial support to pursue my Ph.D. degree.

There are so many others whom I may have inadvertently left out and I sincerely thank all of them for their help.

Maher Ahmed
Duisburg, Germany
November, 2017

ABSTRACT

Recently, the chipless Radio Frequency Identification (RFID) technology has attracted tremendous attention in the market of item identification where the cost is the main concern. However, up to date the technology is at the conceptual level and suffers from a lot of limitations that hinder the technology deployment. The chipless RFID system comprises three major parts which are the reader circuit, the interrogation antennas, and the chipless tags. The contributions of this dissertation are to overcome the challenges that impede the deployment of the chipless RFID system from the perspective of innovating physically modulated tags and developing the reader antenna system. In particular, the system is considered in three novel aspects.

The first aspect is the linear physically modulated tags where the tag is interrogated by Ultra Wideband (UWB) signal and the tag inscribed metallic resonators are physically modulating the interrogation frequencies. Therefore, the UWB waveform is modulated in the form of resonant notches, and/or peaks that are inherently embedded in the tag backscattered Radar Cross Section (RCS) frequency response. In this regard, four innovative physically modulated tags are developed aiming at enhancing the coding efficiency, maximizing the coding capacity, conserving the operating frequency range and preserving the tag size. The first tag is based on nested circular ring resonators where each resonator codifies a tag coding notch. Therefore, the tag structure is scalable, printable and compact size. Moreover, a novel encoding methodology is employed to preserve the notch width and position while coding. The second developed tag is a depolarizing one where the polarization isolation between the reader interrogation signal and the tag response is utilized to minimize the environmental clutter reflections. Furthermore, the tag is scalable, printable, and compact size in the credit card format. Thirdly, a novel Notch Width Modulation (NWM) tag is introduced where the tag-ID is not only based on the notch position but also on the notch width. Hence, the notch width configures a further dimension to increase the Degree of Freedom (DoF) for coding and modulation. Therefore, the notch width and position are modulated simultaneously aiming at enhancing the coding efficiency and capacity. Lastly, a novel On Off-Notch/Peak (OO-N/P) and Notch/Peak-Position (N/P-P)

modulation tag is introduced. The tag basic idea is to exploit both the co-polarized and cross-polarized backscattered signals from a tag excited with a linear polarized wave. Consequently, the tag signature is encoded into Notch/Peak (N/P) format in two orthogonal planes. Thus, the Co/Cross-polarizing N/P modulation scheme presents a novel criterion for enhancing the coding efficiency and capacity of the chipless RFID systems. Moreover, the cross-polarized response enhances the tag detection in a realistic environment. The proposed tags and their associated physical modulation schemes are validated using Electro Magnetic (EM) simulations and real-world testbed measurements.

In the second aspect, the Reflectarray (RA) antenna is proposed to be utilized in the reader side aiming at increasing the reading range, minimizing the environmental reflections, and acquiring a lot of novel capabilities that can not be provided by the conventional antenna arrays. The spatial feeding RA antenna is easily integrated with the RF circuits, lightweight, conformal geometry, and low cost. Hence, in this concern, three different novel designs are developed. The first design utilizes the Log Periodic Array (LPDA) antenna to feed the developed RA surface. This introduced prototype operates at 5.8 GHz and achieves 300 MHz bandwidth. Moreover, the RA antenna radiation beam is 4 times narrower than the feeder beam and thus 6 dB higher in gain with -10 dB Side Lobe Level (SLL). The second developed prototype uses a constant phase center horn antenna to feed the RA surface. Thus, an UWB RA antenna enabling multiple bits accommodation is designed. This antenna operates from 4 GHz to 6 GHz with 15° Half Power Beam Width (HPBW), 19 dBi gain, and -10 dB SLL. Furthermore, this developed UWB RA antenna is successfully integrated with the physically modulated tags and a reading range of 1 m is achieved. To the best of my knowledge, this is the highest reading range achieved in the Frequency Coded (FC) chipless RFID systems, considering real-world indoor environment and software defined radio reader. After that, dual-polarized RA antenna with low cross-polarization level is presented. This RA antenna is proposed to be utilized with the Co/Cross-polarizing tags. Finally, a successful implementation of an electronic beam steering RA antenna is introduced. This novel beam steering RA antenna system enhances the reading robustness and can precisely locate the chipless tags. In this concern, a novel unit cell that is able to electronically control the reflected phase at different discrete frequencies utilizing a single varactor diode is proposed. Therefore, a scanning range of $\pm 50°$ is achieved. Moreover, the steered beams are 4 times narrower than the feeder beam and thus 4 times higher in gain.

In the third aspect, the nonlinear physically modulated tags are proposed. The core functionality relies on interrogating the tag with a prescribed set and format of frequencies

in a time regulated technique while the tag replies with its unique ID at other frequencies. Therefore, the nonlinearity is exploited to completely isolate the environmental clutter reflections, get rid of the necessary reference calibration measurements, overcome the detuning caused by the tagged item materials, and increase the coverage. These objectives are attained by exploiting the nonlinearity generated from a single unbiased diode integrated with the tag structure. The first proposed tag category relies on exploiting the second order nonlinear terms. Therefore, in this regard, three novel tags are introduced. The first class is the single tone harmonic radar tags. In this class, the reader scans the available tags by sending specific fundamental tones. Then, the tag receiving antenna is tuned at only one of these fundamentals which is maximally conveyed to the nonlinear device for generating the corresponding harmonics. Consequently, the tag transmitting antenna is tuned at the second harmonic which is retransmitted back towards the reader representing the tag-ID. Thus, the narrower is the band-pass filter provided by the tag receiving antenna or integrated into it, the more the frequencies that can be utilized for coding. After that, the multi-tone interrogation is proposed to increase the coding capacity. Hence, the tag is interrogated with a prescribed set of fundamentals that are swept over the time to avoid the generation of the mixing products in the reader and tag as well. The tag in turn which is completely planar based on the Coplanar Waveguide (CPW) technology implements a Notch Position Modulation (NPM) scheme in the second harmonics of these fundamental tones. Therefore, the notches that are existing in the second harmonic response symbolize the tag-ID. Afterward, the simultaneous multi-tone interrogation is explored. In this concern, a set of distinct frequency pairs are used to interrogate the nonlinear tags. As a consequence, these tones are mixed through the nonlinear device. Consequently, the tag transmitting antenna figures out only one of these mixed products. The second proposed tag category relies on exploiting the inter-modulation communication principle which exhibits a small frequency span. Therefore, the tag is illuminated by two co-located frequencies and respond at an inter-modulated frequency which is retransmitted by the tag transmitting antenna representing the tag-ID. Finally, the phase encoding capability is proposed. Therefore, not only the existence or the non-existence of a harmonic notch or peak used in coding the tag-ID but also the corresponding relative phase states can be considered. The introduced tags and their associated physical modulation schemes are verified using harmonic balance analysis, EM simulations and realistic testbed measurements.

Lastly, the unique features which are considered in the dissertation bring a significant enhancement to the deployment of the chipless RFID system.

ZUSAMMENFASSUNG

In letzter Zeit hat die chiplose RFID Technologie enorme Aufmerksamkeit im besonders kostenbewussten Markt für Objektidentifikation erregt. Allerdings befindet sich der aktuelle Stand der Technik auf einem konzeptionellen Niveau und leidet noch unter einer Menge Einschränkungen, die eine sofortige Verwendung der Technologie noch verhindern. Grundsätzlich lässt sich ein chiploses RFID System in drei Teile unterteilen, dem RFID Lesegerät, den verwendeten Antennen und dem RFID Tag. Der Beitrag der vorliegenden Dissertation zur Überwindung der erwähnten Einschränkungen liegt in innovativen physikalisch modulierenden RFID Tags und in der Weiterentwicklung des Antennensystems des RFID Lesegerätes. Dabei werden besonders die drei im Folgenden beschriebenen Aspekte betrachtet.

Der erste Aspekt beschäftigt sich mit physikalisch linear modulierten RFID Tags. Dabei werden die RFID Tags mit einem Ultra Breitband (engl. ultra wideband, UWB) Signal bestrahlt und die auf dem RFID Tag aufgebrachten Resonatoren modulieren die Frequenz des Signals physikalisch. Dabei werden dem UWB Signal resonante Notches und/oder Peaks aufmoduliert, die sich in der Frequenzantwort des von der effektiven Rückstrahlfläche (engl. radar cross section, RCS) zurückgestrahlten Signals befindet. Hierfür sind vier innovative physikalisch modulierende RFID Tags, mit dem Ziel einer effektiveren Kodierung und maximalen Kodierungstiefe bei gleichbleibender Frequenzauslastung und RFID Tag Größe, entwickelt worden. Der erste RFID Tag besteht aus ineinander verschachtelten Ringresonatoren, wobei jeder Resonator ein Notch, also ein Bit, erzeugt. Der zweite RFID Tag arbeitet auf zwei unterschiedlichen Polarisationsebenen für empfangene und rückgestrahlte Signale. Dadurch kann die Streustrahlung der Umgebung leichter herausgefiltert werden. Beide Strukturen sind skalierbar, druckbar und kompakt. Als drittes wird ein neuartiger Notchbreiten modulierender (engl. notch width modulation, NWM) RFID Tag eingeführt. Dabei ist die ID des RFID Tags nicht nur über die Notchlage im Frequenzbereich sondern auch über die Notchbreite definiert. Die Notchbreite stellt also eine zusätzliche Dimension bereit, die die Freiheitsgrade (engl. degree of Freedom, DoF) für Kodierung und Modulation erhöhen, was wiederum die kodier

Effektivität und Codetiefe verbessert. Als letztes wird ein neuartiger On Off-Notch/Peak (OONP) und Notch/Peak-Position (N/P-P) modulierender RFID Tag eingeführt. Die Idee dahinter ist, sowohl das kopolarisierte als auch das kreuzpolarisierte Rückstrahl Signal eines mit einer linear-polarisierten Welle angeregten RFID Tags auszunutzen. Dies bittet ein weiteres Kriterium um sowohl kodier Effektivität als auch Codetiefe des chiplosen RFID Systems weiter zu verbessern. Gleichzeitig verbessert die kreuzpolarisierte Antwort auch wieder die Detektion des RFID Tags in einer realen Umgebung. Alle vorgeschlagenen RFID Tags und Modulationsschemata sind mit elektromagnetischen (EM) Simulationen und in einer realen Testumgebung überprüft worden.

Der zweite Aspekt dieser Arbeit schlägt Reflect-Array Antennen (RA) für das RFID Lesegerät mit dem Ziel vor, die Lesereichweite zu erhöhen und die Reflektionen an der Umgebung zu minimieren. Das RA bietet dabei im Vergleich zu herkömmlichen Phased-Array-Antennen eine Menge weiterer Eigenschaften. Das RA ist einfach zu integrieren, von geringem Gewicht, hat eine sehr geometrische Anordnung und ist preiswert, um nur einige zu nennen. Insgesamt wurden drei neuartige RA Aufbauten entwickelt. Als erstes wurde eine logarithmisch periodische Antenne (engl. log periodic antenna array, LPDA) als Primärstrahler für die entworfene RA Oberfläche genutzt. Der Prototype arbeitet bei 5.8 GHz und erreicht eine Bandbreite von 300 MHz. Außerdem ist der erzeugte Antennenstrahl viermal schmaler als der Primärstrahl und erreicht somit einen um 6 dB höheren Antennengewinn bei einem Nebenkeulenpegel (engl. side lobe level, SSL) von -10 dB. Für den zweiten Prototypen wird ein selbstentwickelter Hornstrahler mit konstanter Phase als Primärstrahler für die RA Oberfläche verwendet. Durch diese Anordnung wird ein UWB RA realisiert, mit dem mehrere Bits gleichzeitig ausgelesen werden können. Die Antenne arbeitet zwischen $4-6$ GHz und erreicht einen Öffnungswinkel (engl. half power beam width, HPBW) von 15° bei 19 dBi Antennengewinn und -10 dB SLL. Im Zusammenspiel mit den physikalisch modulierenden RFID Tags konnte mit diesem UWB RA eine Lesereichweite von 1 m erzielt werden, was nach meinem Kenntnisstand die größte bisher für ein chiploses frequenzkodiertes (engl. frequency coded, FC) RFID System erreichte Lesereichweite in einer realen Innenraum Umgebung darstellt. Weiter wird eine dual polarisierte RA Antenne mit geringem Kreuzpolarisations Pegel vorgestellt. Es wird vorgeschlagen diese Antenne mit den ko-/kreuzpolarisierten RFID Tags zu verwenden. Als letztes wird eine RA Antenne mit elektronischer Strahlsteuerung eingeführt, die die Stabilität des Lesevorgangs weiter erhöht und eine präzise Ortung der chiplosen RFID Tags ermöglicht. Dazu wird eine Zelle vorgeschlagen, die mit Hilfe einer Varaktordiode in der Lage ist, für einzelne Frequenzen die Phase des reflektierten Signals elektronisch zu steuern. Ein Scanbereich von $\pm 50°$ kann damit

abgedeckt werden.

Als dritter Aspekt werden nicht-lineare physikalisch modulierende RFID Tags vorgeschlagen. Hier ist der Kerngedanke, dass der RFID Tag seine ID mit einer anderen Frequenz zurückstrahlt als die mit der er selber angestrahlt wird. Durch dieses nichtlineare Verhalten wird die Umgebungsstrahlung komplett ausgeblendet, die sonst unumgänglichen Kalibrierungsmessungen werden überflüssig, das Problem der Verstimmung durch das RFID Tag Material wird umgangen und die Abdeckung wird erhöht. Die Nicht-Linearität wird durch eine einzige in die Struktur des RFID Tags integrierte Diode erzeugt. Zunächst werden RFID Tags vorgeschlagen, die mit Nichtlinearitäten zweiter Ordnung arbeiten. Für diese Kategorie werden drei unterschiedliche RFID Tags entworfen. Als Erstes ein Einzelton harmonischer RFID Radar Tag. In dieser Klasse strahlt das RFID Lesegerät einige spezifische Grundtöne aus, die schmalbandige Empfangsantenne des RFID Tags ist auf einen Grundton abgestimmt, den sie an die Diode weiterleitet. Die hier generierte zweite Harmonische wird von der entsprechend konfigurierten Sendeantenne der RFID Tags zurückgestrahlt. Dabei gilt, je schmaler der Bandbassfilter, desto mehr Frequenzen können zur Kodierung genutzt werden. Um die Codekapazität zu erhöhen werden als nächsten Mehrfrequenzabfragen vorgestellt. Dazu werden am RFID Lesegerät nacheinander, um keine Mischprodukte entstehen zu lassen, vordefinierte Frequenzen durchlaufen. Auf dem RFID Tag können jetzt mehrere ID Bits wieder durch die unterschiedlichen Frequenzen der jeweiligen zweiten Harmonischen erzeugt werden (engl. Notch Position Modulation, NPM). Anschließend werden festdefinierte Frequenzpaare zum Auslesen der ID verwendet. Die Diode mischt beide Frequenzen und antwortet nur auf der Mischfrequenz eines der Frequenzpaare. In einer weiteren Kategorie werden die Intermodulationseigenschaften der dritten Ordnung ausgenutzt, mit dem Vorteil, dass nur ein relativ geringer Frequenzbereich benötigt wird. Hierbei wir der RFID Tag mit zwei benachbarten Frequenzen bestrahlt und die zurückgestrahlte Intermodulationsfrequenz stellt die ID des RFID Tags dar. Schließlich wird die Kodierung über die Phaseninformation vorgestellt. Zusätzlich zur Existenz oder Fehlen eines Peaks oder Notches wird der dazugehörige relative Phasenzustand zur Kodierung herangezogen. Alle vorgestellten RFID Tags und ihre Modulation werden an Hand von Harmonische-Balance-Analyse, EM Simulationen und Messungen in einer realen Testumgebung überprüft.

Zum Schluss lässt sich sagen, die einzigartigen Eigenschaften, die in der vorliegenden Dissertation betrachtet werden, bringen wesentliche Verbesserungen für den Einsatz von chiplosen RFID Systemen.

CONTENTS

LIST OF FIGURES

LIST OF ACRONYMS

ASIC Application Specific Integrated Circuit

EM Electro Magnetic

IoT Interner of Things

CST Computer Simulation Technology

FCC Federal Communications Commission

SDR Software Defined Radio

USRP Universal Software Defined Radio Peripheral

VNA Vector Network Analyzer

LPDA Log Periodic Array

RFID Radio Frequency Identification

RF Radio Frequency

RCS Radar Cross Section

TC Time Coded

FC Frequency Coded

UWB Ultra Wideband

PPM Pulse Position Modulation

ASK Amplitude Shift Keying

NPM Notch Position Modulation

NWM Notch Width Modulation

WB-SVD Window Based Singular Value Decomposition

OO-N/P On Off-Notch/Peak

N/P-P Notch/Peak-Position

N/P Notch/Peak

PPM Pulse Position Modulation

DGS Defected Ground Structure

CPW Coplanar Waveguide

FSS Frequency Selective Surfaces

HIS High Impedance Surface

DoF Degree of Freedom

DC Direct Current

CL Conversion Loss

HB Harmonic Balance

SNR Signal Noise Ratio

SIR Signal Interference Ratio

IC Integrated Circuit

LPF Low Pass Filter

HPF High Pass Filter

BPF Band Pass Filter

BSF Band Stop Filter

HPBW Half Power Beam Width

POC Proof-Of-Concept

RA Reflectarray

AC Anechoic Chamber

SLL Side Lobe Level

FBW Fractional Bandwidth

WG Wave Guide

FoM Figure of Merit

CFCB Center Feed Center Beam

OFCB Offset Feed Center Beam

CFOB Center Feed Offset Beam

F/D Focal/Diagonal

ISI Inter Symbol Interference

RLD Rotman Lens Designer

GO Geometrical Optics

TTD True Time Delay

RH Right Hand

LH Left Hand

IM Inter Modulation

1 INTRODUCTION

Right now, it is the era of Interner of Things (IoT) where all the objects are connected together through cloud data [2]. Hence, these objects are important to be identified. One identification methodology is to use the optical barcode. However, the barcode reading range is very limited, needs line-of-sight and requires a clean environment to operate reliably. In the meanwhile, RFID technology is favored for identifying a collection of objects reliably without line-of-sight restriction. The RFID technology uses RF signals to detect and identify information from tags attached to objects. The system comprises of two main components; a transponder/tag that contains a sequence of electronic codes used for the identification of an object and interrogator/reader that collects information from the tag. Although the RFID tags allow for automatic tracking outperforming the barcode, the technology could not be deployed in the market of item tagging due to the high tag cost resulted from the inescapable existence of the Application Specific Integrated Circuit (ASIC) chip. Moreover, the reading range is mainly limited by the chip turn on sensitivity rather than the reader sensitivity. Thus, the massive deployment can only be possible, if the tag relinquishes this ASIC chip and be similar to the barcode from cost and printing aspects.

Recently, the chipless RFID technology has tremendous potential in the market of item level labeling, tracking, and so on. The chipless tag consists of a specific metallic resonators which are placed over carrier substrate similar to the barcode. The unique EM signature of these metallic resonators is considered to be the tag-ID. Therefore, the chipped modulation principles could not be applied and thus the tag-ID is only modulated physically by the tag metallic strips. The RCS EM response of these strips which are impinged by an incident EM wave is static, repeatable and serves as the tag identifier. Consequently, the chipless tags outperform the other means of identification from the prospectives of cost, printing, security (hard coded), coping with ambient conditions and long lifetime.

The contributions of this thesis are to break through the bottlenecks that prevent the deploy-

ment of the chipless RFID systems from the aspects of tag and reader antenna limitations. Thus, novel chipless RFID tags are developed considering the tag compactness, coding capacity and reading robustness. Furthermore, novel reader antenna system is proposed for enhancing the reading coverage. Finally, the integrated testbeds are demonstrated.

1.1 Motivation and Scope

Chipless RFID systems are expected to revolutionize the predecessor's identification means. However, the system is still at the conceptual level and can not be exploited to its full potential in low-cost item tagging. Four major handicaps impede the chipless RFID system deployment. The first one is the limited reading range that resulted from the tag small RCS value. Moreover, the tag backscattered signal subjected to a fourth power reduction in magnitude. The second dilemma is that the clutter environmental reflections superimposed with the tag backscattered signal [3]. These multi-path reflections make the tag undetectable even if it is within the reader reading range. The third challenge is the tag coding capacity, which is required to be 96-bit similar to the chipped solution. Moreover, the tag size and the occupied bandwidth of the tag response should kept minimum. The last major problem is the multi-tag interference. The superposition of the tags responses within a specified interrogation zone can not be discriminated if the number of transponders exceeds a certain limit. These limitations are addressed in the literature from the signal processing point of view [4–6]. Moreover, the spatial division multiple access is proposed for theTime Coded (TC) chipless RFID tags [7].

On the contrary, those above FC chipless RFID handicaps are solved during the work of this dissertation from the following scopes:

1. **Novel Physically Modulated Tags:** To realize item-level tags, technical challenges, such as shrinking tag geometry, improving coding capacity and minimizing the tag operating bandwidth have been solved. Moreover, the introduced tags implement the collision avoidance MAC protocol introduced in [4]. This protocol mitigates the multi-tag interference by proposing a Notch Position Modulation (NPM) scheme for the tag code. Therefore, novel tag structures with novel physical modulation techniques are introduced. Moreover, the environmental clutter is minimized by exploiting the depolarized tag response.

2. **Reflectarray Readers:** RA are proposed for the improvement of the chipless RFID reader antenna system. This RA antenna system played a significant role in increasing the reading

range, enhancing the detection accuracy and localizing the tag. Furthermore, the problem of the tag response contamination with the multi-path components is dramatically reduced while utilizing the pencil beam provided by the RA antenna system.

3. **Novel Nonlinear Physically Modulated Tags:** In this regard, the chipless RFID tag exhibits a non-linear frequency response. Thus, the reader interrogation frequencies are different from that of the tag response. This nonlinearity is exploited to completely nullify the channel clutter response, increase the reading range and enhance the tag detection. Hence, novel physically modulated nonlinear tags are proposed considering the coding capacity, the tag size, and the reading coverage.

1.2 Dissertation Unique Findings and Organizations

This section briefly describes the unique findings introduced by this dissertation. These contributions are organized into chapters as following:

- **Chapter 2: Thesis Essentials**

  An introduction to the tagging means followed by a comparative study between these means is reported. This study reveals the unique promising features provided by the chipless RFID systems. Afterward, the principles of the chipless RFID systems are described. Then, a novel classification of the chipless RFID tags is presented. Finally, a comprehensive review of the FC tags and the reader antenna systems are introduced as the study focus.

- **Chapter 3: Novel Physically Modulated Chipless RFID Tags**

  In this chapter, the chipless RFID tag fundamental properties, the circuit model and the design guidelines are explained first. After that, the four novel physically modulated tags are presented. Moreover, the associated modulation schemes, components, simulations and measurements are deeply explained. Hence, the tagging effects are inspected considering the object conductive and dielectric material properties. Lastly, the frequency increasing possibilities and limitations are investigated.

- **Chapter 4: Reflectarray Readers**

  This chapter addresses the utilization of the RA antenna in the chipless RFID systems. The RA phasing element essentials and the detailed design steps are illustrated. Afterward,

novel fixed and steering beams RA antennas are introduced. Moreover, the RA bandwidth has been significantly improved to comply with the FC tags. Finally, the real-world physically modulated tags and RA antenna testbed is demonstrated.

- **Chapter 5: Novel Nonlinear Physically Modulated Chipless RFID Tags**

  In this chapter, the nonlinear tag essentials, diode selection, matching and conversion efficiency are investigated. The chapter composed of three different tag categories based on the exploited nonlinear generated term. For each type, the tag TX/RX antennas and the filtration requirements are considered. Moreover, the simulation and measurements of each category are verified.

- **Chapter 6: Conclusion and Future Work**

  This chapter concludes the introduced dissertation highlighting the unique findings. Moreover, a brief outlook in the research area is drawn.

2 THESIS ESSENTIALS

The purpose of this chapter is to present the essential background that is desired through the dissertation work. An overview of the labeling means and a comparative study between these means are introduced on top. Hence, the concept of the chipless RFID system as an emerging identification technology is declared. After that, a comprehensive coverage of the chipless tags illustrating the tag potential and handicaps is explained. Then, a survey on the RFID reader antennas is presented. Finally, the chipless RFID reader antenna requirements are listed and the proposed solutions are briefly described.

2.1 Identification Means

The foremost contactless identification technology is the barcode where the cheapness is the main advantage of the system. Although the barcode technology provides automatic identification, there are a lot of limitations that could not be improved further. These shortages are include the line-of-sight restriction, the individual detection with operator intervention, the need of clean environments, and the limited data capacity [8]. Moreover, the barcode is insecure (easily copied).

In contrast, the chipped RFID technology enables non-line-of-sight operation, automatic tracking, group detection, high data capacity, and outperforming the barcode technology. The RFID tags are classified based on how the tag silicon chip is energized in two categories. The first one is active tags where the tag contains a battery that makes the tag always active. The second category is the passive tags where the tag is energized from the reader. For both categories, a communication protocol is established between the reader and tags. This is time and power consuming. Also, using the same carrier frequency in transmit/receive paths increases the mutual coupling problem at the receiver end, contaminate the tag response due to cluttering signals and thus reduce the Signal Noise Ratio (SNR). Lastly, for the chipped RFID systems, the coverage

is limited by the minimum wake up power for the chip which is about $-20\,\text{dBm}$. Therefore, it is deduced from the above discussion that the electronic circuit of the chipped RFID tag is a primary hindrance.

Presently, the chipless RFID tags exclude this electronic circuit to minimize the cost and overcome the limitations mentioned above. Due to the exclusion of the Integrated Circuit (IC), there is no threshold power level limitation as for the former chipped tags. Thus, the reading range is theoretically higher and is only limited by the reader sensitivity. Moreover, the chipless tag response is not time varying (static) and the unique EM fingerprint of the tag inscribed metallic shape is considered to be the tag-ID, like radar target. Consequently, the chipless RFID systems are expected to overtake the optical barcode and the chipped RFID counterpart as well. Hence, the technology affords a massive business potential in the market of item level labeling and tracking applications. However, there are a lot of challenges that hinder the technology, such as inserting appropriate data bits in a compact tag size, increasing the reading range, etc. These limitations are described in this chapter from the physical aspects of the tag and the reader antenna systems.

2.1.1 Chipless RFID System Description

A typical chipless RFID system comprises of three main parts as explained in Fig. 2.1. A reader which is responsible for the interrogation, the detection (frequency or time domain) and the code identification of the tag Radio Frequency (RF) signature. Secondly, an antenna system which illuminates the tag metallic scatterer's and determines the reader interrogation zone. Thirdly, the chipless RFID tag which is the encoder that realizes the physical modulation process or the identification code. Therefore, the tag receives the reader interrogation signal and re-radiate it's ID back after modulating it by the tag structure (identifier).

2.2 Chipless RFID Tags

The chipless RFID tag consists of a metallic pattern over a grounded or ungrounded dielectric substrate. These tags can be in general classified based on the coding domain into, time, frequency and hybrid coding domains as described in Fig. 2.2. Moreover, each category can also be classified based on the tag structure, size, coding capacity, scalability, the format of encoded data, linear and nonlinear etc.-.

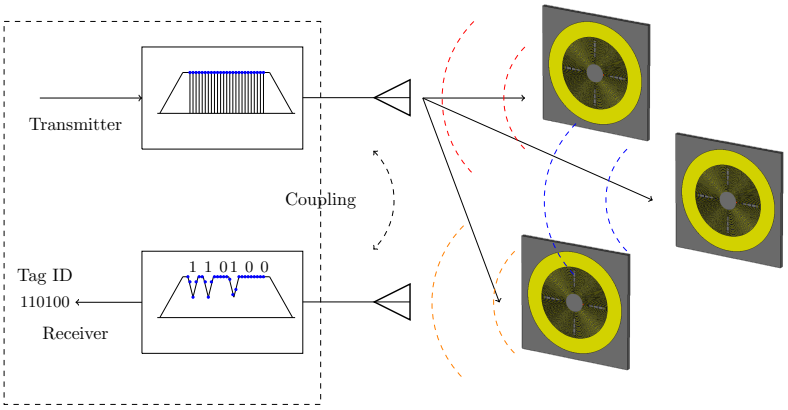

Figure 2.1: Generic chipless RFID system reader interrogates multiple tags at the same time.

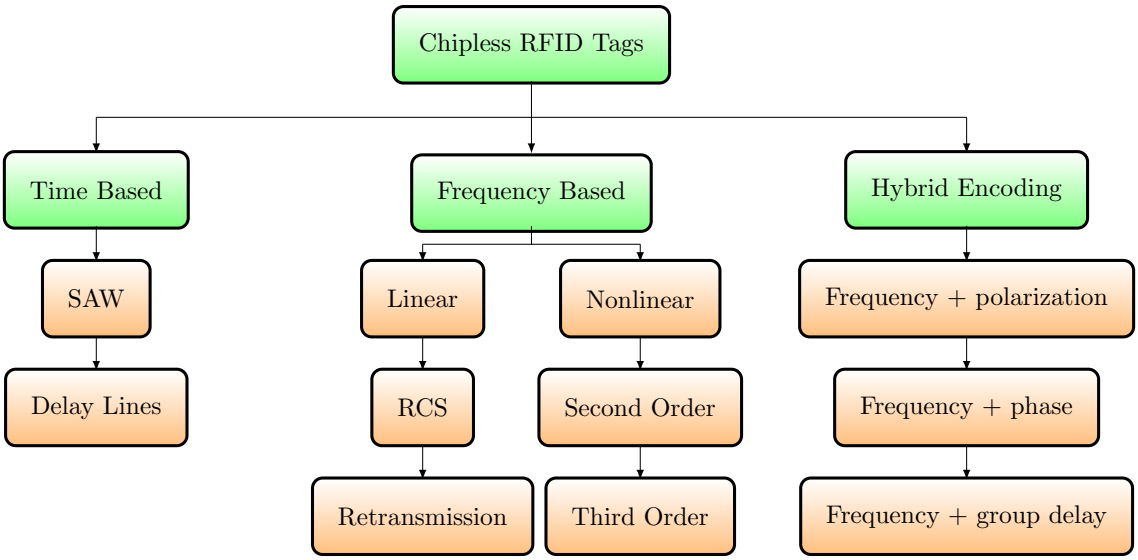

Figure 2.2: Chipless RFID tag coordinations.

The spectral based chipless RFID system is the main concern of this dissertation since it is more efficient in terms of tag size, reader complexity and coding capacity. Mostly, the FC tag consists of several closely placed resonators (e.g., dipoles or patches) which are resonating at different frequency points to execute a distinct physical modulation scheme. Thus, the tag-ID is incorporated in the tag re-radiated frequency response in the form of physically modulated notches and/or peaks. Hence, the operating frequency range is divided into N sections based on the quality factor of the tag resonators and the employed physical modulation scheme.

The spectral based chipless RFID tags are classified from the structural point of view into RCS based and re-transmission based tags. The retransmission tag consists of two UWB receiving and transmitting antennas that are connected to a multi-stop band filter in between

for realizing the coding notches. On the other hand are the RCS based tags, where the tag is considered to be a radar target which has a particular RF signature. Thus, the RCS signature which has a resonance and non-resonant frequency points serves as the tag identifier.

In principle, the RCS value is defined by (2.1):

$$RCS : \sigma(f) = \lim_{r \to \infty} 4\pi r^2 \frac{P_s(f)}{P_i(f)} \tag{2.1}$$

where, r is the reading range, $P_s(f)$ is the total backscattered power (W) and $P_i(f)/4\pi r^2$ is the incident power density (W/m^2). Thus, the RCS is a measure of the tag backscattering effective area, where the reading distance and transmitted power are not factors that influence the RCS estimations. Hence, the RCS is a property of the tag reflectivity that depends on the geometrical shape, material, frequency, the relative tag size with respect to the wavelength of the illuminating reader and the wave incident and backscattered angle. Moreover, the RCS value also depends on the angular orientation of the target relative to the reader transmitting and receiving antennas.

Considering the case of the mono-static reader where one antenna is used for both transmission and reception. The reader range can be theoretically estimated as following:

$$\frac{P_R}{P_T} = \frac{G^2(f)\lambda^2}{(4\pi)^3 r^4} \sigma(f) \tag{2.2}$$

where, P_R is the received power (W), P_T is the transmitted power (W), G is the reader antenna gain, r is the distance between the reader and the tag (m) and $\sigma(f)$ is the tag RCS (m). It is clearly noticed from eq. 2.2 that the larger is the tag projected effective area (RCS value), the higher is the coverage. In principle, the RCS frequency response of a radar target has three different regions of operation. The first one is the Rayleigh region where the target area is less than the reader signal wavelength. In this region the target which is the tag in our case is invisible to the reader signal and thus the RCS value is minimum. The second zone is the resonance region where the tag size is comparable to the wavelength. In this region, the RCS value can attain a maximum or a minimum value based on the engineered tag structure. Finally, the optical region where the tag dimension is approximately larger than 10λ. In this region, the RCS reaches a maximum steady state value and hence can be easily detected.

Consider a half wavelength dipole is placed over a grounded dielectric substrate as illustrated

in Fig. 2.3. The theoretical RCS value for the rectangular plate can be calculated by (2.3).

$$\sigma(f) = 4\pi {A_e}^2/\lambda^2 \tag{2.3}$$

where A_e is the effective area of the plate, which is equal to the physical area multiplied by the aperture efficiency. Therefore, the maximum RCS value can be estimated utilizing (2.4).

$$\sigma_{max} = 4\pi L^2 W^2/\lambda^2 \tag{2.4}$$

where L is the flat plate length and W is the width. It is noticed from (2.4) that the reading range is increased by increasing the tag RCS value, which increases with frequency for a given physical area. The theoretical RCS calculations at 2 GHz and 6 GHz verifies well with the full wave simulation shown in Fig. 2.3. Thus, the Raleigh zone of the given tag size is the region of frequencies below 2 GHz as illustrated in the RCS frequency response shown in Fig. 2.3. For the frequency region beyond 2 GHz, the tag has two modes of reflections which are the structural and dipole reflection modes. The structural mode is due to the structure itself and doesn't have any amplitude or phase information. However, the antenna mode results from the inscribed dipole itself. Both modes are destructively interfered at the dipole resonant frequency and introduce a notch as shown in Fig. 2.3. Therefore, the notch pattern and position are considered to be the unique tag-ID.

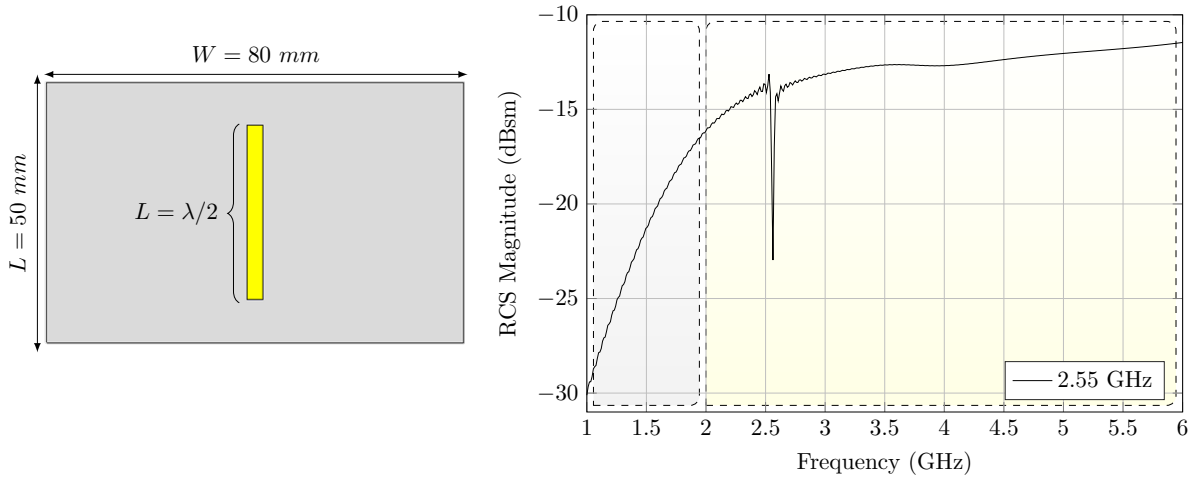

Figure 2.3: Half wave length dipole placed over grounded dielectric substrate and the corresponding RCS frequency response.

2.2.1 Chipless RFID Tag Challenges

Many challenges impede the chipless tag deployment. These handicaps are discussed in this section and addressed in the following chapters in more details.

1. **Tag Size:** The first challenge arose how to insert an appropriate number of coding bits in this dummy tag structure while preserving its size. The tag size is increased with increasing the number of the inscribed resonators. Therefore, novel tag structures with high coding capacity are proposed.

2. **Occupied Bandwidth:** Another limitation is the occupied bandwidth of the tag response which in general increases with coding bits increase. Therefore, this linear relation is broken by employing novel coding techniques. Moreover, the tag resonators are optimized for minimum notch and peak widths.

3. **Mutual Coupling:** One of the handicaps is the coupling variation between the tag resonators while coding by removing or inserting an encoding resonator. This variation lead to false code identification since the link between the code and tag geometry is no longer related. Thus, a novel encoding mechanisms are proposed to preserve the tag-induced current distribution and so the resonance frequency position and bandwidth.

4. **Clutter Reflections:** The environmental clutter reflections are usually stronger than the tag reflections and thus conceal the tag response. This results in error detection for the tag resonant frequencies. Moreover, the tag resonant frequencies are diminished by the spatial variations of the fields [9]. Therefore, approaches from the physical tag structure point of view that can reduce this cluttering are significantly important. Furthermore, the non-linear tag response is exploited to completely isolate these environmental reflections.

5. **Reading Range:** Dissimilar to the chipped tags the chipless counterpart is limited only by the reader sensitivity. Thus, it is a trade-off between the tag size and the required minimum value of the re-radiating RCS. Hence, the reading range is determined from the least possible received power at the reader which is considered to be in its sensitivity range.

6. **Tagging Effects:** Basically, the RFID technology, even the conventional one does not work for specific materials like metals and food items. Thus, the proximity of tags to these conductive and dielectric objects is another important challenge. Thus, the tag response should cope with the detuning effects caused by these materials.

7. **Multiple reading:** Reading multiple tags simultaneously is another handicap that impedes the chipless RFID system deployment. Therefore, the tag-ID is somehow implementing a collision avoidance protocol that enables multi-tag identification.

8. **Printing Capability:** Another handicap, is the tag printing capability which is closely linked to the tag cost. Therefore, a novel printable tag structures are introduced.

Attaining these properties all together is a big challenge. However, it has to be observed that the chipless RFID system is application specific. For example, for some applications, the large number of coding capacity is not required. However, printing the tag structure is an ultimate objective. So, only a small reliable ID string that can codify hundred of different products is sufficient. On the contrary, for applications such as supermarket scenario, the coding capacity and the tag size are the main concern.

2.3 RFID Reader Antennas

RFID readers can be classified into three groups which are hand-held, mobile or stationary readers. Any of those RFID readers consists of two main components which are the interrogation circuitry and the antenna system that determines the interrogation zone. The chipless RFID tag is dumb. Thus, to mitigate the challenges of reading such stupid tag, all the intelligence are carried to the reader side. Hence, the antenna system plays a significant role in capturing the optimum RCS that is backscattered from such tag. This antenna system can be a single element or array type which is classified based on configuration into 3-D and planar arrays. The antennas that are utilized in the RFID systems are planar microstrip patches. However, based on the purposes and application, it can be a horn, helical or any.

In general, the antenna system is accommodated to the reader type. The first reader type is the hand-held and thus the antenna size is desired to be the smallest. Hence, in this case, one antenna is connected to a circulator and utilized for both transmission and reception. Regarding the second category where the reader is fixed to a mobile vehicle, the antenna can be small or large based on the vehicle. The last reader category is the fixed readers, which are the core of the study. For these fixed interrogators the antennas are kept at different locations and angles. However, the antenna radiation pattern can be fixed or steered. The fixed beam antenna system provides a single and fixed radiation pattern. Although it is easy to install, it picks up the environmental reflections along with the tag response. Moreover, all the tags covered by the

antenna beam respond to the reader interrogation signals simultaneously, which also may result in reading errors. The second type is the beam scanning antenna array, which can provide spatial filtering between tags and thus reduces the collisions among tags, mitigates the multi-path interference and enables tag localization. In the following section, a literature review for these two types is introduced from the scope of the chipless RFID systems.

2.3.1 Chipless RFID Reader Antennas

The chipless RFID system is a new technology and hence there is no commercial tags, reader antennas or even regulations up to date. However, the aforementioned basic antenna types are briefly reviewed in this section.

The first category is the fixed beam antenna array. Thus, the LPDA is an example of a fixed beam linear polarized antenna array. It consists of multiple dipoles in parallel with slight overlapping resonances to cover continuous UWB frequency range. Thus, the LPDA can be utilized for the chipless RFID readers since it can provide a high gain about 7 dBi and the tag orientation and place are almost fixed. However the LPDA radiation pattern is asymmetry and hemispherical, so reading tags from half of the space. Thus, the possibility of multi-tag interference is high. Another example is the parabolic reflector which is a directional high gain antenna. Moreover, it operates over the feeder frequency independent on the polarization or the angle of the incident wave. However, the parabolic reflectors are bulky and incompetent for beam steering.

On the other hand, the beam steering antenna array generates a single beam which is steered over the entire space searching for the tag or a specified condition. Therefore, this antenna array can mitigate the tag reading problems by offering a directional high gain beam towards the desired tag location and nulls towards the interference. The most popular beam steering antenna arrays are the switched beam antennas and the phased array antenna or a combination of both types. The switched beam antenna array consists of multiple fixed antennas that are spatially separated and connected to power divider/combiner circuits via a matrix of switches. These switches are controlled using a specific control algorithm to activate a particular antenna element or group of elements at the same time. The advantage of such antenna array is the low cost and processing time compared to the phased array antenna. On the other hand, the phased array antennas where each element fed with a pre-calculated amplitude and phase values. Therefore, this antenna is capable of steering the beam towards the desired direction and the

nulls can be steered towards the interfering direction. However, the phased array antennas have little acceptance in the chipless RFID systems due to the following reasons. The first one is that the main advantage of the chipless RFID system is the low cost. However, the phased array antenna requires expensive, complex feeding networks that consist of RF power distribution network, phase shifters, biasing networks, electronic switches and a processor that programmed with the control algorithm. Furthermore, the chipless RFID system operates over UWB range of frequencies which can not be attained with such complex feeding network antennas. Therefore, the only methodology to accomplish an appropriate UWB antenna array with stable performance is to exclude such complex feeding network. One possible solution is to utilize the optical beam-forming networks where an optical signal is modulating the RF signal. After that, specific delays are introduced to that modulated signal using dispersive (changing the optical signal wavelength) or non-dispersive (variable lengths) optical fiber lines. Thus, the system losses and complexity are high [10].

From the above discussion, it is concluded that the utilized chipless RFID reader antenna should attain the following characteristics. It should operate over UWB range of frequencies, be directive, high gain with beam-steering capability and low cost. During the work of this thesis the spatial feeding antenna arrays specifically, the Reflect-arrays are proposed to be utilized in the reader side to achieve the former objectives. Since spatial feeding, the antenna performance degradation due to the loss in the feeding network has been excluded. Furthermore, the flat reflectarray surface is portable, deployable, printable and thus suitable for the mass volume production requirements.

The next chapters, address the solutions that have been applied for the chipless RFID limitations from the physical perspective of the reader antenna system and tag design.

3 Novel Physically Modulated Frequency Coded Chipless RFID Tags

This chapter presents four innovative physically modulated FC chipless RFID tags aiming at maximizing the coding capacity, conserving the operating frequency range, and preserving the tag size. First, the NPM tags are presented where the tag-ID is based on the notch existence or nonexistence at certain frequency positions. Hence, the position of the notches are determined by the tag-ID and realized physically by engineering the tag structure. In this category, two novel tag structures fulfilling the NPM scheme are introduced. The first one is RCS based with novel encoding methodology. The second NPM tag is retransmission based where the reader interrogation signal and the tag response are separated in two orthogonal polarization planes. Therefore, the polarization diversity is used to minimize the environmental reflections and enhance the tag detection. Second, the NWM tag is presented where the tag-ID is not only based on the notch position but also on the notch width. Hence, the tag resonators are physically modulating the notch width and position simultaneously aiming at enhancing the coding capacity. Eventually, the novel OO-N/P and N/P-P modulation tag is demonstrated. The operation principle relies on exploiting the backscattered co-polarized and cross-polarized responses from a tag illuminated with a linear polarized wave. Consequently, the tag-ID is configured in two orthogonal planes. The frequency notches are encoded in the co-polarization plane and the re-radiation peaks are encoded in the cross-polarization plane. Therefore, the Co/Cross-polarizing Notch/Peak modulation scheme presents a novel criterion for maximizing the coding capacity of the chipless RFID systems. Moreover, the cross-polarized response enhances the tag detection in a real environment. The proposed tags and their associated physical modulation schemes are validated using EM simulations and measurements. The carried out work introduced in this chapter is published in [11–14].

3.1 Introduction

Since the chipless RFID tags are without chip, dummy and memoryless, the conventional modulation and encoding principles can not be applied. Consequently, the tag-ID is incorporated in the physical EM signature which is modulated and realized by the tag structure. Therefore, the tag inscribed metallic resonators are physically modulating the reader interrogation signal either in the time or in the frequency domain [4]. For the time modulated tags, a pulse signal is transmitted from the reader to interrogate the tags and then each tag implements a specific Pulse Position Modulation (PPM) scheme [15] to configure the inherent code. Afterwards, these modulated pulses are retransmitted towards the reader to figure out the tag's ID. Although the time modulated tags enable higher reading range, simple calibration procedures, and immunity against environmental reflections [16], only few bits can be encoded with large tag size even when employing meta-material cells [17]. Furthermore, the reader requires high processing power with nanoseconds [15] resolution to correctly detect the backscattered signal.

On the other hand, the FC tags physically modulate the reader's interrogation signal which can be transmitted in a pulse or in a frequency sweeping waveforms. Mostly, the tag's resonators absorb certain frequencies from the interrogation signal [4] where each resonator codifies a tag coding bit. Therefore, the frequency modulated tags undergo a linear relation between the number of coding bits and the number of encoding resonators, which limits the coding capacity and tag size [18]. Furthermore, the tag response occupies extremely wide bandwidth that requires complicated and expensive spectrum analysis devices [19].

Recently, several approaches have been proposed to increase the coding capacity, conserve the occupied bandwidth and miniaturize the tag size. Some approaches employ hybrid coding techniques [20, 21] which utilize the phase state as a coding dimension. However, encoding data in phase without equalizing the multi-path results in bit-decoding errors [12]. Other approaches use different modulation parameters such as Amplitude Shift Keying (ASK) [22], [23] which encodes data in the amplitude level of the backscattered signal. However, the backscattered co-polarized tag response is angularly dependent and varies with the relative distance between the reader and tag. Additionally, it is sensitive to structural mode and environmental reflections. Therefore, distinguishing between the different amplitude levels is quite challenging, unless there is some reference levels. The state of the art researches for the FC tags are summarized in table 3.1, where the tags are compared in terms of encoding technique, size, occupied frequency range, and coding density.

Table 3.1: Recently published FC chipless RFID tags

Resonator Type	Encoding Technique	No. Bits per Single Element	Tag Size (cm^2)	Frequency Range (GHz)	Coding Density ($bits/cm^2$)
Spiral [18]	N	1	6.5×8.5	3-7	0.63
Rhombic Loop [22]	Y	2	4×7	3-6	0.25
Stepped Impedance [24]	Y	2	2×3	3-9	7
U-Shape [25]	N	1	25×70	2-4	1.14
Rectangle Loop [1]	Y	2	2×4	3-10	3.56
C-Ring [26]	N	1	D2.5	2-4	6.11
C-Shape [23]	Y	3	3×5	2-5	1.25

To dethrone the barcode from item level labeling, the research orientation in the field should be devoted to increasing the coding capacity, preserving the tag size, conserving the operating frequency range, minimizing the environmental reflections, and ensuring accurate detection. However, to attain these properties all together is a big challenge. Therefore, this chapter introduces novel tag approaches which assist in deploying the chipless RFID system in the full potential. The FC tag design principles and the corresponding circuit model are illustrated in Section 3.2. Section 3.3 exhibits the NPM RCS based tags while the retransmission tag is demonstrated in Section 3.4. Section 3.5 interprets the core functionality of the introduced NWM principles. Moreover, the corresponding tags are illustrated. In Section 3.6, the proposed OO-N/P and N/P-P modulation tags are presented. The simulation and measurement results for each tag are presented to prove the validity of the introduced physical modulation schemes. Finally, the chapter conclusive discussion is drawn in Section 3.7.

3.2 FC Tag Design Principle

FC tags consist of FSS which are placed over grounded or ungrounded dielectric substrates. These surfaces are utilized as spatial filters for the FC tags. Therefore, the tag is illuminated by incident plane wave and the tag's RCS frequency response as expressed in (3.1) serves as the tag

identifier.

$$\sigma(f) = \lim_{r\to\infty} 4\pi r^2 \frac{P_{\mathrm{s}}(f)}{P_{\mathrm{i}}(f)} \tag{3.1}$$

where $\sigma(f)$ is the RCS frequency response, r is the reading range, $P_{\mathrm{s}}(f)$ is the total backscattered power in (Watt) and $P_{\mathrm{i}}(f)/4\pi r^2$ is the incident power density (Watt/m^2). Thus, the RCS is a measure of the tag backscattering effective area, where the reading distance and transmitted power do not influence the RCS estimations. Hence, the RCS is a property of the tag reflectivity that depends on the geometrical shape, material, frequency, aspect angle and the relative tag size with respect to the wavelength of the illuminating reader. Therefore, the RCS frequency signature can have a minimum and maximum values with resonant and non-resonant frequency positions based on the engineered FSS. Hence, the design principles of the tag resonators, the circuit model and the mathematical representation are derived.

The FSS is placed over a grounded dielectric substrate to realize the High Impedance Surface (HIS), which exhibits impedance larger than the free space impedance all over the resonance frequency band. Therefore, this surface absorbs the incident plane wave and the resonance bandwidth is the range of frequencies where the absolute value of the tag impedance is greater than the free space impedance [27]. Consequently, the equivalent circuit model shown in Fig. 3.1 consists of RLC series branches representing the resonators impedances and short circuit stub representing the grounded dielectric substrate impedance. Thus, the FSS equivalent impedance is given by (3.2).

$$Z_{\mathrm{FSS}} = Z_1//Z_2.....//Z_N = R_s \pm \mathrm{j}X_s \tag{3.2}$$

where Z_{FSS} is the total surface impedance, $Z_i, i = 1, 2, ...N$, is the RLC impedance of each resonance branch, R_s, and X_s are the equivalent resistance and reactance respectively. The short circuit dielectric substrate impedance is calculated using (3.3) [28].

$$Z_{\mathrm{d}} = \mathrm{j}\frac{Z_0}{\sqrt{\varepsilon_{\mathrm{r}} + \mathrm{j}\grave{\varepsilon}_{\mathrm{r}}}} \tan\left(k_0 h \sqrt{\varepsilon_{\mathrm{r}} + \mathrm{j}\grave{\varepsilon}_{\mathrm{r}}}\right) = R_d + \mathrm{j}X_d \tag{3.3}$$

where Z_{d} is the inductive impedance of the grounded dielectric substrate, Z_0 is the free space impedance ($\approx 377\,\Omega$), $(\varepsilon_{\mathrm{r}} + \mathrm{j}\grave{\varepsilon}_{\mathrm{r}})$ is the effective permittivity of the substrate, k_0 is the free space wavenumber and h is the substrate thickness. This grounded substrate behaves like an inductor unless the thickness is less than the quarter guided wavelength. Finally, the FSS and the thin grounded dielectric substrate are stacked together to compose the HIS, where the input impedance

as illustrated in Fig. 3.1 is calculated as following:

$$Z_{\text{inp}} = Z_{\text{FSS}} // Z_{\text{d}} \tag{3.4}$$

$$Z_{\text{inp}} = -\frac{Z_0^2(1+\Gamma)}{2Z_0\Gamma} \tag{3.5}$$

$$Z_{FSS} = -\frac{Z_d Z_0(1+\Gamma)}{Z_d - Z_0 - \Gamma(Z_d + Z_0)} \tag{3.6}$$

where Γ represents the reflection coefficient of the HIS that is calculated with the aid of a full wave simulation program. The values of the inductances and capacitances can be iteratively obtained once the value of the FSS impedance is calculated by (3.7)

$$Z_{FSS} = -\frac{Z_d Z_0(1+\Gamma)}{Z_d - Z_0 - \Gamma(Z_d + Z_0)} \tag{3.7}$$

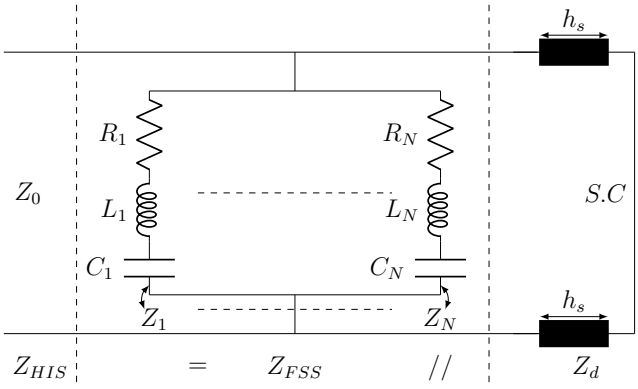

Figure 3.1: Equivalent circuit model for the grounded FSS with multiple resonators.

Various basic elements with the same substrate parameters are simulated to investigate the backscattered signals from a tag excited with a linear polarized plane wave. The backscattered co-polarized response is presented in Fig. 3.2a and the cross-polarized backscattered response is illustrated in Fig. 3.2b. This simulation study together with the examination of the electric and magnetic fields distribution on the element surface reveals three facts. The first one is that the fields are destructively interfering in the co-polarized plane that generates a notch response as shown in Fig. 3.2a. Moreover, the fields in the cross-polarized direction have the same polarity and hence produce a peak radiation in that direction as shown in Fig. 3.2b. The second is that the crossed dipole has the narrowest resonance bandwidth and the patch has the widest. The last one is that the cross-polarized peak can be exploited to increase the coding capacity and ensure

accurate detection.

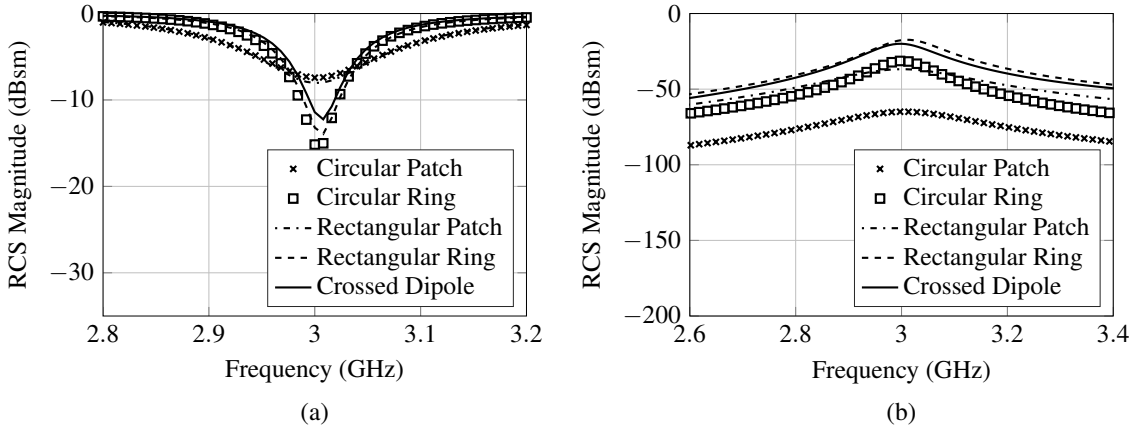

Figure 3.2: Co/Cross-polarized response for different FSS cell shapes, while assuming infinite cell periodicity and linear polarized wave illumination: (a) Co-polarized notches response. (b) Cross-polarized peaks response.

3.3 Notch Position Modulation Tags

In the NPM scheme, each notch position resembles a tag coding bit, where the presence of a notch resembles the logic-1 and the absence mimics the logic-0. Hence, this is the basic modulation scheme where the operating spectrum is divided based on the minimum achieved resonator bandwidth. Therefore, the notch width fluctuations should be kept minimum. In this category, two different scalable and printable tags are introduced. The first one is RCS based and consists of coplanar ring resonators without the ground plane and thus printable as depicted in Fig. 3.3. Each ring resonator symbolizes a tag coding bit where the ring radius is determined by (3.8):

$$R = \frac{c}{2\pi f_0}\sqrt{\frac{2}{\varepsilon_{reff}+1}} \tag{3.8}$$

where f_0 is the resonance frequency, c is the light speed, ε_{reff} is the substrate permittivity and R is the ring radius. The advantage of the circular ring is that the spurious modes are not generated because of the structure symmetry [29]. Furthermore, the coding bits can be increased to a certain limit without increasing the tag size by adding extra rings within the same confined area.

Three key features are introduced to the new enhanced tag design. The first feature is adding redundant deactivated rings in between the coding ones to minimize the notch width, increase the number of coding bits and thus conserve the spectrum. Therefore, 14-bit coding capacity

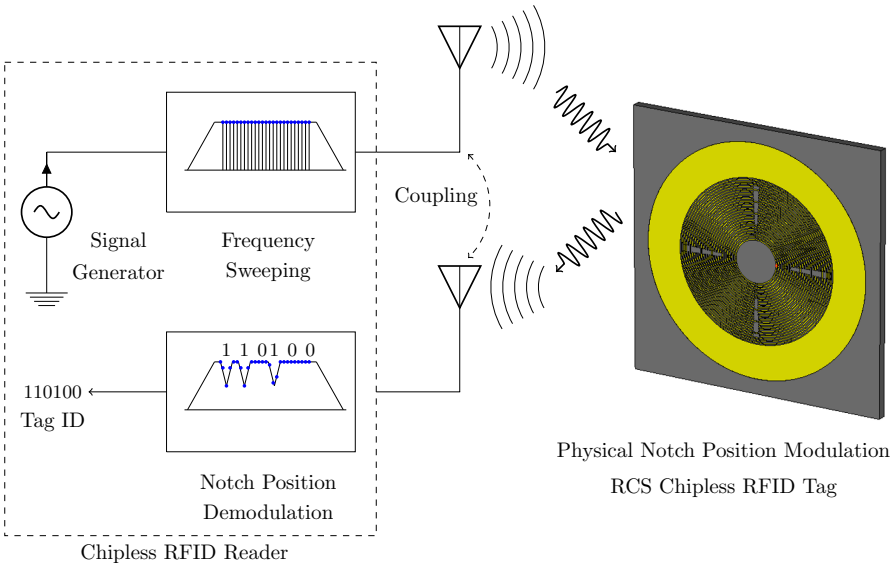

Figure 3.3: NPM RCS tags system description.

is achieved in 3 GHz bandwidth from (2 GHz to 5 GHz) compared to 8-bit coding capacity in 8 GHz bandwidth introduced in [29]. The encoding methodology followed in [29] to switch off a notch is to remove the corresponding ring. However, the RCS resonance bandwidth is highly affected by the presence or absence of the adjacent resonators. This resonance bandwidth gets wider if the nearby notch is removed. Therefore, a novel encoding methodology is introduced to preserve the current distribution and so the position and bandwidth. This methodology is based on adding a cut in the ring current path in the two orthogonal planes to remove the corresponding notch from the coding spectrum without removing the associated ring as followed in [29]. The last feature is to boost the level of the backscattered power by designing (2×2) tag array. This array increases the value of RCS by 6 dBsm at the expense of increasing the tag size.

The manufactured tag as shown in Fig. 3.4 illustrates the novel encoding methodology and the inserted supplementary resonators. Four different coded single and array tags with 14-bit coding capacity are designed, simulated and implemented as shown in Fig. 3.5a, b. The substrate used in the design is RO4003C with a permittivity of 3.38, loss tangent of 0.0027 and a thickness of 1.52 mm. It is revealed from both responses that the notches of the different coded tags are uniform and the RCS level of the array tag is higher than single tags by 6 dBsm. Furthermore, the novel encoding methodology and the switched off or redundancy resonators inserted in between the coding rings provide immunity against variation of the notch width and position.

The realistic response of these tags is verified outside the anechoic chamber. The measurement setup as described in Fig.3.6 exploits the Software Defined Radio (SDR) which is

Figure 3.4: NPM manufactured single and array RCS based tags.

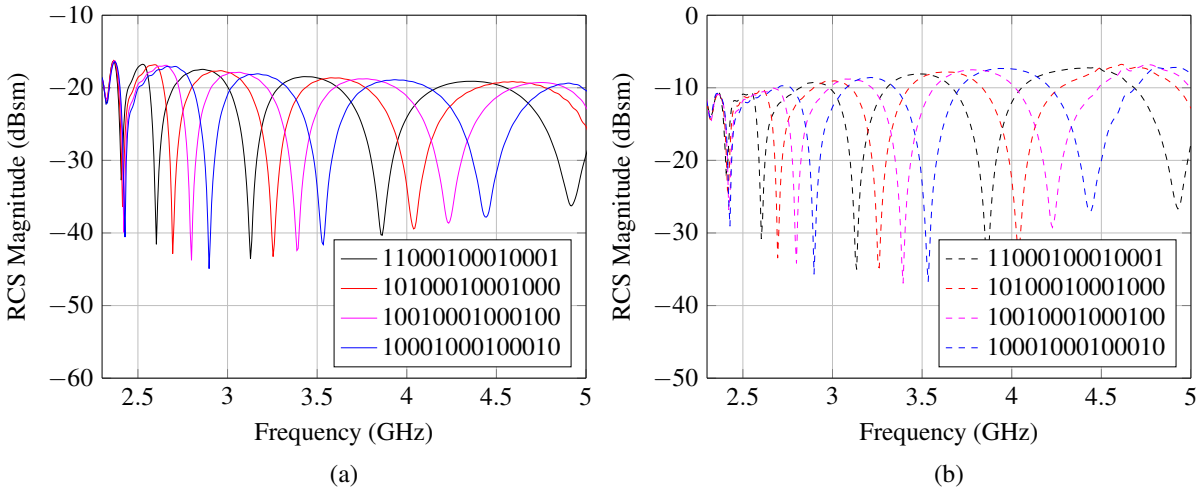

Figure 3.5: RCS frequency response for different NPM single and array tags illustrating 14-bit coding capacity in 2.7 GHz spectrum BW: (a) Single tags (b) Array tags.

connected to two LPDA antennas for interrogation and detection. Hence, the tag is mounted at a distance of 20 cm in the broadside direction of the LPDA antennas. The simulation and measurement results for two different coded tags are illustrated in Fig. 3.7, where the simulated and measured notches are in a good match.

Despite the RCS based tags are small size and the channel cluttering signals are dramatically superimposed with the tag backscattered response [12], they are successfully detected in a real environment. The low RCS value of the small tag structure can be enhanced as explained by forming a tag array. Moreover, the undesired clutter reflections and the mutual coupling between the reader antennas can be minimized by exploiting a depolarizing response. Therefore, dissimilar to the previous tag, a depolarizing retransmission tag is introduced in the following

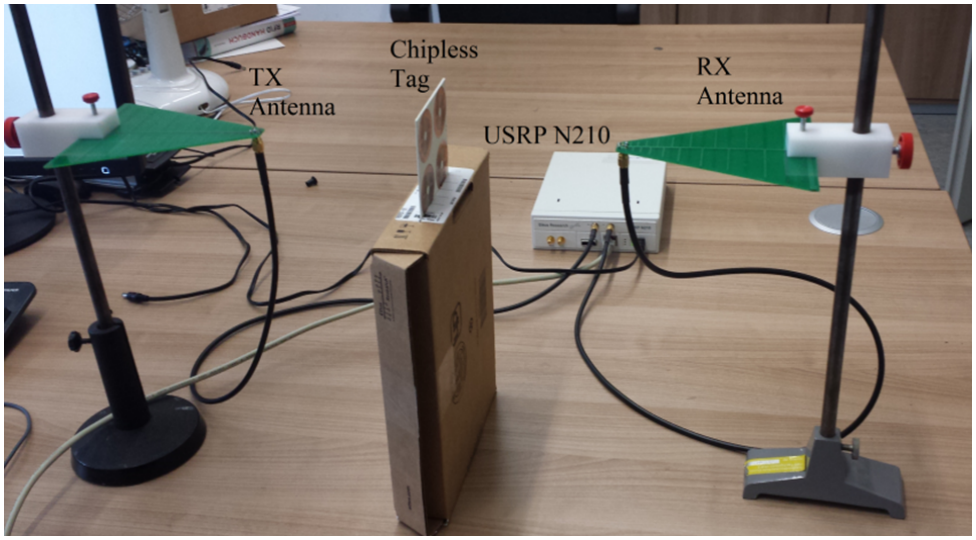

Figure 3.6: NPM RCS tags indoor measurement setup.

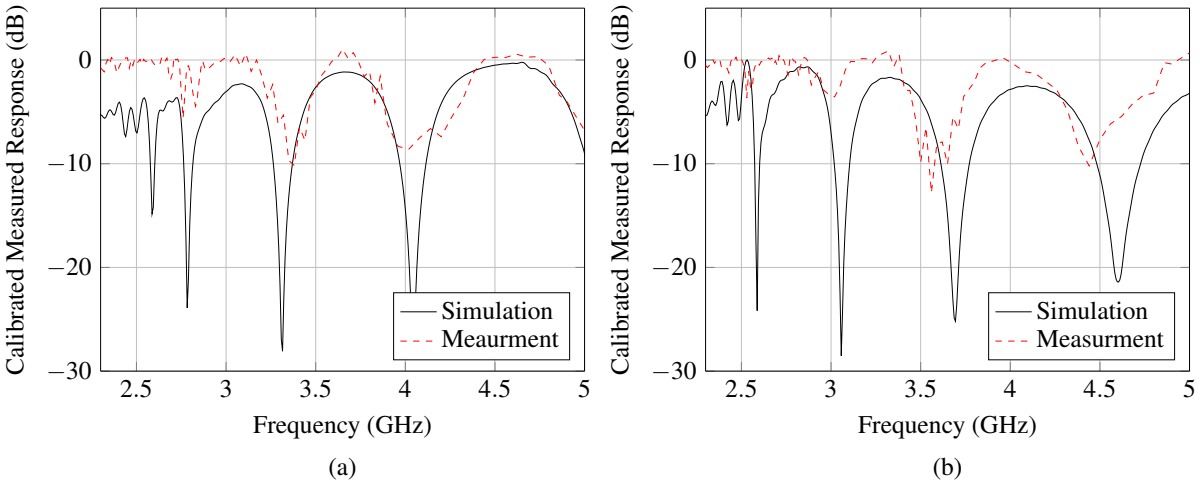

Figure 3.7: NPM RCS tags indoor measurement results: (a) Tag 1 (11000100010001). (b) Tag 2 (10001000100010).

section.

The deficiencies of the retransmission tags presented in the literature are the unprintable tag structure and the incapability to increase the number of resonators within the same size. In state of the art, the followed methodology to increase the number of notches for the retransmission tag is to add extra resonators in series and thus enlarging the tag size [30–32]. Also, the nonuniform radiation characteristics of the tag UWB antennas can tilt the maximum radiation direction. These limitations are solved in the proposed tag which is presented in the following section.

3.4 Printable Depolarizing Chipless RFID Tag Based on DGS Resonators for Suppressing the Clutter Effects

In this section, a novel single layer FC depolarizing tag is introduced. The tag consists of L-shape Defected Ground Structure (DGS) resonators defining the tag signature and two orthogonally polarized UWB monopole antennas for realizing the cross-polarization retransmission process as shown in Fig. 3.8. Consequently, the polarization diversity between the reader interrogation signal and the tag retransmitted response is utilized to reduce the mutual coupling and minimize the channel clutter effects. The number of coding resonators in the proposed tag structure can be easily inserted in parallel as illustrated in Fig. 3.8. This significantly enables increasing the coding capacity while preserving the same tag size. Moreover, a novel encoding methodology is proposed to preserve the resonator current distribution while encoding. Hence, an 8-bit prototype from (3.1 GHz to 6.1 GHz) is presented and the maximum achievable number of notches is investigated. The UWB monopole antenna and the DGS resonators simulation, implementation and measurements are separately verified and demonstrated. Furthermore, two tags with different codes are designed, simulated and implemented. After that, a reference tag without resonators is exploited for calibration purposes. Hence, the manufactured tag operation is conclusively verified in an indoor real-world environment.

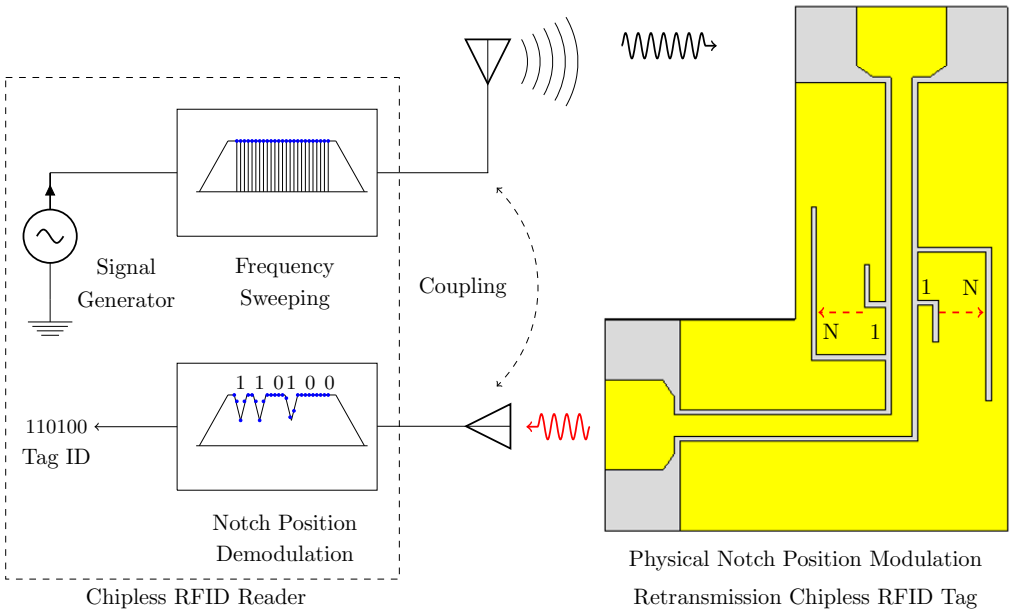

Figure 3.8: NPM retransmission tag system description.

3.4.1 CPW UWB Monopole Antenna

The CPW UWB monopole antenna comprises of radiating patch and ground plane on the same surface which are placed over a dielectric substrate. The radiating patch can be assumed to be any shape. However, regular shapes such as elliptical, circular, square and rectangle are typically used to simplify the analysis and performance prediction. Although, the circular and elliptical monopoles exhibit much wider bandwidth than the other shapes, but, the rectangular patch is simple in geometry and featured with the more uniform radiation pattern over the impedance bandwidth [33]. So, the designed CPW UWB monopole consists of a rectangular radiating patch where the lower band edge frequency is given by (3.9) [34]:

$$f_L = \frac{7.2}{\{L + r + p\} \times k} \tag{3.9}$$

where f_L is the lower band edge frequency in GHz, L is the length of the monopole patch, r is the effective radius of the equivalent cylindrical monopole antenna, p is the feeding gap, all in cm.

$$k = \sqrt{\varepsilon_{eff}} \tag{3.10}$$

where k is a correction factor due to the presence of the dielectric substrate. The value of r in the case of the printed rectangular monopole is given by (3.11) [34].

$$r = \frac{W}{2 \times \pi} \tag{3.11}$$

where W is the width of the rectangular patch. Accordingly, a rectangular radiating patch is designed first. Afterward, the feed region and the radiating patch are optimized to smooth the current distribution and increase the impedance bandwidth. Therefore, 17 GHz impedance bandwidth has been achieved as illustrated in Fig. 3.10. Moreover, the simulated realized gain varies from $(2-5)$ dBi and the radiation pattern over the frequency band of interest is uniform as described in Fig. 3.10. The designed monopole evolutions illustrating the final manufactured dimensions are described in Fig. 3.9, where the design substrate is Rogers RO3003 with thickness $h = 1.52$ mm.

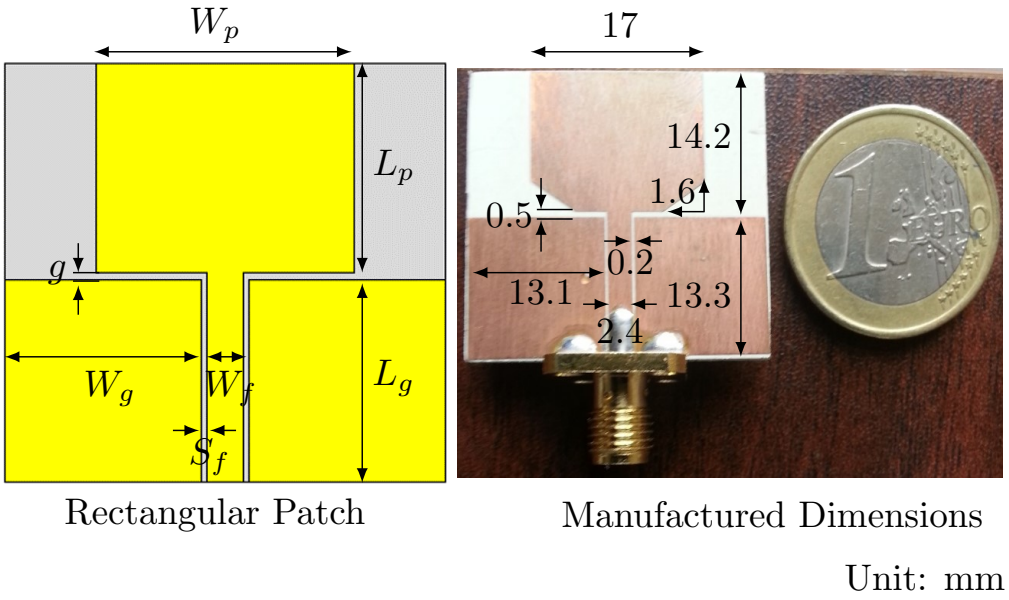

Figure 3.9: Manufactured CPW UWB monopole antenna.

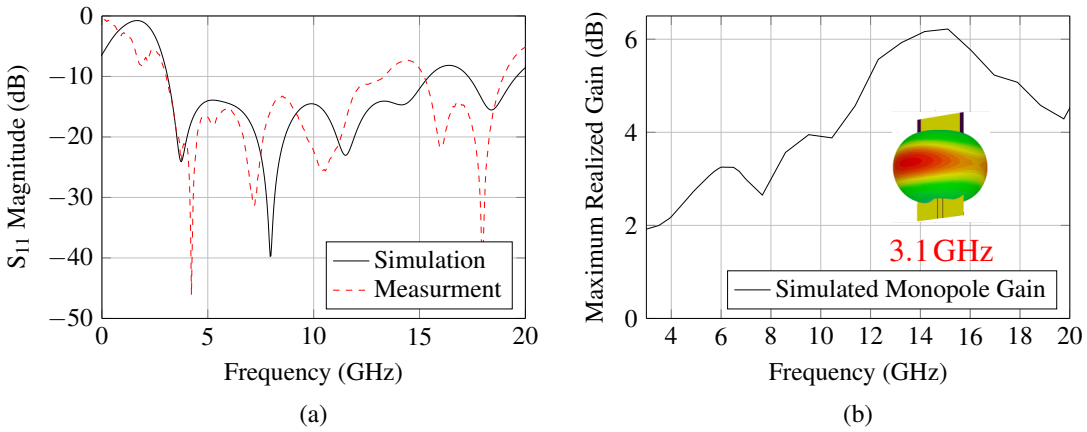

Figure 3.10: CPW UWB monopole antenna: (a) Simulated and measured return loss (b) Simulated gain with uniform omni-directional pattern.

3.4.2 CPW DGS Parallel L-Shape Encoding Resonators

Basically, the ground plane slot structures are employed in the microwave devices to filter out the undesired in-band frequencies [35], reduce the coupling between the adjacent antennas [36] and suppress the unwanted harmonics [36]. Therefore, these structures are engineered to provide the multi-stop band filter response with compact size. The CPW transmission line parameters are calculated [37] to produce 50 Ω characteristic impedance to be integrated with the designed CPW UWB monopole antenna. Hence, this CPW transmission line is loaded with the DGS

slots to constitute the encoding resonators. The proposed resonators are parallel L-shape slots which are etched in the ground plane along the propagation path of the CPW transmission line to symbolize the tag coding notches as illustrated in Fig 3.11. The slot parameters are the slot length L_s which is initially equal to the quarter wavelength at the desired notch frequency and the slot width W_s which affects the resonance bandwidth and the absorption level. Therefore, These parameters are optimized to attain equally spaced, narrow and highly attenuated stop band frequencies, while considering the implementation resolution.

As mentioned above, each DGS slot resonator provides a short circuit current path to the ground plane at a predetermined frequency generating a corresponding notch at that frequency. Therefore, the slot is modeled as a short circuit stub, where the input impedance is given by (3.12) considering the lossless case:

$$Z_{inp} = jZ_{0s}tan(\beta L_s) \tag{3.12}$$

where Z_{0s} is the characteristic impedance of the equivalent transmission line and β is the propagation phase constant. This short circuit stub model neglects the mutual coupling between the slots and also neglects the interaction between the slots fundamental resonance frequencies and the corresponding harmonics. However, this model is utilized for the initial design and the equivalent lumped components can be extracted using full wave EM simulators.

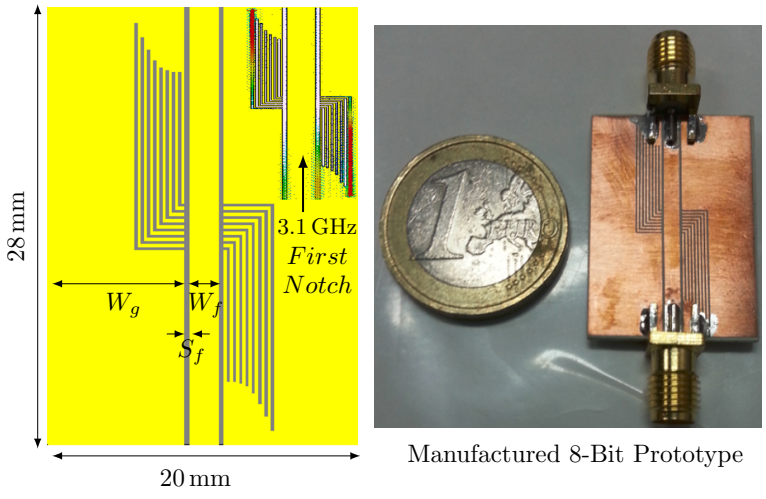

Figure 3.11: Manufactured CPW DGS L-shape resonator prototype.

An 8-Bit multi-stop band filter prototype is implemented with eight notches in the frequency range from (3.1 GHz to 6.1 GHz) as explained in Fig.3.12a. Subsequently, this 8-Bit prototype is integrated with the orthogonally polarized UWB monopole antennas as demonstrated in Fig 3.13

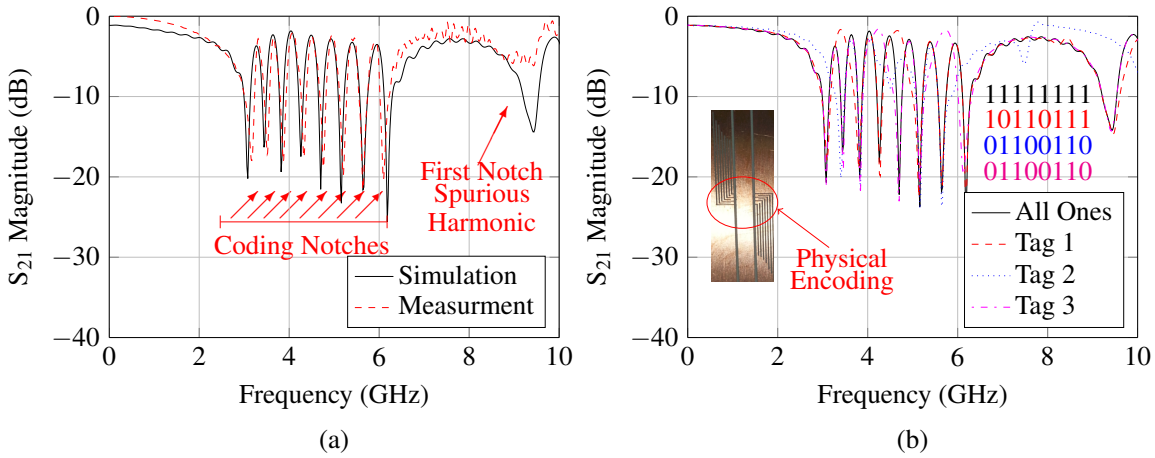

Figure 3.12: CPW DGS L-shape resonator: (a) Simulated and measured insertion loss of the 8-bit prototype. (b) Physical encoding methodology and various codes.

to compose the depolarizing tag. Furthermore, a novel encoding methodology is proposed to preserve the resonator current distribution while coding and so the notch position and bandwidth are retained. This methodology is based on placing short-circuit piece of copper at distinct positions along the slot length to disable or shift the slot resonance frequency. Thus, the short circuit is implanted away from the resonator end where the current magnitude is maximum as clarified in Fig. 3.11. Therefore, by deactivating a particular resonator, the coupling between the other resonators are not altered. Therefore, the resonance frequencies of the other resonators are not changed significantly while encoding as illustrated in Fig. 3.12b. This easy encoding and tuning property can preserve the same layout for all the tags while shorting the slots at discrete positions for obtaining various codes.

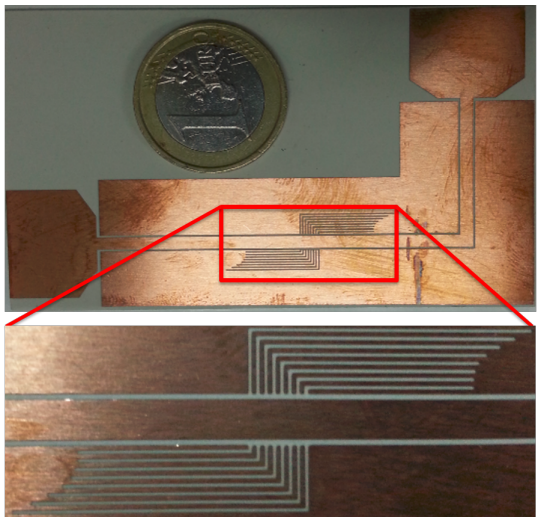

Figure 3.13: Retransmission based chipless RFID tag prototype.

Another key feature of the presented tag is that the spurious response begins at the third harmonic as illustrated in Fig. 3.12, unlike [31], where the second harmonic exists in the retransmitted tag response. Therefore, 18-bit coding capacity can be achieved considering 3-bit/GHz.

3.4.3 RFID System Indoor Measurements

The whole RFID system is verified in a real environment, where two tags with different codes are measured in the presence of various surrounding objects to validate the objectives mentioned above. Thence, the measurement setup as shown in Fig. 3.14 employs two orthogonally polarized transmitting and receiving LPDA antennas, which are connected to Vector Network Analyzer (VNA) to measure the tag's response. This VNA is utilized to measure the insertion loss (S_{21}) between the LPDA transmitting and receiving antennas. These antennas are far apart 40 cm while the tag is mounted on foam material in the middle position between the LPDA antennas. It is noteworthy that the tag retransmitted response is radiated in the forward and backward directions. This property qualifies the detection with both bi-static collocated and dislocated configurations and enables the reader antennas to be in-front or behind the tag. Moreover, a reference tag without any resonators is designed for calibrating the overall system variation with frequency, such as reader and tag antennas. This calibration is accomplished by deducting the measured tag response (S_{21}) from the reference tag measurements. Thus, nullifying the EM background noise and compensating the path loss.

As a consequence of the tag depolarization effect, the tag response can be determined without calibration as illustrated in Fig. 3.15a. In this condition, a smart notch detection algorithm is applied per each window to determine the notch existence. However, the reference tag measurement is exploited and thus a consistent threshold of -2 dB amplitude difference can be applied as explained in Fig. 3.15d. This feature is acquired by deducting the insertion loss of each coded tag from the reference tag insertion loss on the log scale to get the response of the resonators only. Therefore, the multi-stop band filter simulated insertion loss coincides with the measurement results of the complete tag structure as illustrated in Fig. 3.15c, d. Consequently, the detection efficiency is enhanced, the system complexity and latency are minimized.

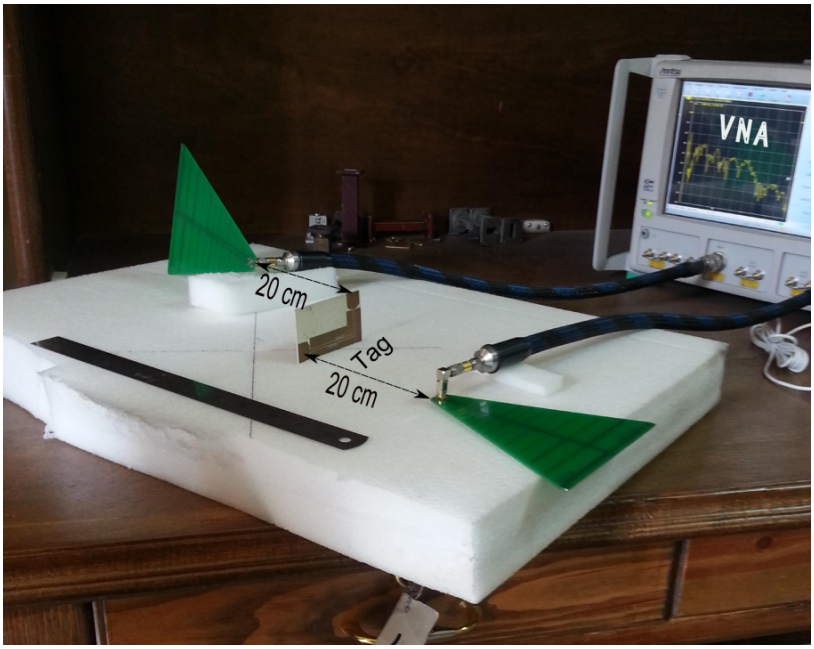

Figure 3.14: Retransmission tag indoor-measurement setup.

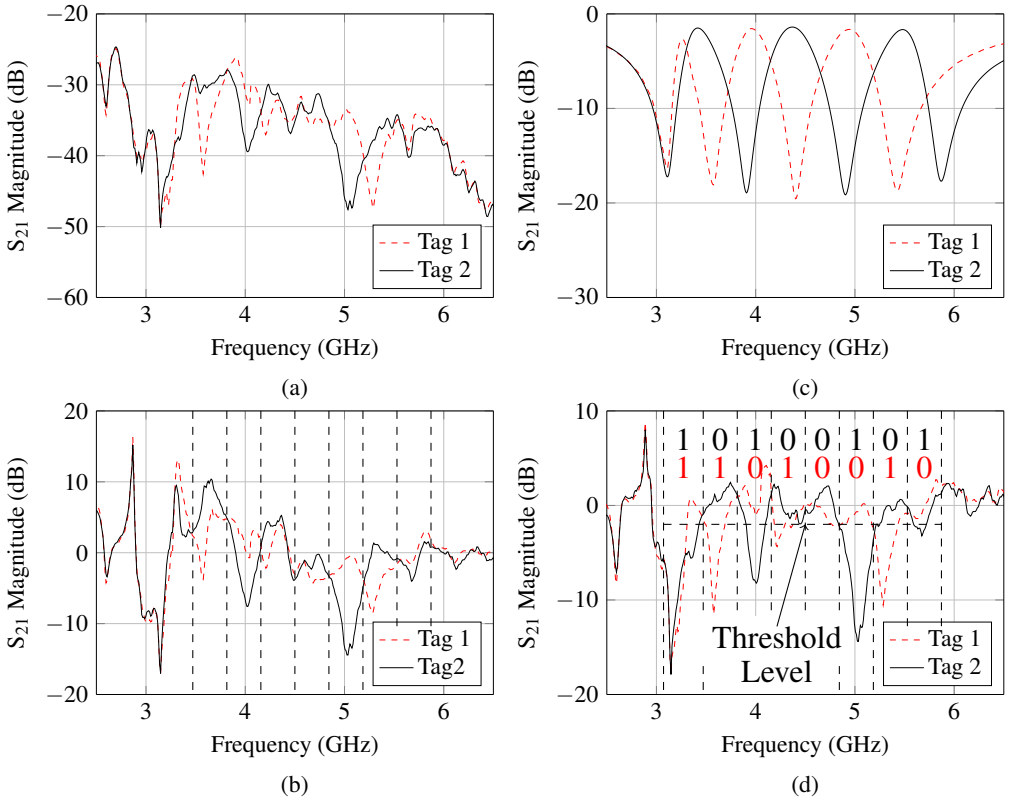

Figure 3.15: Retransmission tag system measurements: (a) Measured response of the two different tags before nullifying the background EM noise. (b) Measurements of the two different tags after nullifying the background EM noise. (c) The two port insertion loss (S_{21}) of the slot resonators only. (d) The measured response of the two different tags while exploiting the reference tag measurements deduction.

In comparison to the previous work [29], [32], where the tag measurements are performed inside the anechoic chamber with calibration procedures that nullify the background EM noise. This calibration is accomplished using the no-tag condition as the reference and subtracting the measured tag response (S_{21}) from the no-tag measurements. Consequently, the notches are not placed correctly at the designed frequencies. However, the measured tag response with the proposed calibration procedure overcome this problem.

In the NPM mentioned above tags, the tag-ID is based on the presence or absence of the notch. This one-to-one relation between the number of notches and coding bits is considered to be the basic modulation scheme. Therefore, the next section introduces a novel physical scheme that exploits the notch width to increase the coding capacity.

3.5 Notch Width Modulation Tags for High Coding Capacity

In this section, the notch bandwidth and its corresponding frequency position are exploited to increase the coding capacity as described in Fig. 3.16.

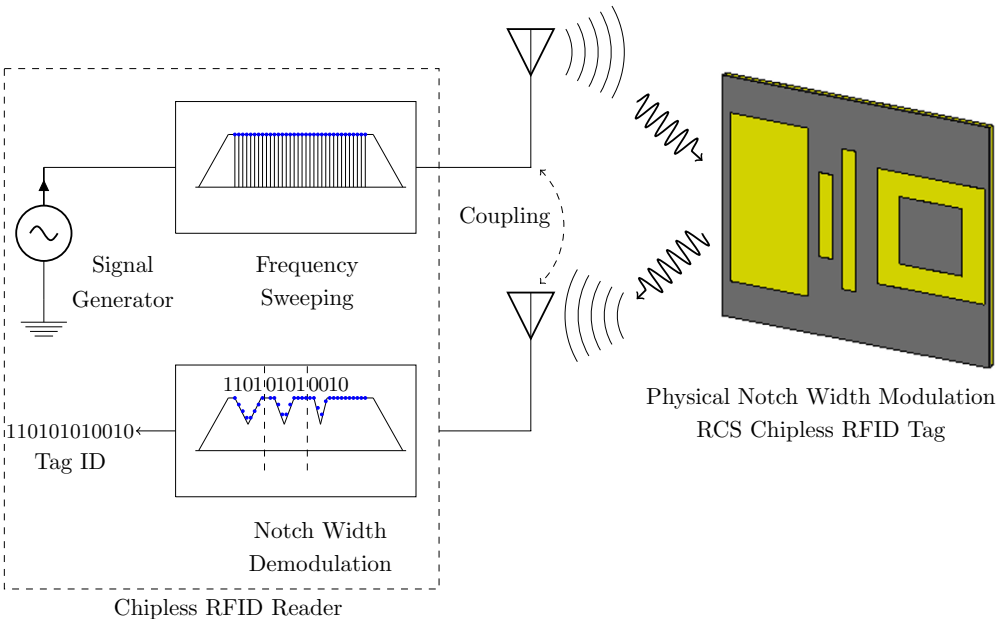

Figure 3.16: NWM RCS tags system description.

The chipless RFID system coding relies on exploiting either the co-polarized or the cross-polarized tag response. The basic modulation scheme is the NPM [11,38], where the existence of the notch at a particular frequency represents the logic-1 and the nonexistence mimics the logic-0. Accordingly, the operating spectrum is divided into windows and the notch is either switched

on or off for each window, which yields to (1-bit/coding window) as clarified in Fig. 3.17a. In order to increase the coding capacity, the coding window is divided into three positions, where each position codifies a different state. Therefore, four states are acquired for each window and thus two-bits coding capacity is achieved as explained in Fig. 3.17b [1]. However, this section introduces a novel physical modulation scheme which exploits the notch width to increase the coding capacity. Hence, exploiting the notch width parameter introduces ten possible coding states as described in Fig. 3.17c and achieves 72-bit coding capacity in 3 GHz bandwidth. The NWM scheme as demonstrated in Fig. 3.18 comprises three different arbitrary notch bandwidths ($BW1$, $BW2$ and $BW3$) and the corresponding frequency positions are (F_r, $F_r + \delta f$ and $F_r - \delta f$). Where, BW is the notch bandwidth, F_r is the notch resonant frequency and δf is the frequency shift which is utilized for coding purposes.

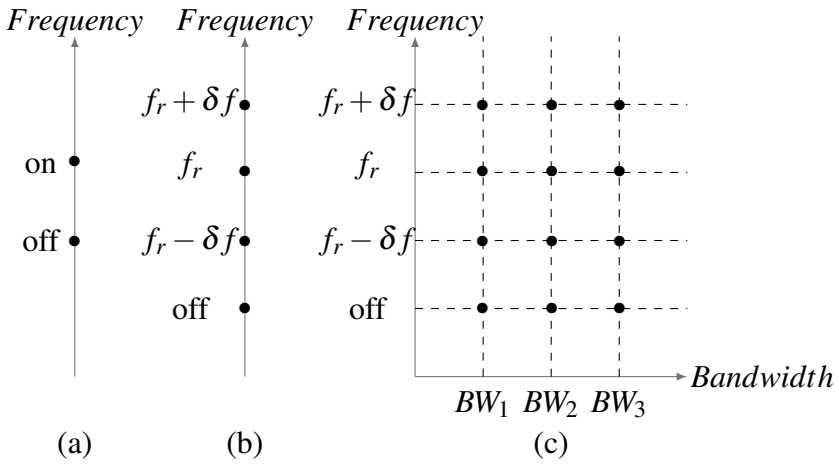

Figure 3.17: Constellation diagrams for: (a) The NPM scheme. (b) The frequency position encoding [1]. (C) The NWM besides the NPM.

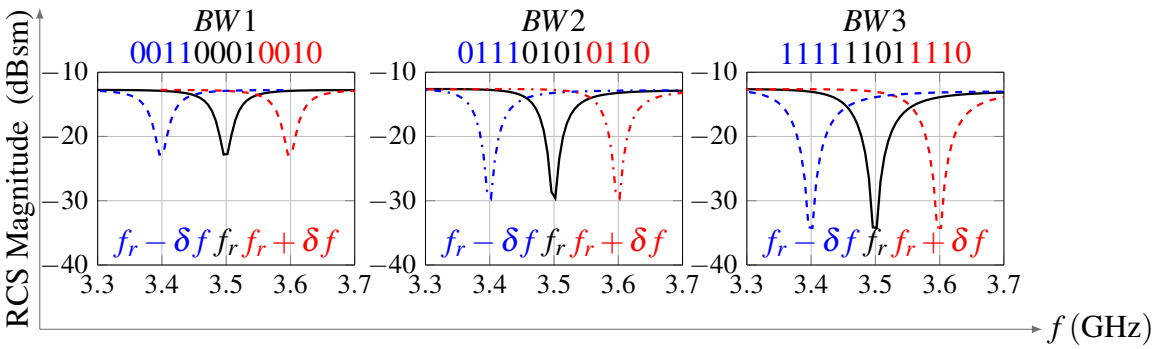

Figure 3.18: The principle of the NWM coding methodology.

3.5.1 NWM Chipless RFID Tag

There are challenges which impede the realization of the aforementioned NWM scheme. The first challenge is that the notch width is approximately fixed for the same resonator with the same substrate parameters. Furthermore, the notch bandwidth varies with frequency and affected by the relative distance between the resonators. Another important handicap is that the notch pattern is dramatically influenced by the presence or absence of the nearby resonators. Therefore, a novel tag structure considering the aforementioned objectives and limitations is proposed. The proposed tag structure consists of three variant FSS shapes specifying three different quality factors. These resonators are the dipole, the rectangular ring and the patch corresponding to the first, the second and the third coding bandwidths respectively. Thus, the notch position is specified by the resonator length while the bandwidth is determined by the resonator quality factor. Hence, to anticipate this variation, the coding spectrum is divided into three windows and the relative notch widths are studied for each window. This ratio is almost kept constant per each window. Therefore, the tag is capable of introducing these various notch widths at any prescribed frequency of these windows.

First, the notch patterns of these elements are calculated and optimized per each window to demonstrate the three different notch widths. After that, a smart arrangement of these elements is utilized in the tag specified area. This arrangement of the resonators allows for a sufficient good decoupling of their EM responses to preserve the tag response against frequency shift as well as bandwidth variation that resulted from inserting or removing a coding element. Then, the images of these notches as shown in Fig. 3.19 are transferred to the RFID reader to predict the relative bandwidth variation with frequency.

3.5.2 NWM Tag Simulation and Measurements

As shown in Fig. 3.20, three different tags demonstrating all possible combinations are designed, simulated and measured to prove the concept. Hence, the RCS frequency response of the designed tags reveals the flexibility of controlling the bandwidth as well as the position of the introduced notches all over the specified operating frequency range as explained in Fig. 3.22a. Accordingly, the NWM scheme encodes 4 bit information per single resonator. Furthermore, it's observed that up to 6 windows can be allocated within 1 GHz representing the 72-bit coding capacity in 3 GHz bandwidth. Each dotted line represents f_r as mentioned in the previous section and the arrows represent the shift to each f_r.

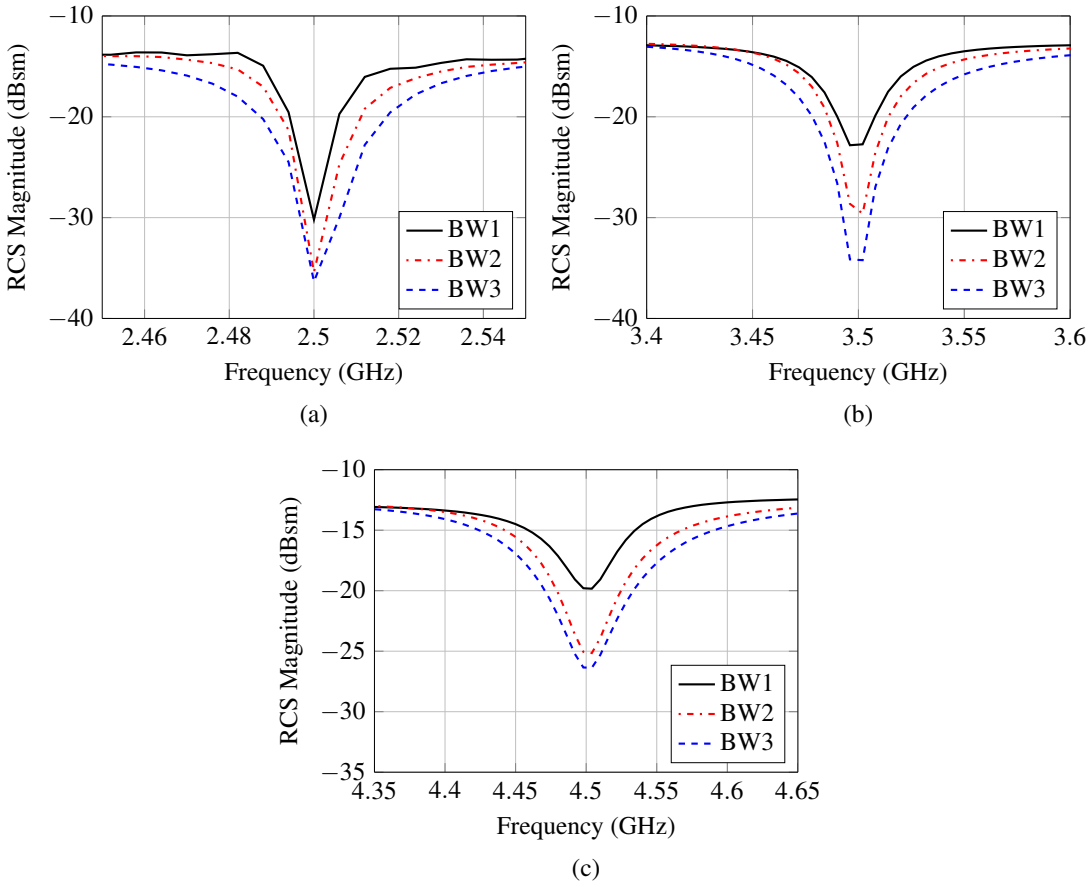

Figure 3.19: Notch patterns for the three different windows using CST-Microwave Studio EM simulator: (a) First window (b) Second window(c) Third window

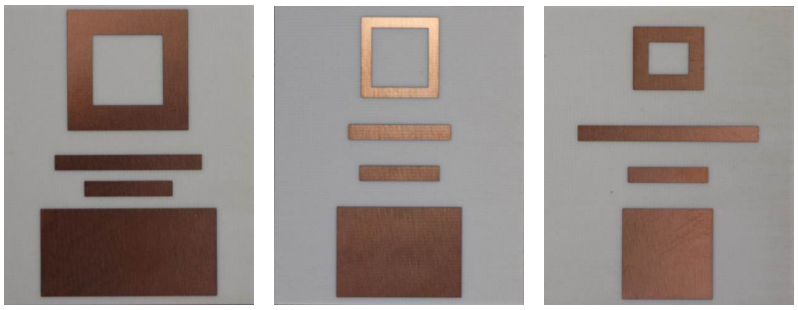

Figure 3.20: Three different tags demonstrating the physical NWM approach

The Bi-static RCS measurement setup of the NWM tags as illustrated in Fig. 3.21 employs two LPDA antennas in the reader side. A copper plate is placed between the two interrogator's antennas to minimize the effect of each antenna on the other. Hence, the tags are positioned at 15 cm distance from the reader antennas. The reader is implemented utilizing the Universal

Software Defined Radio Peripheral (USRP) N210 [39] and the CBX daughter board (1.2 − 6 GHz) [40] for identification and detection. A frequency sweeping mechanism is applied such that a cosine wave is transmitted from 2 GHz to 5 GHz with a frequency step of 10 MHz. At the same time, the receiver monitors the reflected signal from the tag (because the CBX daughter board is full duplex). Then, the reader starts the processing phase for applying the (Window Based Singular Value Decomposition (WB-SVD)) algorithm and the designed decoding technique [41]. Accordingly, the effectiveness, reliability of the proposed tag design and the introduced physical modulation scheme are determined.

The tag response is extracted by deducting the reflected signal power by the tag front from the received power reflected by the tag's ground plane as illustrated in (3.13).

$$R^i_{\text{measured}} = R^i_{\text{front}} - R^i_{\text{back}} \text{ (dB)} \tag{3.13}$$

where R^i_{measured} is the measured backscattered signal for tag i, the backscattered signal from the tag front is R^i_{front} and R^i_{back} is the backscattered signal power from the tag ground plane (the copper side). Each tag has 4 resonators and each resonator encodes 4-bit according to the notch bandwidth and the corresponding frequency position. Fig. 3.22 illustrates the total backscattered signals received from each tag in the USRP reader side. Besides, the proposed decoding technique is applied to the received signal and th WB-SVD algorithm is realized. The measurement results illustrate a good match with the simulation as explained in Fig. 3.22. Hence, the validity of the introduced modulation scheme and the proposed tag design are ensured in a realistic system. As described in the previous section the notch width is exploited to increase the coding capacity. However, the notch pattern is sensitive to the environmental reflections. Moreover, the measurements are conducted inside an anechoic chamber, where a copper plate should be placed between the reader antennas to minimize the effect of coupling on the notch pattern. To minimize these clutter reflections, the polarization diversity between the reader interrogation signal and the tag response is proposed. However, the retransmission tag introduced previously requires two orthogonally polarized UWB antennas, resulting in complex tag structure and large size. The following section solves these design dilemmas where a depolarized tag response is attained from the RCS based tag which is illuminated with a linearly polarized wave.

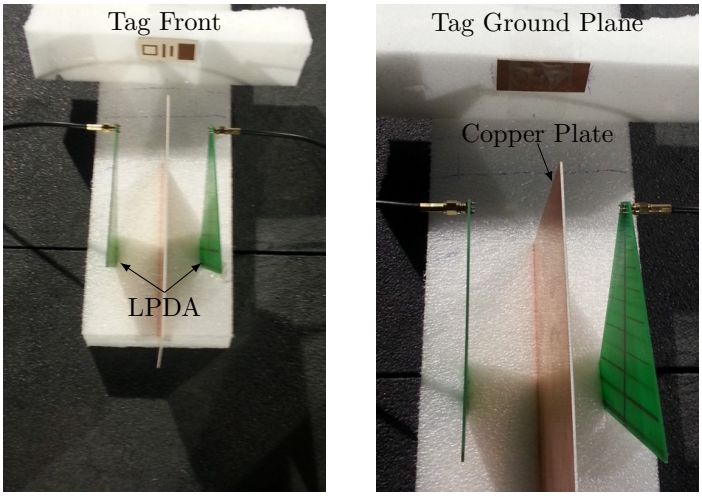

(a) (b)

Figure 3.21: Measurement setup inside the anechoic chamber: (a) NWM tag front. (b) NWM tag ground plane.

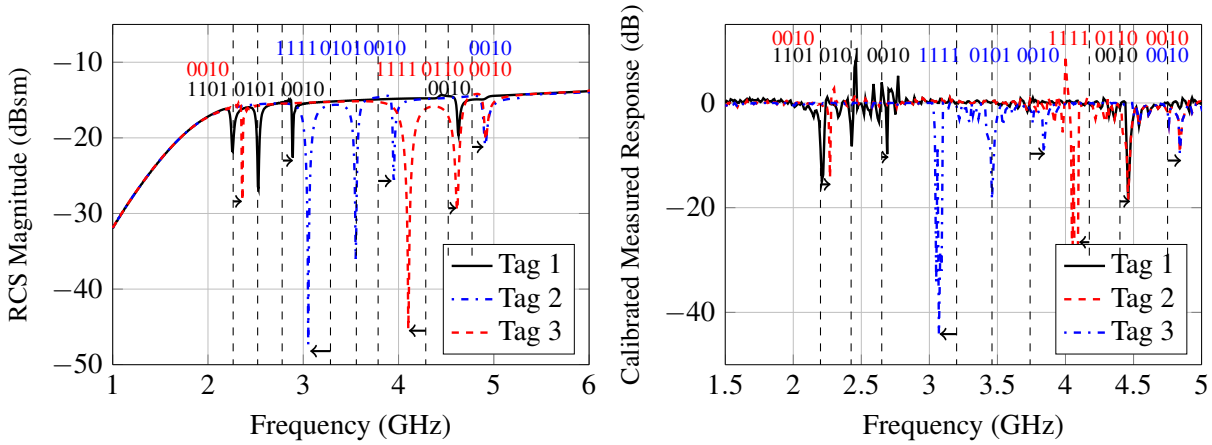

(a) (b)

Figure 3.22: The NWM tags simulation and measurment: (a) Simulation results for the designed NWM tags. (b) USRP measured results for the NWM manufactured tags.

3.6 A Novel Co/Cross-Polarizing Chipless RFID Tags for High Coding Capacity and Robust Detection

This section introduces a novel physical modulation scheme where both the co-polarized and the cross-polarized tag responses are exploited to increase the coding capacity, conserve the spectrum and preserve the tag size. The corresponding system description is illustrated in Fig. 3.23, where the reader illuminates the tag with a linear polarized wave. The tag in turn physically modulates

the reader signal and backscatters a notch response in the co-polarization direction and a peak response in the cross-polarization direction. Consequently, the tag signature is encoded into N/P format in two orthogonal planes. Therefore, the existence of the notch or the peak resonance resembles the OO-N/P modulation and the frequency shift emulates the N/P-P modulation as illustrated in Fig. 3.24.

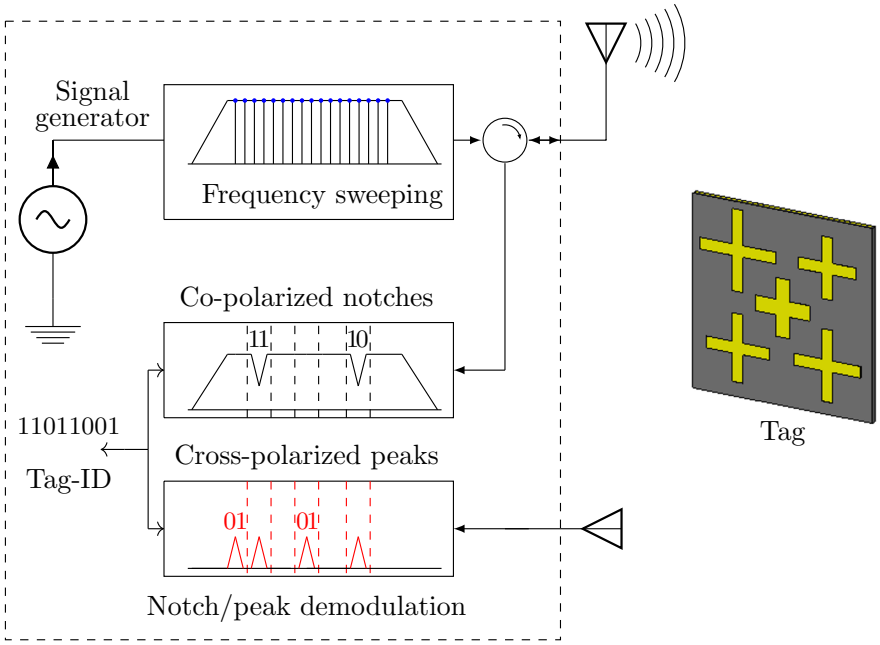

Figure 3.23: System description for the OO-N/P and the N/P-P physical modulation technique illustrating the co-polarized notch response, the cross-polarized peak response and the realizing tag structure.

The coding spectrum is divided into windows and per each window the notch can take one of three different positions and so the peak can be tuned to any of these positions as illustrated in Fig. 3.24. Consequently, two bits are defined in the co-polarization plane and the other two are located in the cross-polarization plane. Thus, four bits coding capacity for each crossed dipole is achieved per each window. The notch frequency shift value is denoted by δf and the peak frequency shift is denoted by ε. These two shift values can be the same or different as explained. The corresponding constellation diagram is illustrated in Fig. 3.25 where nine possible states are apparently feasible besides the off state.

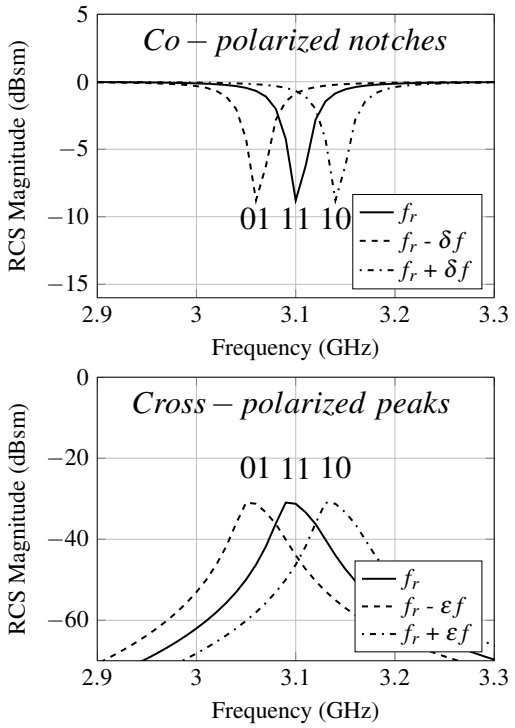

Figure 3.24: The OO-N/P and the N/P-P coding principle utilizing both the notch and peak positions in two orthogonal planes.

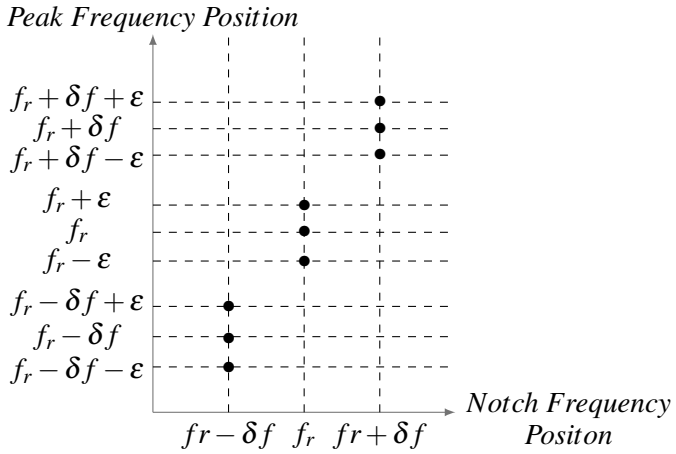

Figure 3.25: The constellation diagram of the OO-N/P and N/P-P physical modulation schemes.

3.6.1 N/P Co/Cross-Polarizing Chipless RFID Tag

The designed tag consists of asymmetry crossed dipoles which resonate at a half wavelength of its maximum length. Each crossed dipole introduces a filtering property in the co-polarization direction and a resonance peak in the cross-polarization direction. Therefore, the crossed dipole enables the encoding in two divergent polarizations separately. The designed crossed dipoles

backscatter the resonant notches in the plane of the incident wave (vertical plane) and the resonant peaks in the orthogonal polarization direction (horizontal plane) simultaneously. Thus, the coding capacity is increased. Furthermore, the crossed dipole is a spectrum-efficient resonator where the resonance bandwidth is about 40 MHz.

A parametric study is constructed to get the best cell parameters for the substrate and the dipole dimensions. It is revealed from the study that the thinner dipole width can reduce the resonance bandwidth but it deteriorates the formation of the corresponding peak as described in Figs. 3.26a and b. Besides, the lossy high dielectric substrates exhibit high absorption levels at the expense of low radiation peaks as depicted in Figs. 3.26c and d. Therefore, the dipole widths are tuned to preserve the shape uniformity of the response and the lengths are varied corresponding to the prescribed resonance frequencies. The utilized substrate is Rogers Ro6010 with 0.64 mm thickness.

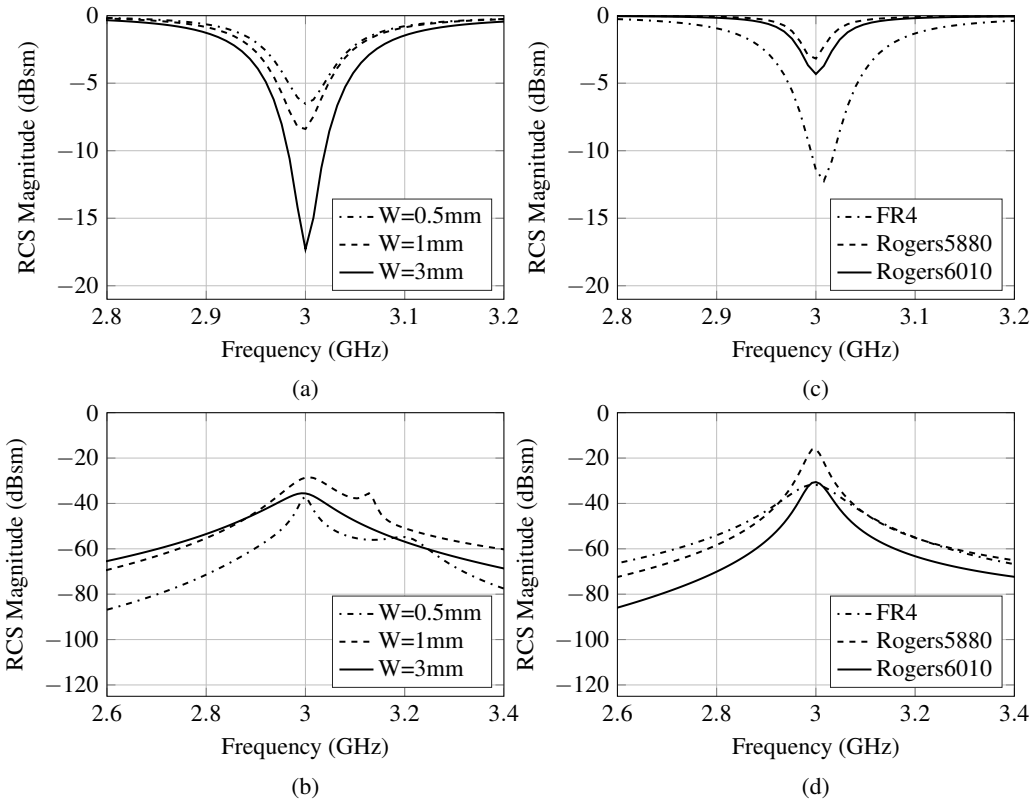

Figure 3.26: Parametric study for the crossed dipole dimensions and substrate parameters: (a) Co-polarized notches for different dipole widths. (b) Cross-polarized peaks response for different dipole widths. (c) Co-polarized notches for various substrates. (d) Cross-polarized peaks response for various substrates.

3.6.2 Co/Cross-polarizing Tag Simulation and Measurements

Two different tags that demonstrate all possible combinations are designed and simulated to prove the robustness of the introduced physical modulation scheme. The RCS frequency response of these tags inspires the flexibility to control the notch and peak positions in two orthogonal directions simultaneously as illustrated in Figs. 3.27a and b. Accordingly, this scheme encodes four-bit information per crossed dipole. Hence, two bits are codified in the form of notches in the co-polarized plane, and the other two bits are codified in the form of peaks in the cross-polarized plane. Therefore, 100-bit coding capacity is achieved in 3 GHz operating frequency range, considering that the dipole resonance bandwidth is 40 MHz and thus 120 MHz coding window. Based on literature, this is the highest coding capacity that can be achieved within this frequency range. Furthermore, the simulation results shown in Fig. 3.27 verifies that there are two peaks for each window. One of these peaks results from the horizontal encoding dipole that ensures the notch frequency position in the co-polar direction, the other peak corresponding to the vertical encoding dipole which is utilized for coding in the cross-polar direction. Therefore, the depolarized tag response is used to minimize the environmental reflections and enhance the detection reliability. The following section investigates the problem of placing the tag on different material objects.

The Co/Cross-polarizing tags are verified in a real indoor environment where two tags with two different codes are measured in the presence of various surrounding objects. The notches and peaks of the first tag are designed to be in the middle of the coding windows and thus the second tag code demonstrates the notch and peak frequency shift. Each dotted line represents a start of a new coding window and thus the arrows represent the frequency shift with respect to the reference positions as illustrated in Fig. 3.13. The real-world testbed setup is described in Fig. 3.28 where the USRP [39] and two LPDA antennas are employed to realize the reader communication process. The tag is mounted on a foam material in the broadside direction of the antennas at a distance of 20 cm and 10 cm for notch and peak detection respectively. The tag response is extracted by deducting the reflected signal power by the tag front from the received power reflected by the tag's ground plane as illustrated in (3.13).

The measured response of the co-polarized notches as shown in Fig. 3.29a is slightly shifted right with respect to the simulation notches illustrated in Fig. 3.27a. Therefore, the corresponding peaks in the orthogonal directions verify the newly changed positions as illustrated in Fig. 3.27b. Accordingly, the resonant peaks resulted from the vertical encoding dipole undergo the same

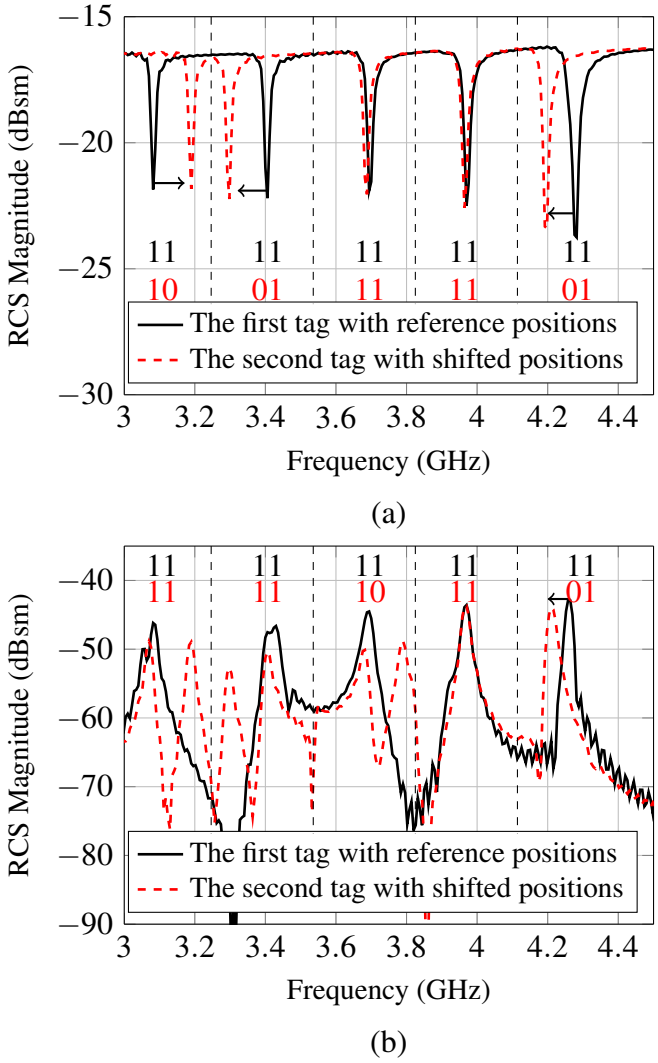

Figure 3.27: The OO-N/P and N/P-P physically modulated tags simulations: (a) The simulated co-polarized notches. (b) The simulated cross-polarized peaks.

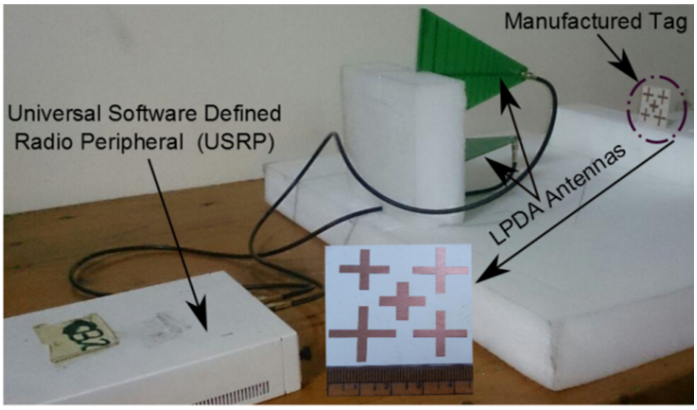

Figure 3.28: Indoor office setup for the Co/Cross-polarizing tags.

shift. Furthermore, any nearby background object does not depolarize the incident wave like the crossed dipole. Thus, the detection robustness chipless RFID system could be enhanced.

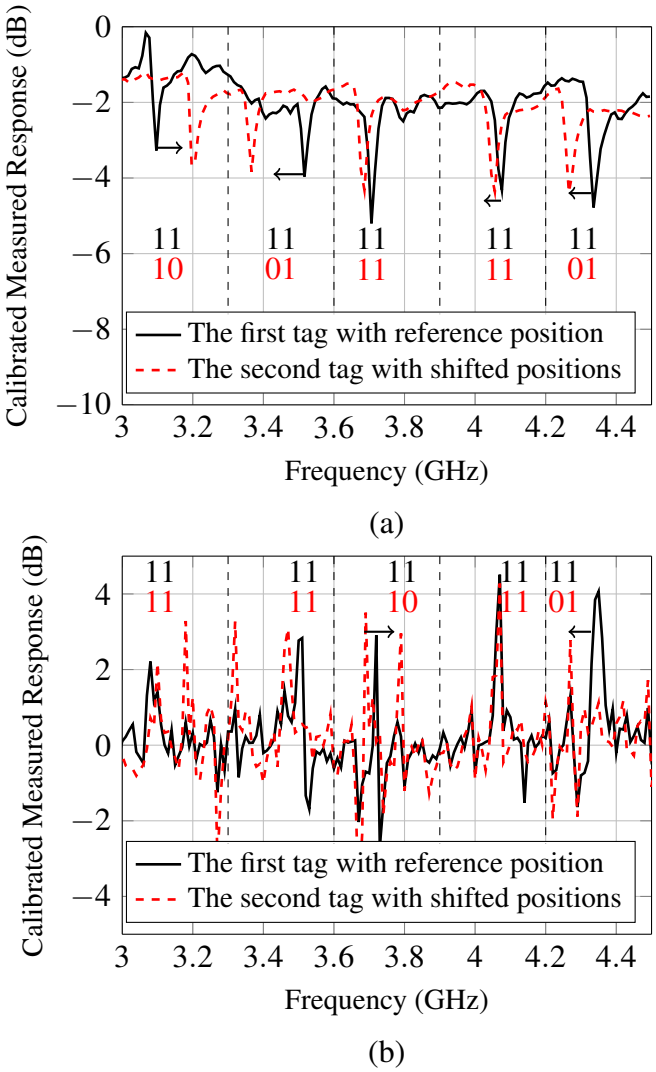

Figure 3.29: The OO-N/P and N/P-P physically modulated tags measurements: (a) The measured co-polarized notches. (b) The measured cross-polarized peaks.

3.7 Conclusive Discussion

In this chapter novel physically modulated chipless RFID tags are introduced. First, the NPM tags with novel encoding techniques are presented. Moreover, the number of coding resonators could be increased without increasing the tag size. Thus, 14-bit coding capacity is achieved for the RCS-based tags and 18-bit coding capacity is acquired for the retransmission based tags. However, their literature counterpart, the coding capacity is less with bigger tag size and larger

occupied frequency range. Afterward, the notch width is exploited to increase the coding capacity and enhance the coding efficiency by encoding 4-bit per single resonator. Thus, 72-bit coding capacity is achieved. Then, the co/cross polarizing tags are introduced where the depolarized plane is exploited to increase the coding capacity and thus 100-bit coding capacity can be achieved. Up to the authors' knowledge, this is the highest coding capacity that can be achieved with this occupied frequency range and tag size. Furthermore, the depolarized tag response is exploited to minimize the environmental reflections and thus enhancing the reading robustness. The unique features of the introduced tag compared to the state of the art contributions are summarized in table 3.2. The introduced tags outperforms the previous contributions from the aspect of coding density, occupied spectrum, and tag size.

Table 3.2: Summary of the proposed physically modulated chipless RFID tags

Resonator Type	Physical Modulation	No. Bits per Single Element	Tag Size (cm^2)	Coding Capacity (bit)	Coding Density (bit/cm^2)	Frequency Range (GHz)
Circular Ring [12]	**NPM**	**1**	**4×4**	**14**	**1.11**	**2-5**
L-Shape DGS [11]	**NPM**	**1**	**5×8**	**18**	**0.45**	**3-9**
Dipole, ring and patch [13]	**NWM**	**4**	**4.5×5**	**72**	**3.6**	**2-5**
Crossed Dipole [14]	**OO-N/P N/P-P**	**4**	**4.5×4.5**	**100**	**4.8**	**2-5**

The influence of placing the tag on items with different material properties is investigated. These materials are characterized by their conductive and dielectric properties. Finally, the limitations of increasing the tag coding spectrum are discussed.

3.7.1 Detection Robustness Discussion

This subsection investigates the impact of tagged material properties on the tag co-polarized notches and cross-polarized peaks. The presence of the ground plane is a key point to make the tag less sensitive to the tagged item. The item can be constituted from dielectric or conductive materials. The dielectric materials are specified by the permittivity (ε_r) and loss tangent ($\tan\delta$). The material permittivity influences the resonance position while the loss tangent affects the

losses in amplitude, especially for the ungrounded tags. However, two solutions can be adopted to mitigate these practical limitations. The first one is to make the holding object properties as a part of the tag design. An alternative solution is to reserve two frequencies outside the coding spectrum to probe the amount of frequency shift caused by the material.

On the contrary, if the tag is near to metal plate or a water-filled container, the RCS value and shape are deteriorated [42]. Hence, the tag is placed on an aluminum surface and a variable sheet size is considered as shown in Fig. 3.30. The echo of this copper surface acts like a clutter signal with strong reflection. Therefore, the co-polarized notches are gradually diminished with the increase of the aluminum surface area as illustrated in Fig. 3.31a. However, the depolarized peaks are clearly discriminated as depicted in Fig. 3.31b. Consequently, the Co/Cross-polarizing physically modulated tag is favored with the conductive objects. The material object can be any other material and shape, but only these two examples are discussed in this chapter.

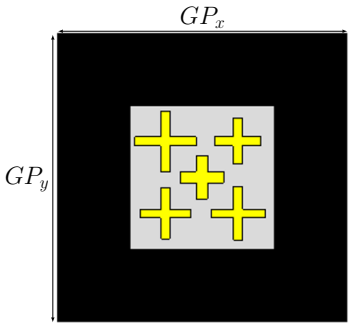

Figure 3.30: The RCS tag is placed on metallic or dielectric platform.

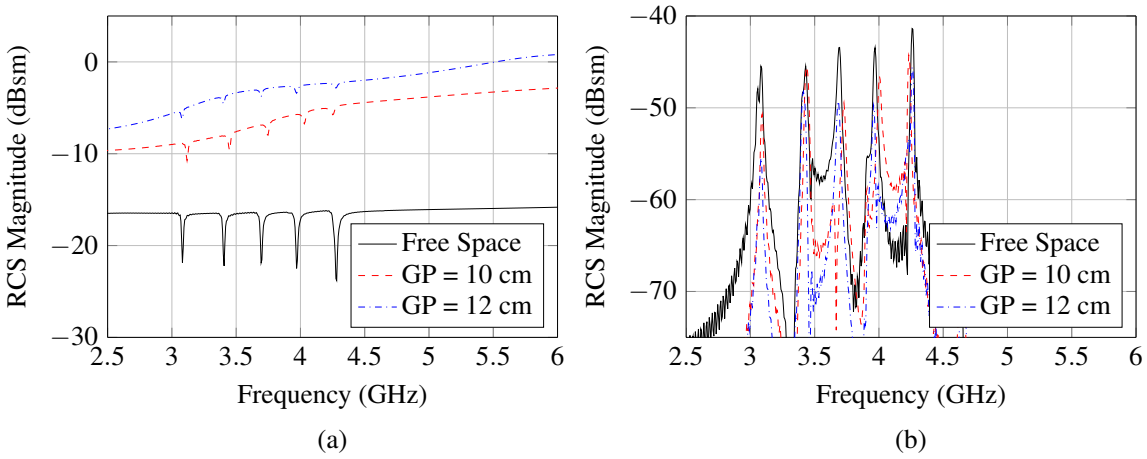

Figure 3.31: The response of the RCS tag which is placed on metallic surface: (a) The co-polarized notch response (b) The cross-polarized backscattered peaks.

3.7.2 Frequency Increasing Possibilities and Limitations

Basically, raising the operating frequency leads to an increase in the RCS value. In this subsection the RCS frequency response is investigated at higher frequencies to examine the possibilities of shrinking the tag size. Thus, a narrow-band half-wavelength dipole is placed over a grounded substrate as shown in Fig.3.32. The dipole resonant length is varied while keeping the same substrate parameters. The RCS frequency response as shown in Fig. 3.32 illustrates that the notch gets wider and less deeper while increasing the resonance frequency of the dipole.

Fundamentally, this anticipated RCS frequency response can be interpreted from the differential RCS reduction point of view which can be defined as the ratio of the resonator RCS over the ground plate RCS:

$$Diffrential\ RCS : \sigma^{\circ}(f) = \frac{\sigma_{ID}}{\sigma_{carrier}} \tag{3.14}$$

where, $\sigma^{\circ}(f)$ is the differential RCS, σ_{ID} is the RCS of the dipole and $\sigma_{carrier}$ is the RCS of the grounded carrier substrate. Therefore, one possible solution to rescue the notch pattern is to reduce the carrier substrate size. However, the RCS level is also reduced as illustrated in Fig. 3.33. Reducing the substrate length and width by a factor of two leads to a reduction in the RCS level by 6 dB. Hence, the tag is invisible to the radar signal of frequencies less than 4 GHz. The other solution to keep the same RCS value is to add dummy resonators in a way to sharpen the notch and avoid coupling as explained in Fig 3.33. Adding supplementary resonators in a smart way will increase the value of the stored energy at the same resonance frequency and thus compensate for the notch depth reduction.

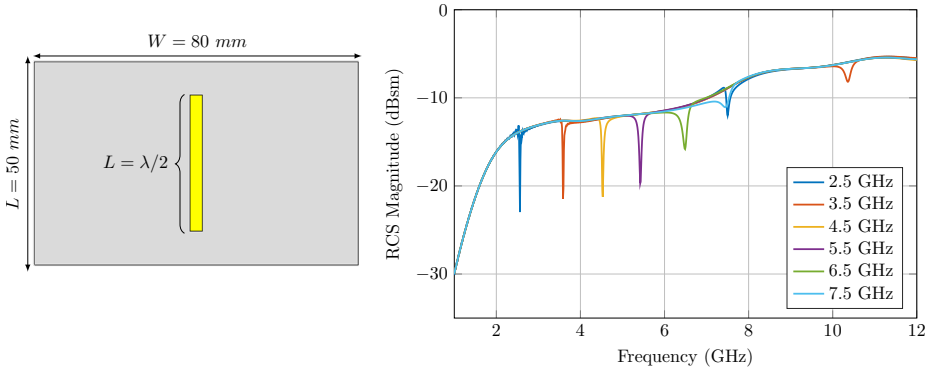

Figure 3.32: Half-wavelength dipole RCS response at different resonating lengths illustrating the notch deformation with increasing frequency.

The NWM tag is utilized to complete the investigation. The previous coding spectrum of

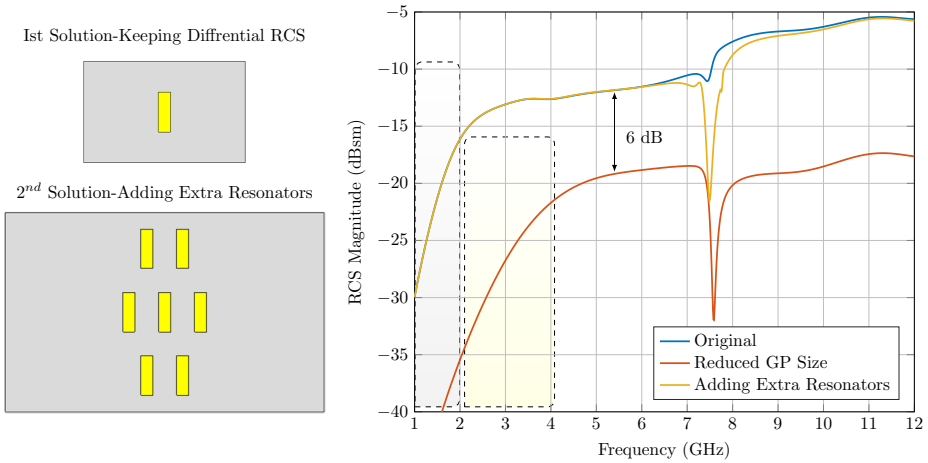

Figure 3.33: Notch survive methodologies at high frequencies by either keeping the differential RCS value or compensating for the notch depth decrease.

this tag was chosen to be from 2 GHz to 5 GHz. In this study the coding BW is shifted to be from $(4-7\,\text{GHz})$, so doubling the frequency points while keeping the occupied BW fixed. Therefore, the notch pattern of the second tag introduced previously in Section 3.5 is utilized to be the baseline of the study. The tag resonators dimensions are scaled down to have one gigahertz shift frequency response for each iteration. Consequently, the RCS frequency response of the tag evolutions as shown in Fig. 3.34 reveals that the notch width increases with frequency. Moreover, the notch level dynamic range is reduced. Therefore, to recover the notch dynamic range, the carrier substrate size is to be reduced and so the tag size. The other preferred solution is to insert extra resonators while fixing the tag size to keep the maximum RCS value. Thus, the enhanced tag response as illustrated in Fig. 3.34 reveals the capability of increasing the tag operating frequency while keeping the maximum RCS value, increasing the notches dynamic ranges and keeping their patterns.

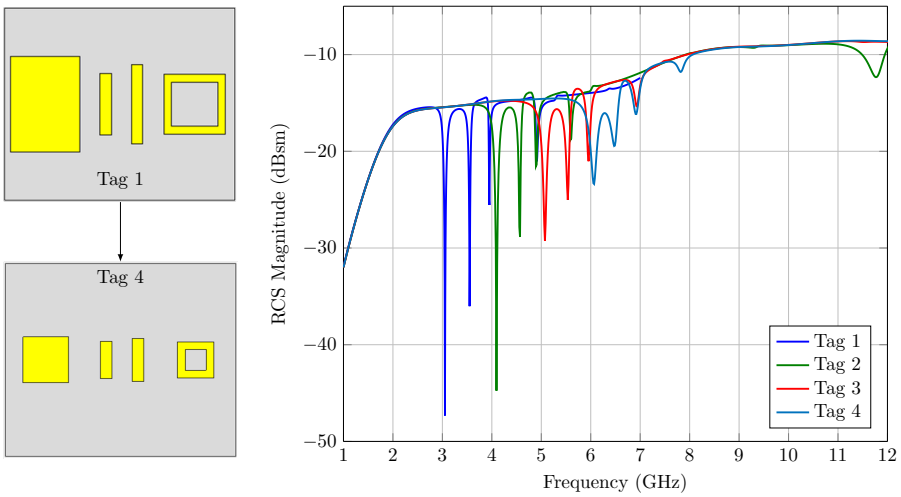

Figure 3.34: Frequency increase investigation utilizing the NWM tag: Scaling down the resonators dimensions as explained on the left side and the corresponding RCS frequency response for the NWM tag evolutions on the right side.

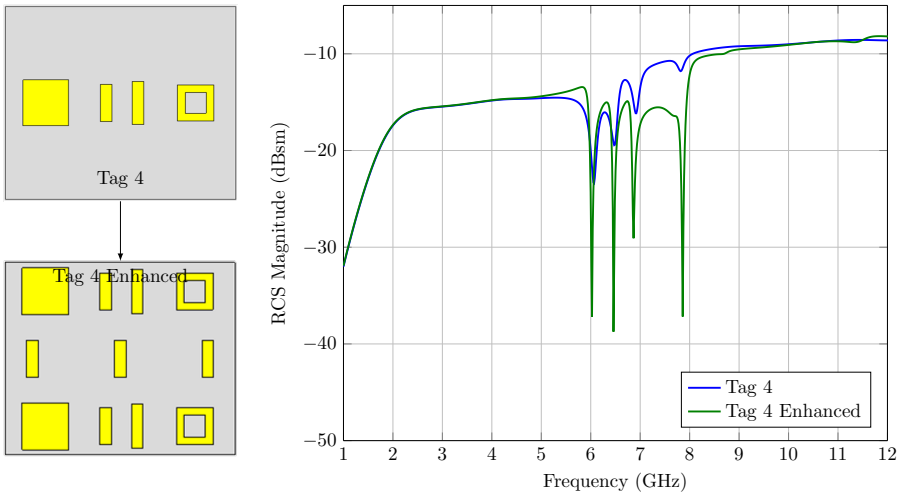

Figure 3.35: Compensating the notch pattern deformation that happened to the fourth tag by adding auxiliary resonators.

It is concluded that the notch bandwidth is broadened at higher frequencies and beyond a certain limit it is concealed by the increased RCS value of the carrier substrate. Therefore, the coding capacity is reduced. However, the RCS level is increased, and thus the detection and coverage can be enhanced. This enhancement is acquired by keeping the tag size and inserting supplementary resonators to recover the notches dynamic ranges and patterns.

4 REFLECTARRAY READERS

This chapter proposes the utilization of the RA antenna in the reader side aiming at increasing the reading range, minimizing the environmental reflections and attaining a lot of novel capabilities that can not be provided by the conventional antenna systems. First, a Proof-Of-Concept (POC) RA antenna operates at 5.8 GHz and uses the LPDA as a feeder is demonstrated. Although the LPDA antenna is not a standard feeder because of the non-constant phase center position, the designed prototype is successfully implemented, measured and verified inside the Anechoic Chamber (AC). Hence, this POC RA antenna is four times narrower beam width than the feeder beam and thus 6 dB higher in gain with -10 dB dB SLL. Moreover, the operating bandwidth is about 300 MHz which can accommodate few bits. However, the FC chipless RFID system requires UWB range of frequencies to provide multiple bits. The conventional antenna arrays can not provide this UWB operation. Even though, the RA antenna is also suffering from a bandwidth limitation, a novel UWB RA antenna dedicated to the chipless RFID readers is accomplished. This RA antenna achieves UWB range of frequencies from 4 to 6 GHz fulfilling the requirements of the FC chipless RFID systems. Therefore, this developed UWB RA antenna is successfully integrated with the physically modulated chipless RFID tags, and a reading range of 1 m is achieved. To the best of the author knowledge, this is the highest reading range achieved in the FC chipless RFID systems, considering real-world indoor environment and software defined radio reader. After that, a low cross-polarization level dual-polarized RA antenna is presented. This RA antenna is proposed to be utilized with the co/cross polarizing tags. Finally, a successful implementation of an electronic beam steering RA antenna is introduced. This novel beam steering RA antenna system enhances the reading robustness and can precisely locate the chipless tags. In this regard, a novel unit cell that is able to electronically control the reflected phase at different discrete frequencies utilizing a single varactor diode is proposed. Therefore, the UWB operation is attained and a scanning range of $\pm 50^\circ$ is achieved. Moreover, the steered beam is four times narrower than the feeder beam and four times higher in gain. The contents of this chapter have been partially published in [43, 44]

4.1 Introduction

One of the major handicaps of the chipless RFID systems is the short reading range, which is estimated to be few centimeters less than 40 cm [11]. This reading range is calculated based on (4.1), considering symmetrical system, i.e., the reader transmitting and receiving antennas are in the same position:

$$r_{range} = \sqrt[4]{\frac{G_T G_R \lambda^2 P_T}{(4\pi)^3 P_{min}} \sigma} \tag{4.1}$$

Where r_{range} is the reading range, G_T is the reader transmitting antenna gain, G_R is the reader receiving antenna gain, λ is the wavelength, σ is the tag radar cross section, P_T is the transmitted power and P_{min} is the reader sensitivity.

One of these limitations results from the restrict Federal Communications Commission (FCC) UWB power regulations. In [45] a novel methodology to increase the reading range by best utilize these regulations is introduced. This methodology states that 0 dBm peak level of emission is allowed within 50 MHz bandwidth [46]. So, the tag interrogated with a frequency sweeping mechanism instead of UWB pulse transmission, which is limited to -41.3 dBm/MHz, i.e., -24.31 dBm/50 MHz. Hence, this methodology is applied on the NPM ring structure tag where the RCS value of the logic-1 is -30 dBsm and that of the logic-0 is -10 dBsm. To detect the notch clearly, at least 5 dB dynamic difference is required between the notches and peaks. Therefore, the reading range with the received power is calculated at 5 GHz as explained in Fig 4.1, assuming unity gain transmitting antenna ($G_T = 0$ dBi) and that the receiving antenna gain is ($G_R = 10$ dBi). As a consequence, considering that the receiver sensitivity is -80 dBm, the minimum RCS value that can be detected at 2 m is about -20 dBsm and thus the notch dynamic range is -10 dB. However, this theoretical reading range can not be reached in a real-world scenario because of the cluttering signals, the transmitter leakage, etc.,

Hence, the reading range is also affected by the environmental reflections and the multi-tag interference; both are contaminating the tag RCS frequency response. Thus, the problem of multi-tag interference is investigated, where multiple NPM RCS tags with various codes are simulated simultaneously. The simulation setup as described in Fig. 4.2 consists of two different tags separated by a minimum distance d. This separation is determined from the far-field classical equation given by (4.2) and also verified by the full wave simulation.

$$d = \frac{2D^2}{\lambda} \tag{4.2}$$

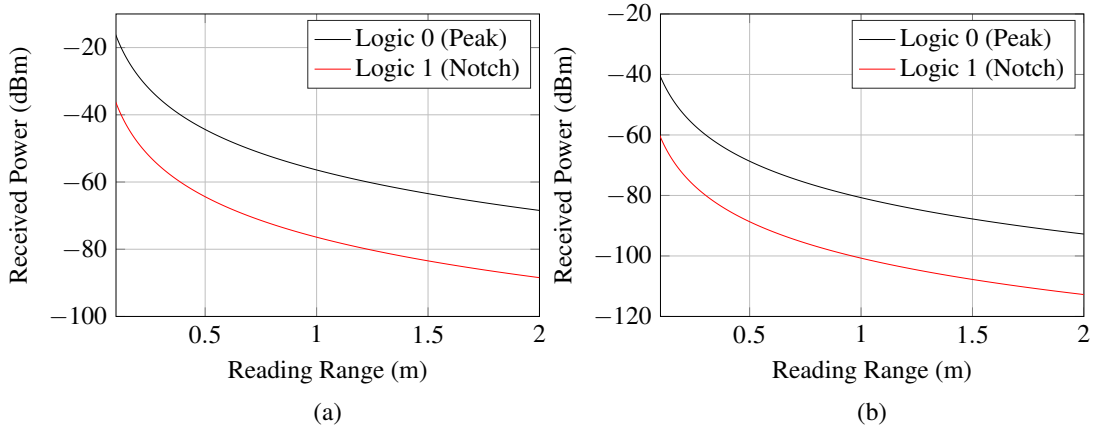

Figure 4.1: Theoretical reading range as a function of the received power at 5 GHz in case of: (a) Frequency sweeping interrogation with 0 dBm/50 MHz. (b) UWB transmission with −41.3 dBm/MHz.

where D is the largest tag dimension as shown in Fig. 4.2. It is found that the minimum separation between the tags to less affect each other is 6 cm. Thus, various tags are added in the simulation environment with 6 cm separation. If the tags are with the same code, the RCS level is directly related to the tags quantity. However, if the tags are different codes as explained in Fig. 4.3, the notches are interleaved with each other producing a large notch at the whole band. Hence, the notches are not deterministic at which frequencies. One possible solution to minimize this interference is to make the notch bandwidth very narrow, and sharp seems to be ideal. However, this can't be even attained. Therefore, decreasing the number of tags in the reader interrogation zone is utmost important.

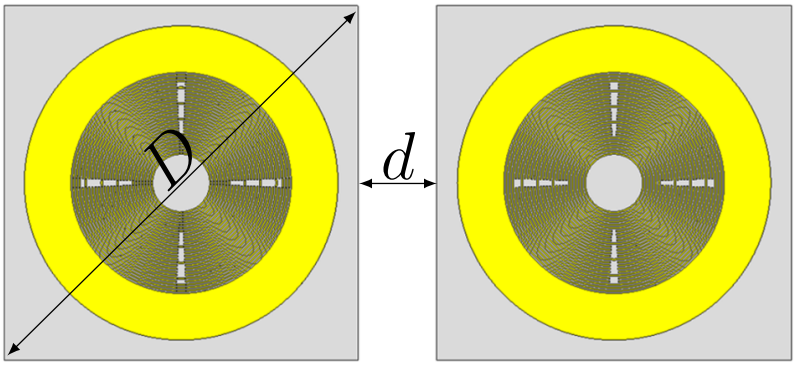

Figure 4.2: Multi-tag interference simulation setup.

In order to overcome the above-mentioned limitations, the other reading range parameters are enhanced to increase the reader coverage and minimize the multi-tag interference problem.

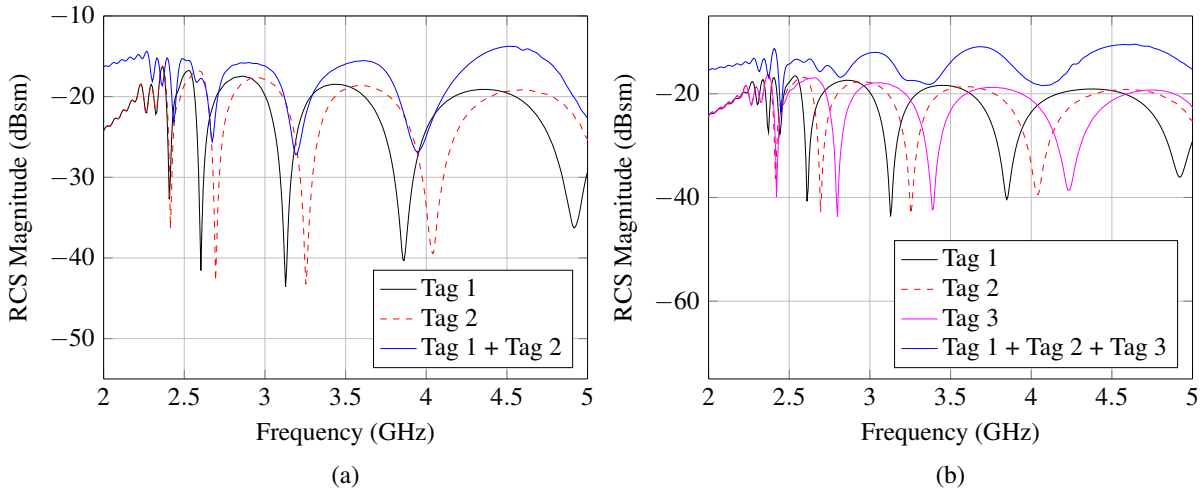

Figure 4.3: Multi-tag interference simulation study for: (a) Two tags with different codes. (b) Three tags with different codes.

Therefore, a high gain, directive antenna is proposed to be utilized in the reader side. Moreover, this antenna should provide UWB operation to codify an appropriate number of bits. However, the conventional antenna arrays can not provide uniform functionality over a wide range of frequencies due to the complex feeding networks [10]. Therefore, the spatial feeding RA antenna is the best candidate in comparison to the bulky reflector and the complex feeding network phased array antennas. However, there are two challenges that impede the RA antenna employment. The first challenge is the narrow-band operation [47]. The second challenge is the capability of providing continuous beam scanning while covering a wide band frequency, satisfying the FC chipless RFID system requirements. These handicaps are addressed in the following sections.

4.2 Reflectarray Fundamentals and Limitations

RA is a hybrid antenna system that combines desirable features of the parabolic reflector and the phased array antennas. These combined advantages are the spatial feeding, the light weight, the easy integration with RF circuitry, the wide beam scanning ability, the comfortability with installation platforms (conformal geometry), the multi-beam capability and the low cost. The building blocks of the RA antenna as described in Fig. 4.4 consist of free space located feeder that spatially illuminates a flat reflecting surface of radiating cells. The power received by each cell is re-radiated after modulating the reflection phase. Thus, the RA antenna is a phase only synthesis problem, where the feeder pattern constrains the amplitude degree of freedom. Therefore, the re-radiation characteristics are controlled by tuning the reflection phase distribution over the array

surface. Therefore, the reflecting surface can be engineered to re-radiate the electromagnetic energy in a single beam or multi-beams with a prescribed shape and direction.

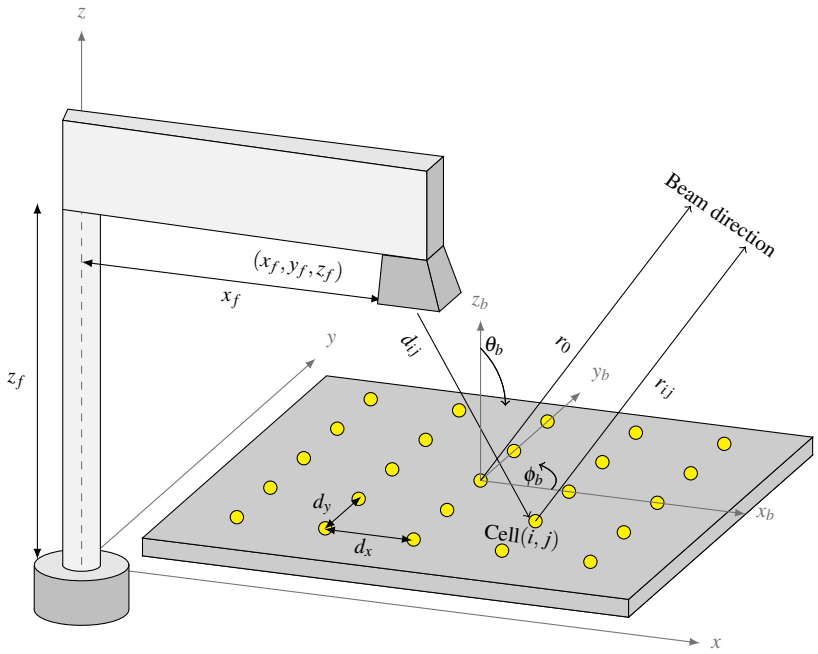

Figure 4.4: RA building blocks.

The first RA antenna limitation is the narrow-band operation [48], which results from the dependency of the compensated spatial distance on the frequency. Moreover, the RA constituent cell exhibits narrow-band resonance. Basically, using single resonator as the array element offers one resonant frequency. Consequently, the phase range is less than 360°, the phase slope is nonlinear and thus the operating bandwidth is narrow with high scattering field components. Recently, several efforts are devoted to increase the RA antenna bandwidth such as utilizing multi-layer stacked resonators and exploiting the aperture coupling techniques. [48]. Thus, these proposed solutions are labor intensive manufacturing process. Recently, utilizing the single layer concentric or non-concentric resonators can enhance the RA antenna bandwidth [49], [43], [50]. However, these designs are backed with a low permittivity substrate to linearize the reflection coefficient phase slope. This added substrate has to be assembled without air gaps. In this regard, a foam substrate is exploited to linearize the phase slope as will be explained in the following sections.

The second aspect introduced in this chapter is to steer the RA antenna beam. There are various enabling technologies for the dynamic control of the RA antenna beam. These technologies differ significantly in terms of; availability, performance, complexity, suitability

for a given frequency range, integration and biasing. Therefore, it is crucial to select the best technology for a given implementation and a set of requirements.

The beam of the RA antenna can be steered either mechanically or electronically. The mechanical scanning approaches suffer from low scan rate, high scan volume, low scan resolution and high-cost [51]. On the other hand, the electronic scanning methods utilize variable lumped elements that are embedded in the array cells and controlled via analog biasing lines. Therefore, steering the beam electronically is faster (no moving parts), more robust, and reliable. Most designs so far use lumped elements such as P-I-N and varactor diodes. Thus, the objective is to steer the beam utilizing the electronically controlled tuning devices. These elements can be aperture coupled or directly connected to the RA cell. Although the aperture coupling configuration provides wide bandwidth because of the independent optimization to the tuning device, it suffers from design complexity. Furthermore, the use of two different substrates increases the cost and losses [52]. Therefore, the aperture coupling is not preferred. Research in [53] places two tuning devices across a slot in the central part of the radiating patch. However, the added metallization and vias create undesired scattered field components which degrade the antenna performance and increase the SLL. Other research is introduced in [54], where the tuning device is connected between the radiating surface and the ground plane. Thus, this configuration requires a through hole via to place the diode through the substrate and to connect the radiating patch with the ground plane. But this solution is impractical, in addition to the limited bandwidth that doesn't exceed Fractional Bandwidth (FBW) of 0.6%. Therefore, these design limitations of the beam steering RA antenna can be counteracted if there is a possibility to reduce the number of the tuning devices, surface mounts these devices and minimize the patch metalization.

In the following sections, the handicaps mentioned above are addressed and solved. Therefore, the UWB fixed and adaptive beam RA antennas are introduced. Moreover, different feeder and beam configurations that emulate various real world scenarios are presented. Section 4.3 illustrates the RA design and analysis methods. The POC RA antenna is elucidated in Section 4.4. The introduced UWB fixed beam RA is demonstrated in Section 4.5. Finally, the electronic beam steering RA is introduced in Section 4.6. followed by chapter conclusion.

4.3 Design Guidelines and Analysis Methods

There are two approaches that can be employed in the design of the RA antenna. The core functionality of these approaches is to calculate the cell reflection phase curve with the physical or electronic tuning parameters. The first approach is based on calculating the field distribution at the array plane while illuminating the RA surface with a determined feeder radiation pattern. Then, the phase distribution on the RA plate can be compensated and the beam can be controlled. The other approach is based on the assumption of normal plane wave excitation and local periodicity, where all the RA cells are identical. This approach takes into account the coupling between the array cells and the specular reflection from the ground plane. However, there are phasing error terms due to the non-identical cells or in other words the non-uniform current distribution. Besides, the incidence plane wave is oblique and the fact that the feeder emits spherical waves. These phase error terms can be calculated and minimized. Therefore, the Wave Guide (WG) model is developed based on the approach mentioned above and hence employed in the designed RA antennas. Consequently, the boundary conditions of the WG model verify the infinite array approach as illustrated in Fig. 4.5. Hence, the cell reflection amplitudes and phases are calculated with the tuning parameter values, while considering the normally incident plane wave on the RA cell.

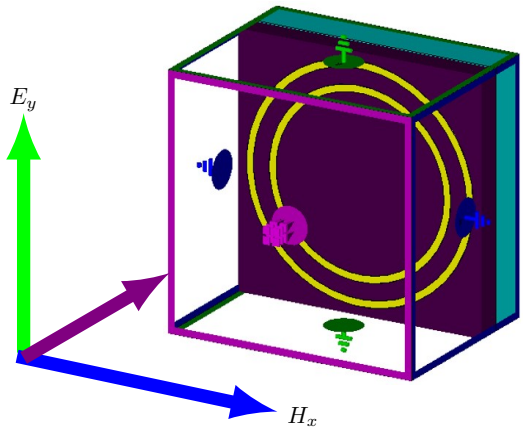

Figure 4.5: CST developed wave guide model boundary conditions.

4.3.1 Design Guidelines

The RA cell is the basic building block, which is determined first. The cell parameters are the substrate materials, the cell shape, the cell dimensions and orientations. Hence, these parameters

are exploited for minimizing the backscattering losses and linearizing the reflection phase slope. After obtaining the best cell specifications, the tuning parameters which can be physically or electronically controlled are determined. Afterward, the reflection phase coefficient is calculated in accordance with the variation of the tuning parameters and utilizing the developed WG model. Hence, the compensating phase curves are derived at the design frequencies. Consequently, the developed Matlab algorithm calculates the required compensating phase distribution on the array surface. These calculations take into account the other array configuration parameters which are (the No.of cells, the No.of beams, the direction of the generated beams and the feeder configuration). After that, the calculated phase distribution is realized exploiting the tuning parameters set. Therefore, each cell is realizing a predetermined reflection phase values and thus the array is constituted from these cells. Finally, the feeder is designed and the complete array is assembled, simulated, optimized and analyzed for performance prediction. The initial phase distribution for each cell is calculated based on (4.3).

$$\phi_R(x_{ij}, y_{ij}) = k_0(d_{ij} - (x_{ij}\sin\theta_b\cos\phi_b) - (y_{ij}\sin\theta_b\sin\phi_b)) \tag{4.3}$$

Where $\phi_R(x_{ij}, y_{ij})$ is the phase of the reflected field, k_0 is the propagation constant in vacuum, d_{ij} is the distance from the feeder phase center to the array cells, (x_{ij}, y_{ij}) are the coordinates of element (i, j) and (θ_b, ϕ_b) are the elevation and azimuth angles of the produced beam respectively. Lastly, the minimum distance between the RA cells that avoid the appearance of grating lobes is calculated based on (4.4).

$$\frac{d}{\lambda_0} \leqslant \frac{1}{1+\sin(\theta)} \tag{4.4}$$

Where d is the element spacing, θ is the angle of the feeder incident beam. Therefore, the elements located at the RA edges are better to be larger spacing. However, the uniform spacing is easier in design and manufacturing.

4.3.2 Analysis Methods

The factors that gauge the RA antenna performance are the aperture efficiency, the phase errors, the cross polarization level, the losses, and the feeder blockage [48]. The mathematical expressions of these terms are expressed for the analytical analysis of the RA antenna performance. The first factor is the aperture efficiency, which is expressed in (4.5) [55]:

$$\eta_{aper} \approx \eta_s \eta_t \tag{4.5}$$

Where η_{aper} is the aperture efficiency, η_s is the spillover efficiency, and η_t is the taper efficiency. Considering that the feeder pattern is $\cos^n(\theta)$, the spillover efficiency is calculated based on (4.6) [48]:

$$\eta_s = 1 - \cos^{n+1}(\psi_{RA}/2) \tag{4.6}$$

Where (ψ_{RA}) is the subtended angle of the RA. In a similar way the taper efficiency is driven in [48]:

$$\eta_t = \frac{2n\,(1-\cos^n(\psi_{RA}/2))^2}{\tan^2(\psi_{RA}/2)\left[\frac{n}{2}-1\right]^2 1-\cos^n(\psi_{RA}/2)} \tag{4.7}$$

Therefore, a judicious design of the RA surface yields a good aperture efficiency and the best F/D ratio is determined from the optimum subtended angle.

The polarization efficiency of the RA is expected to be high even if the feeder is low cross-polarization level. This is because the RA constituent elements are polarization selective dissimilar to the parabolic reflector. The phase efficiency is determined from the phase error terms mentioned before. These error terms get worse for large RA aperture size except the terms of local periodicity assumption. Consequently, the bandwidth is reduced. The maximum value effect of phase errors is 180°, which causes out of phase radiation. Therefore, these RA antenna analysis terms are estimated numerically as mentioned using array theory and verified with the full wave simulation.

4.4 The Developed Fixed Beam Reflectarray Antennas

Regarding to the fixed beam RA antennas, the printed elements located on the array surface impart a given phase onto the incoming wave physically. The physical parameters can be the element dimensions, position or orientation. Therefore, a judicious design for the physical parameters of the RA constituent elements leads to a unique aperture field distribution for each of its operating bands and polarization. In this section, the wideband RA antenna operating at 5.8 GHz is presented. Afterward, the UWB RA antenna which is dedicated to the chipless RFID applications is introduced.

4.4.1 Cell Features and Design Key Points

For an ideal RA cell, it is supposed that the magnitude of the re-radiated wave is the same as that of the incident wave. Therefore, the conductor and dielectric losses of the cell should be

kept minimum. The other design key point is the reflection phase curve. The ideal phase curve is assumed to be linear and sufficient to avoid approximation and truncation errors. Hence, the ring structures are considered to be the best candidate. Although the ring structures are narrow-band elements, the resonance bandwidth can be increased by increasing the substrate thickness and reducing the effective permittivity. However, increasing the substrate thickness is too expensive and lossy. Therefore, a low permittivity substrate which is (Ro5880 $\varepsilon_r = 2.2$) is loaded with a foam layer to enlarge the resonance bandwidth and minimize the re-radiation losses as illustrated in Fig. 4.6. Furthermore, this foam layer is exploited to linearize the phase slope as clarified in Fig. 4.7.

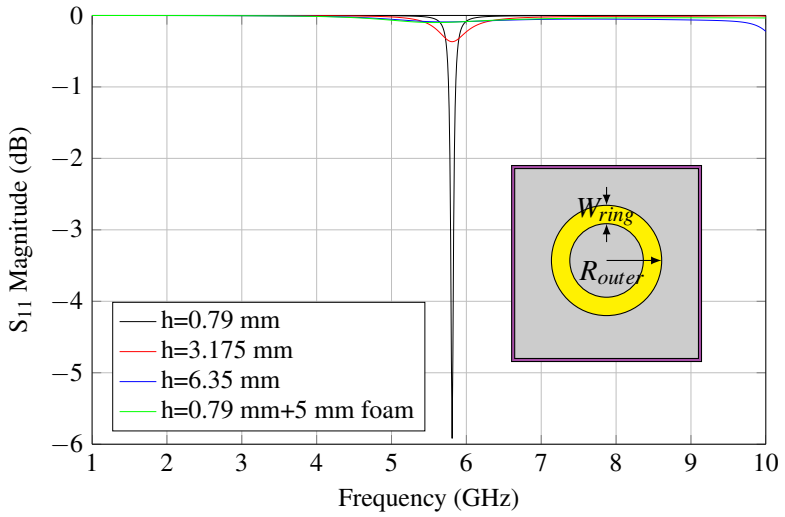

Figure 4.6: Re-radiation losses comparison for different substrate thickness.

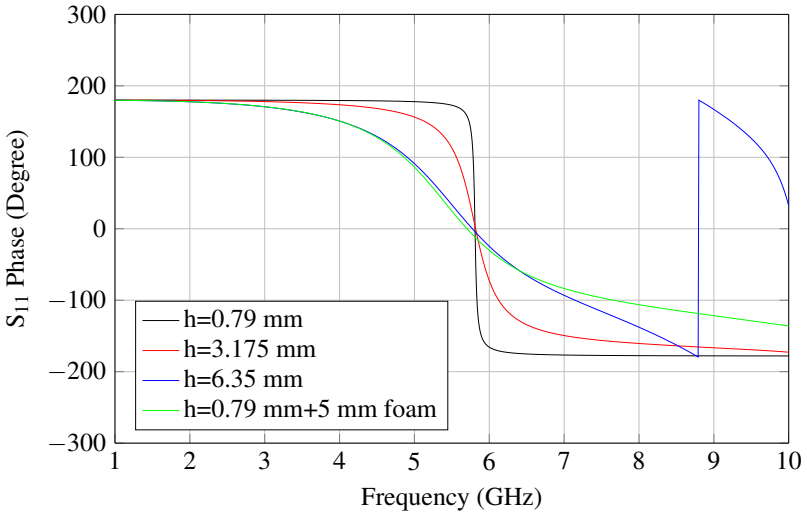

Figure 4.7: Reflection phase comparison for different substrate thickness.

4.4.2 5.8 GHz Reflectarray Antenna

In this subsection, a wideband RA antenna operating at 5.8 GHz is presented. The cell design evolutions are discussed first. After that, the design guidelines introduced in the former section are applied and the complete RA antenna is constructed for simulation and measurements.

It is important that the cell reflection phase curve provides all the necessary phase values. However, as obvious from Fig. 4.7 that the reflection phase of one ring can not attain 360 degree phase range. So, a second ring is incorporated to extend the phase range. Therefore, the basic cell geometry as described in Fig. 4.8 consists of two closely spaced ring resonators over a grounded dielectric substrate. The reflection phase range of these two rings is sufficient, but the phase slope is not smoothly continuous. The reason is that the two resonances are not close enough to be considered as one resonance with continuous phase curves. The gap between these two resonances is reduced with the increase of the substrate thickness as explained in Fig.4.9. However, the thicker substrates are too expensive and thus an appropriate thin substrate is loaded with a suitable foam layer to implement the desired curve smoothness. Therefore, the Ro5880 thin substrate (h = 0.79 mm) is supported by 5 mm foam material and utilized for the array design. Moreover, the cell parameters are optimized for smoothing the reflected phase curve and minimizing the backscattered losses.

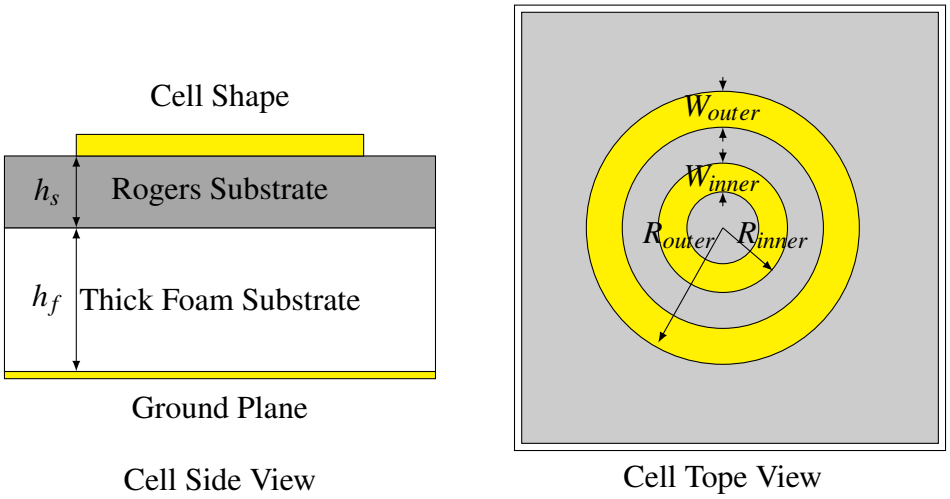

Figure 4.8: The basic cell configuration of the fixed beam RA antennas.

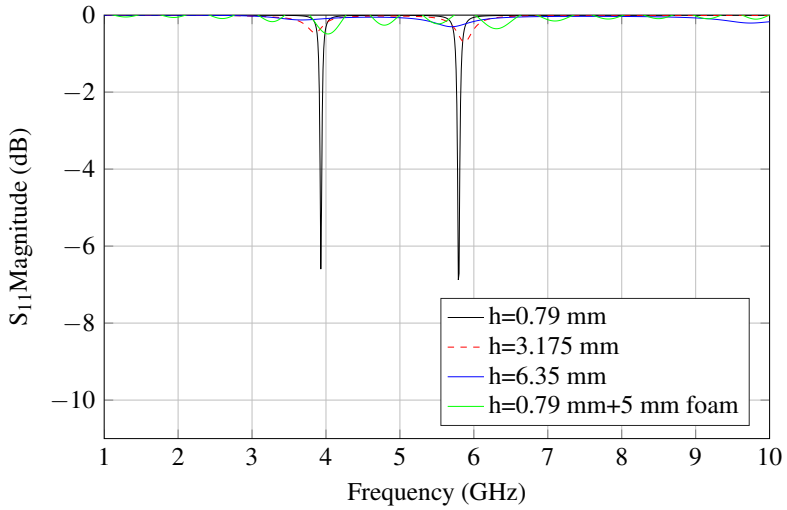

Figure 4.9: Re-radiation loss comparison for the double ring resonator cell with different substrate thickness.

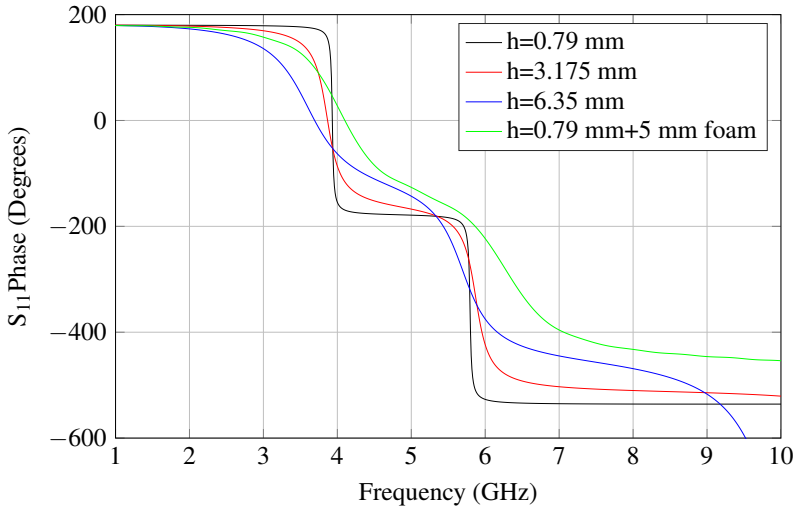

Figure 4.10: Reflection phase comparison for the double ring resonator cell with different substrate thickness.

Following the design guidelines, the cell dimensions are first determined. The cell size is $\lambda/2 \times \lambda/2$, and the best rings diameter and width ratios, which provide the sufficient phase range and the linear phase slope are illustrated in Fig. 4.11. After that, the reflected phase response versus the cell physical parameters is calculated exploiting the developed Computer Simulation Technology (CST) WG model as illustrated in Fig. 4.11a. Then, the optimized phase distribution of the array is calculated based on the desired feeder setup and the required beam configurations. These compensating phase values are acquired from the relative variation of rings radius's and width's of the array cells as illustrated in Fig.4.11b.

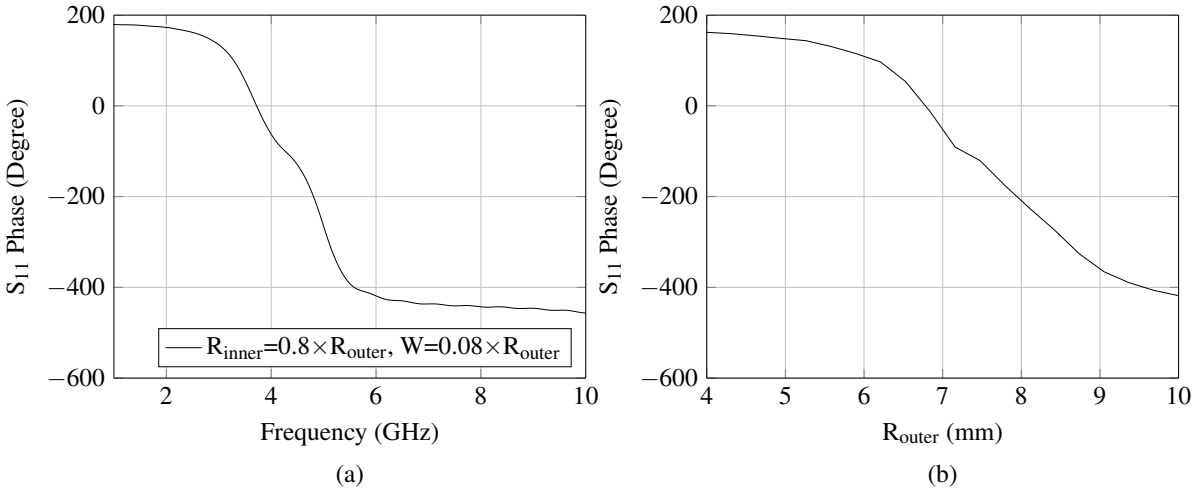

Figure 4.11: 5.8 GHz RA antenna cell: (a) The best relative dimensions ratios. (b) The resultant reflection phase curve with the physical dimensions at 5.8 GHz.

The RA surface which constitutes of 5×9 cells is implemented and the feeder is designed. Hence, an UWB LPDA antenna covering the frequency band from 1 to 6 GHz is designed and employed to feed the RA surface. For the reason of that, the LPDA is not a standard feeder; the RA bandwidth is about 300 MHz centered at 5.8 GHz. The RA and the feeder are implemented, simulated and optimized with CST. The simulation setup as shown in Fig. 4.12a describes the feeder and the RA surface configuration.

The measurements are conducted inside the AC as described in Fig 4.12. First, the feeder radiation pattern is measured and hence the complete RA antenna. Thus, the simulated and measured feeder patterns are first compared as illustrated in Fig. 4.13. This comparison declares that the simulated feeder pattern is not exactly the same as the measured one in terms of gain, beamwidth, SLL and so on. However, another comparison is conducted between the simulated/measured feeder radiation pattern and the simulated/measured RA antenna patterns at 5.8 GHz. This comparison as shown in Fig. 4.13 illustrates that the simulated/measured ratios between the RA antenna and the feeder gain and beamwidth are likely the same. It is clearly noticed that the RA antenna SLL is about -10 dB, 4 narrower beam-width and thus 6 dB higher gain than the feeder in both simulations and measurements. These acquired results proof the RA antenna concept and validate the design approach.

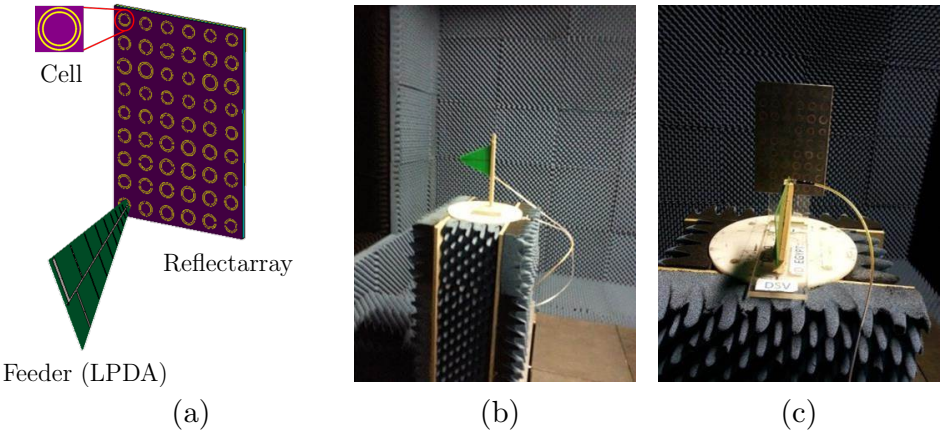

Figure 4.12: 5.8 GHz RA simulation and measurement setup: (a) CST simulation setup. (b) Feeder measurement setup. (c) Complete RA antenna measurement setup.

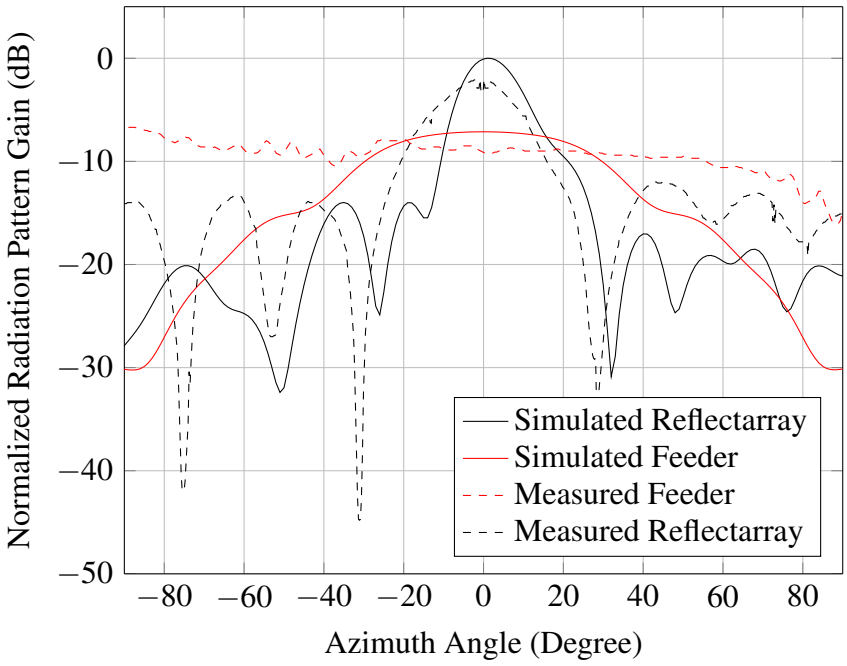

Figure 4.13: Simulation and measurement results for the 5.8 GHz GHz RA antenna in comparison to the associated feeder.

4.5 UWB Reflectarray Antenna for Chipless RFID Applications

This section introduces the UWB RA antenna which is developed to be utilized in the chipless RFID reader. Therefore, the RA design objectives are to produce a high gain pencil beam pattern over UWB range of frequencies. Moreover, the design complexity and the cost features are important to be minimized.

As mentioned before, the RA cell should provide a sufficient phase range and linear phase slope if a good bandwidth is to be achieved. Furthermore, the feeder phase center position should be kept constant. Thus, the phase Figure of Merit (FoM) is defined to determine the slope of the phase curve around a certain frequency. This term is optimized for a minimum value for each phase curve in order to have a good bandwidth performance.

$$FoM = \frac{\Delta\phi}{\Delta f} \tag{4.8}$$

The utilized cell as explained previously consists of two circular rings in a nested formation. This developed cell introduces two co-located resonances and therefore essentially doubles the phase range of a single resonance element. A thick substrate with $h = 3\,\text{mm}$, $\varepsilon_r = 2.3$ is then utilized to improve the RA bandwidth. Furthermore, a foam loading substrate is exploited to reduce the effective dielectric constant and so the cell quality factor. Thus, the resonance bandwidth and the phase slope are allowed to be smoothly varied. Hence, the slow phase variation as shown in Fig. 4.14 provides immunity against manufacturing tolerance and truncation errors. Moreover, the Focal/Diagonal (F/D) ratio is optimized so that the array elements in the middle are almost same size and smaller than the edge elements to reduce the coupling. This smooth variation of the cell elements across the RA surface justifies the assumption of infinite periodic and minimize the phase errors. Furthermore the phase **FOM!** (**FOM!**) is optimized for a minimum value. Thus, the UWB operation of the RA antenna is attained.

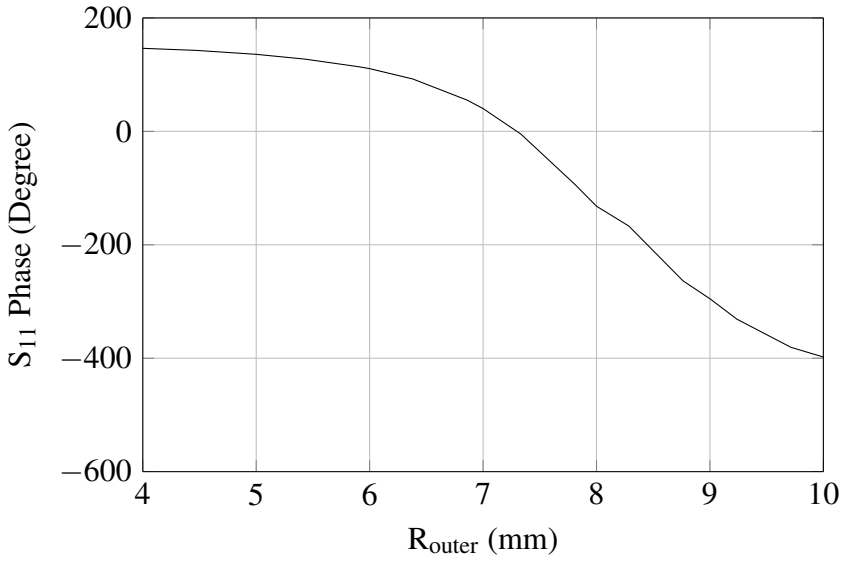

Figure 4.14: UWB RA cell reflection phase with the outer ring radius at 5 GHz and the other cell dimensions are in relation to R_{outer}.

An UWB horn antenna operating from 4 GHz to 6 GHz is designed, implemented in CST to be employed as the array feeder. Furthermore, different feeder and array configurations are investigated to best emulate the real case scenarios with the appropriate configuration. Therefore, the possible configurations can be Center Feed Center Beam (CFCB), Offset Feed Center Beam (OFCB), Center Feed Offset Beam (CFOB) and the simultaneous multi-beam. The CFCB configuration is not preferred because of the feeder blockage and to minimize this blockage the feeder or the beam is placed or directed away from the center of the RA surface as shown in Fig. 4.15. Thus, both CFOB and OFCB configurations are demonstrated. The CFOB configuration is defined by a single beam that is directed towards $\phi = 0^o,\ \theta = 30^o$, while the OFCB beam is directed towards $\phi = 0^o,\ \theta = 0^o$ and the feeder is placed away from the RA center as shown in Fig. 4.16. The simulated realized gain for the CFOB and OFCB is illustrated in Fig. 4.16, where the results verify that both configurations are accepted for feeder blockage minimization.

The last investigated configuration is the multiple beam generation. Hence, the RA feeder is placed at the center of the array surface and simultaneous multi-beam in different directions can be generated. This configuration is described in Fig. 4.17, where double beams can be achieved covering two different interrogation zones simultaneously. However, depending on the number of generated beams, the RA gain, HPBW are reduced. Therefore, the OFCB configuration is employed for the introduced UWB RA antenna. This OFCB UWB RA antenna is developed specifically for the chipless RFID applications.

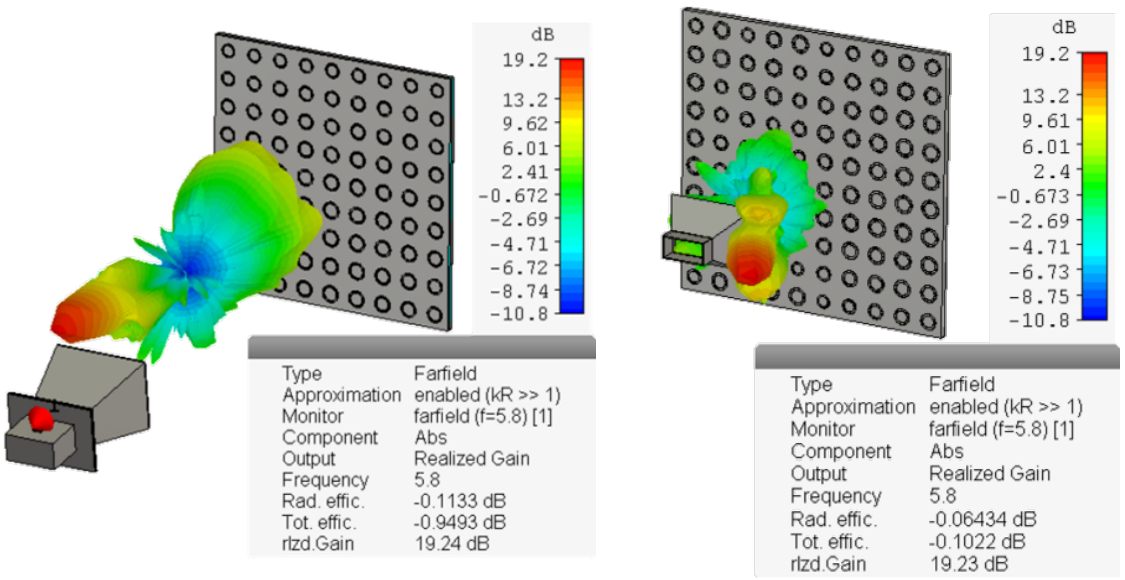

Figure 4.15: RA blockage reduction configurations, OFCB on left and CFOB on right.

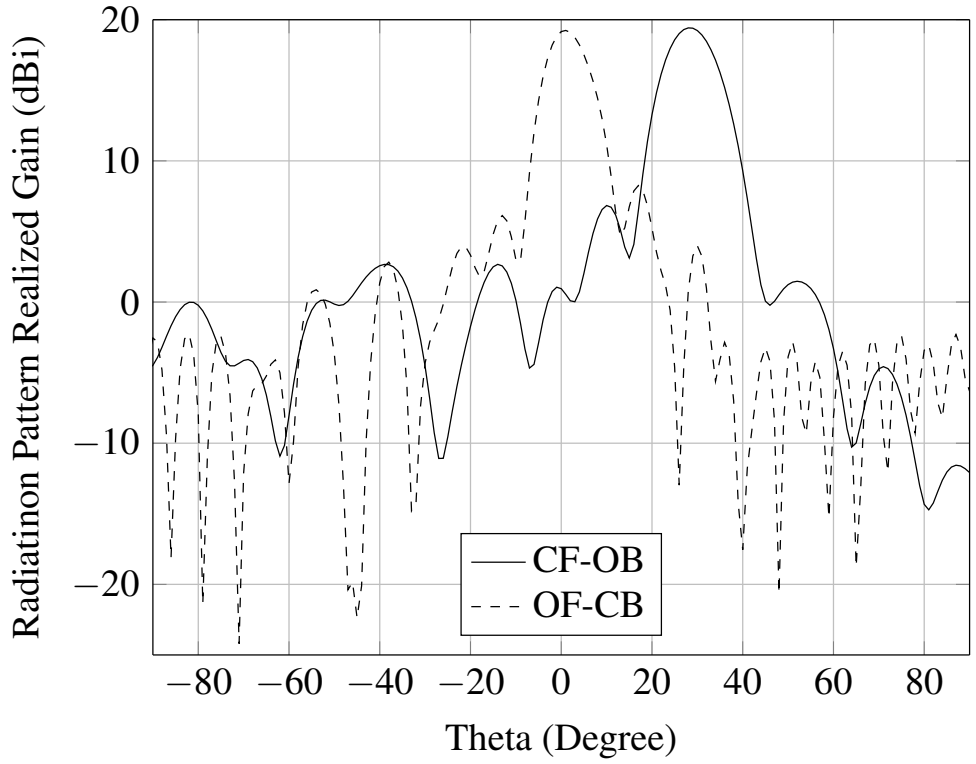

Figure 4.16: Realized radiation pattern gain for the CFOB and OFCB configurations at 5 GHz.

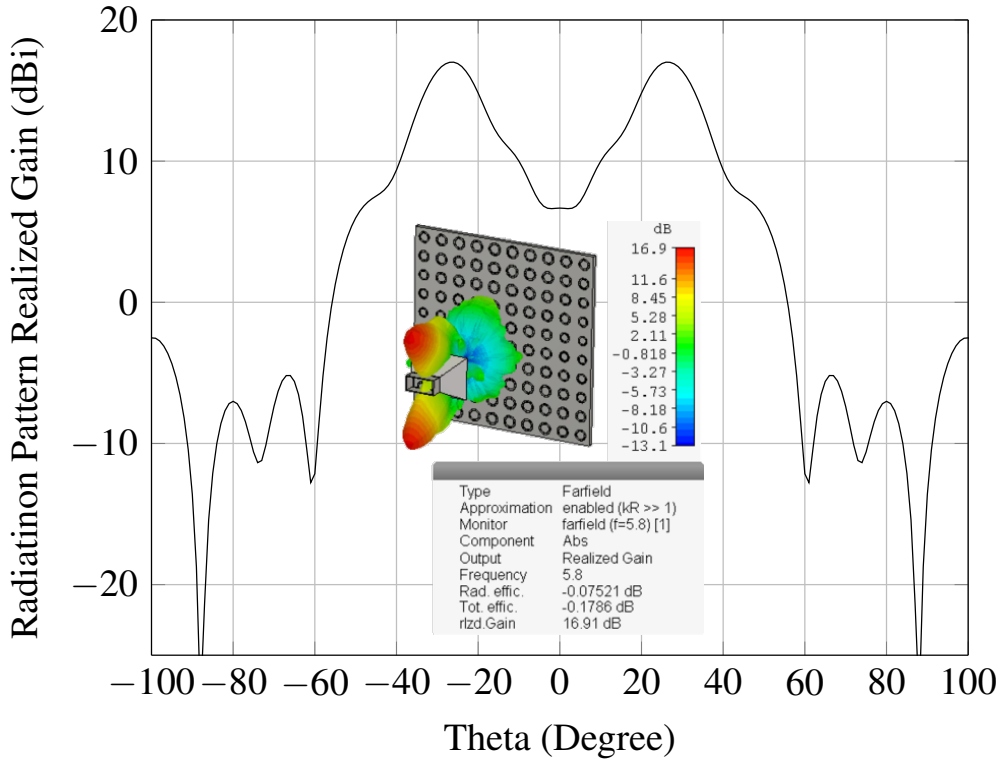

Figure 4.17: Simultaneous multi beam configuration with dual beams directed at $\phi = 90^o, \theta = 30^o$ and $\phi = 90^o, \theta = -30^o$.

4.5.1 UWB RA Antenna Measurements

First, the feeder which is horn antenna operates from 4 GHz to 6 GHz is designed, simulated and manufactured. Hence, the manufactured horn operation is verified inside the AC, where the measurement setup of the feeder is described in Fig. 4.18a. The simulated and measured radiation patterns are in a good agreement as illustrated in Fig 4.19a. After that, the RA surface which consists of 9×9 elements is implemented. Lastly, the feeder is integrated with the RA surface as shown in Fig.4.18b and the complete RA antenna is verified inside the AC. The RA antenna simulations and measurements are in a good match as illustrated in Fig. 4.19b. However, the RA beam is slightly shifted right beyond 5.5 GHz this shift results from the phase errors of realistic integration.

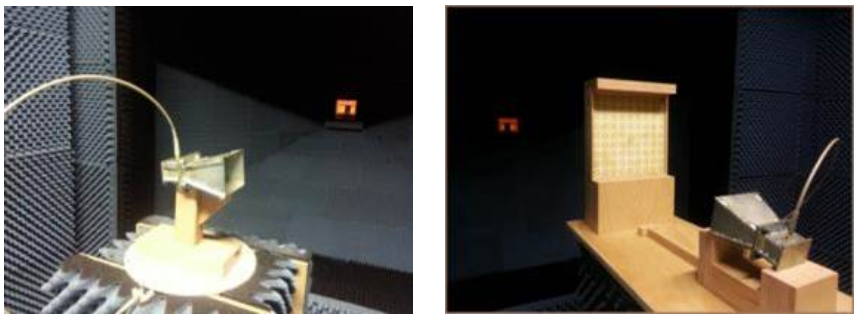

(a) (b)

Figure 4.18: UWB RA antenna OFCB measurements setup: (a) Feeder measurement setup. (b) Complete RA antenna measurement setup inside AC.

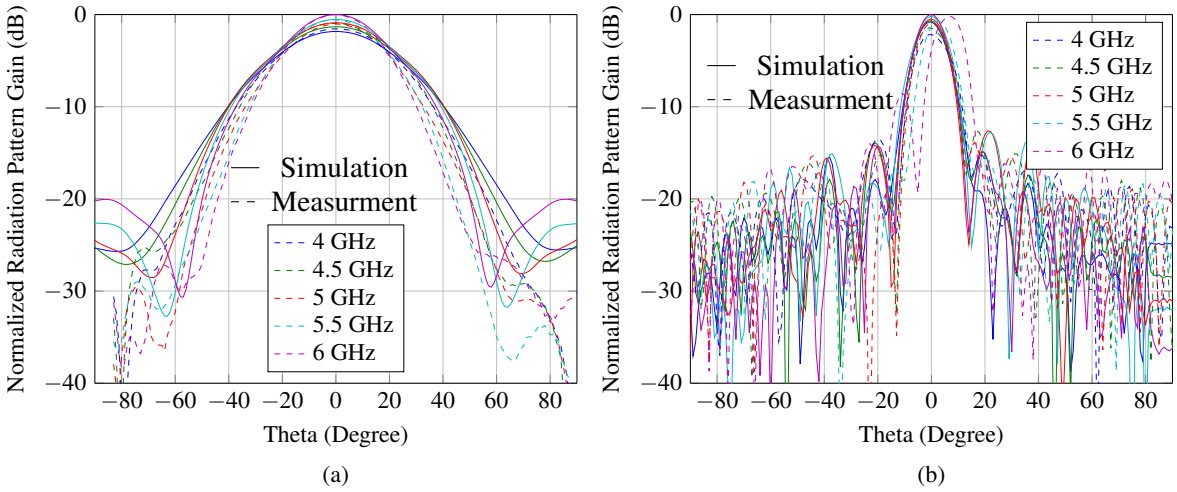

Figure 4.19: UWB RA antenna simulated and measured radiation patterns: (a) Feeder radiation patterns. (b) Complete UWB RA antenna radiation patterns.

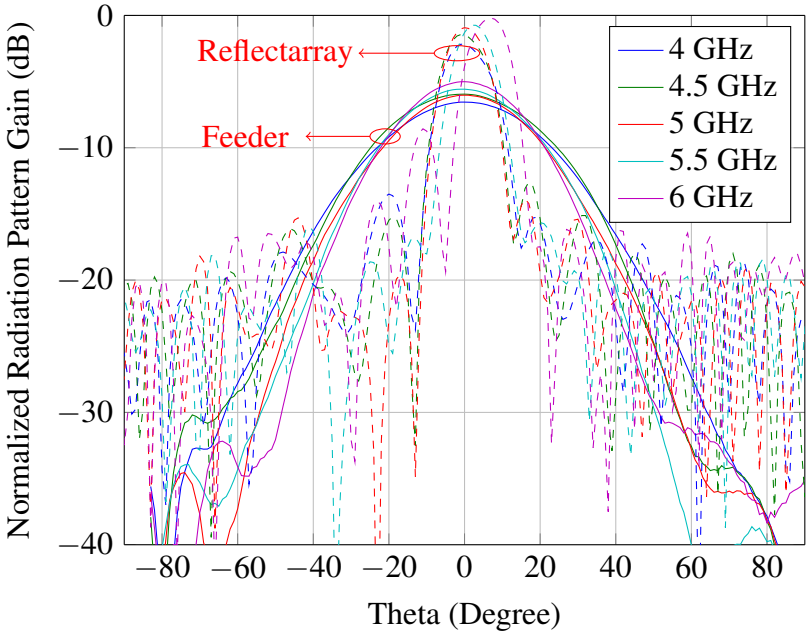

Figure 4.20: The measured radiation patterns of the UWB feeder vs the UWB RA antenna.

4.5.2 Realistic Testbed: Physically Modulated Tags and UWB RA antenna

The proposed system is a preliminary design for the supermarket scenario, where the tagged items are moving on a conveyor belt through the interrogation zone of a fixed reader antenna system. Therefore, two different NPM tags are designed in the frequency range from 4 GHz to 6 GHz. After that, the complete RA antenna is integrated with the USRP to assess the objectives of the design with realistic chipless RFID tags in a real environment. The complete testbed is illustrated in Fig.4.21, where the tags are placed in the middle distance between the transmitting and receiving RA antennas. The simulated and measured tag responses are clarified in Fig. 4.22, where the achieved reading range is about 100 cm. These results verify the system level integration of the physically modulated tags and RA reader antennas.

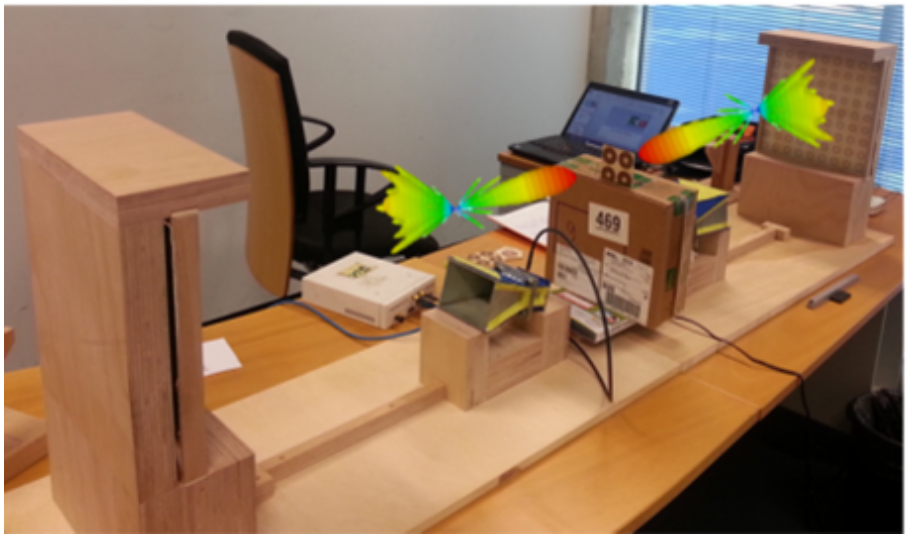

Figure 4.21: Physically modulated tags and UWB RA antenna testbed.

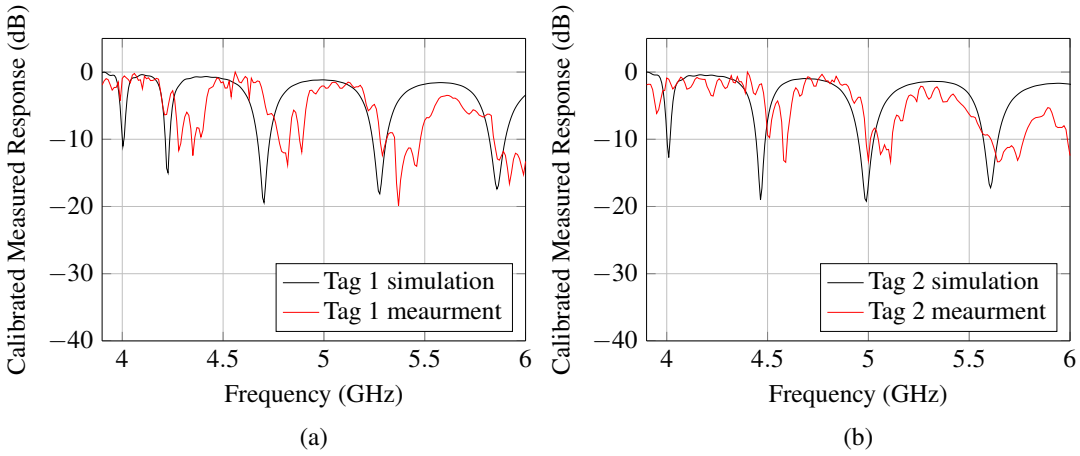

Figure 4.22: Physically modulated tags and UWB RA antenna testbed results: (a) Simulation and measurement results for the first tag with code (11010101). (b) Simulation and measurement results for the second tag with (10101010) code.

4.5.3 UWB Dual Polarized Reflectarray Antenna for the Depolarized Chipless RFID Tags with Low Cross Polarization Level

The low cross-polarization level is essential in order to be able to detect the depolarized tags introduced in the preceding chapter. Therefore, UWB orthogonal beams RA antenna is developed to be utilized with the depolarizing tags. The double ring structure can be employed as the array cell by cutting gaps across the rings in the cross polarized direction. Thus, the cross polarization

patterns are canceled. However, a polarization selective dipole is preferred to increase the isolation level between the co-polarized and cross-polarized re-radiated fields.

The basic cell is described in Fig.4.23a, where the 360° phase response is acquired using two closed resonant dipoles. Hence, the orthogonal polarization is produced by using these two dipoles in a vertical arrangement for the co-polarization beam and a horizontal arrangement for the cross-polarization beam. Therefore, the best cell dimensions and substrate parameters for one polarization are first calculated and optimized for bandwidth enlargement. After that, these lengths are calculated to produce the dual polarized beams in two different directions to minimize the cross-polarization levels.

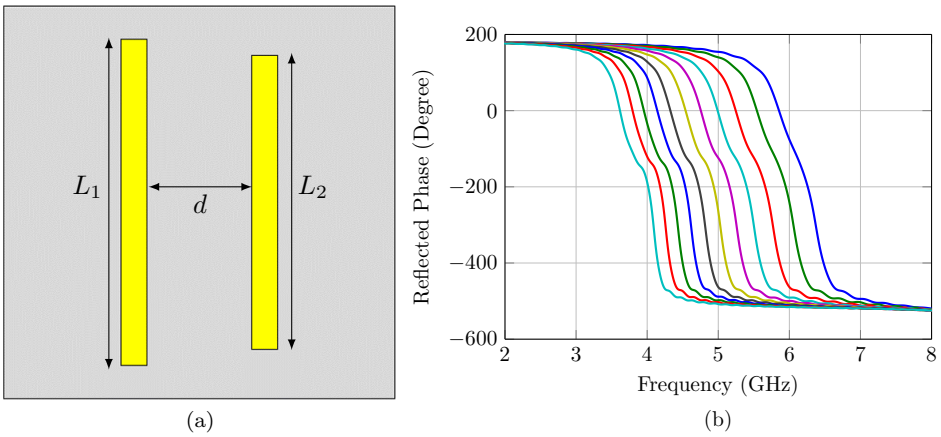

Figure 4.23: UWB RA dual polarized cell: (a) Cell shape consists of two coupled dipoles with relative lengths $L_2 = 0.9 \times L_1$. (b) Reflected phase with frequency at different lengths of the first dipole.

The dual polarized RA antenna configuration is described in Fig.4.24, where two spatially separated orthogonal feeders are utilized to feed the RA surface and in accordance different beam in each polarization is produced. Thus, the cross polarization levels are further reduced. The relative dipole lengths are calculated to produce an offset beam directed at $(\theta_b = 30°,\ \phi_b = 0°)$ for the vertical polarization and the other horizontally polarized beam is directed at $(\theta_b = -30°,\ \phi_b = 0°)$. The simulation results are presented in Fig.4.25, where the cross-polarized patterns are defined based on Ludwig's third definition [56]. These results indicate that the cross-polarization level is less than 40 dB, the SLL is less than -10 dB; the RA antenna gain is about 20 dB which is 4 times higher than the feeder. Furthermore, the bandwidth of operation is about 1 GHz for both polarizations. The asymmetric in horizontal and vertical polarization patterns is produced because of feeder and cells asymmetry.

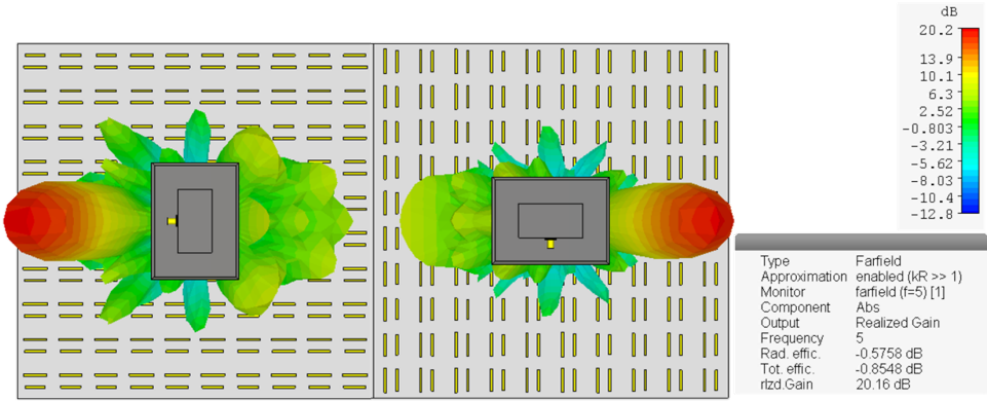

Figure 4.24: UWB RA dual polarized cell: (a) Cell shape consists of two coupled dipoles with relative lengths $L_2 = 0.9 \times L_1$. (b) Reflected phase with frequency at different lengths of the first dipole.

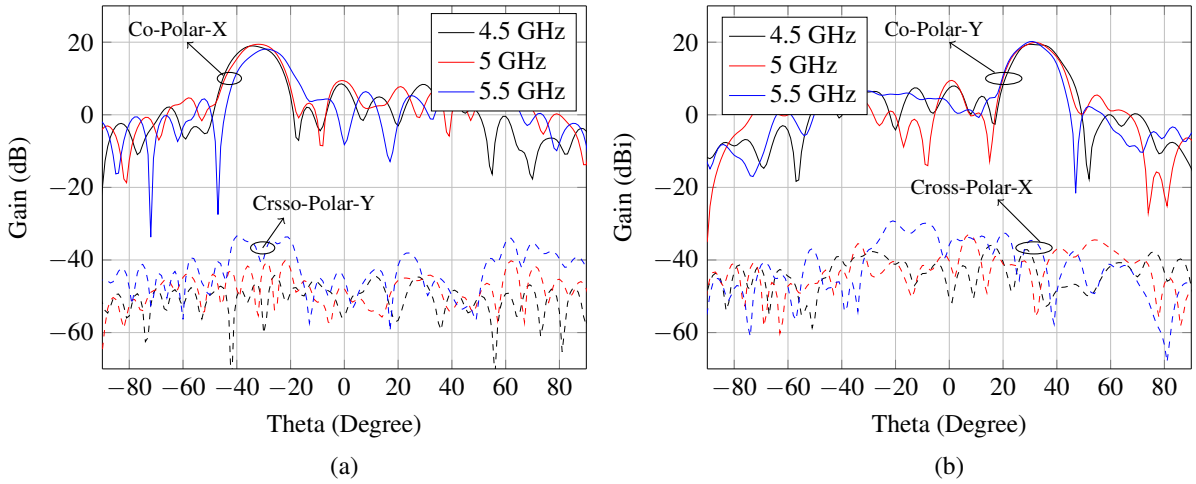

Figure 4.25: The dual polarized RA simulated radiation patterns illustrating the UWB operation: (a) Horizontal polarization. (b) Vertical polarization.

4.6 Adaptive Electronically Beam Steering RA Antenna

The previously fixed beam RA antennas are characterized by a unique and specific radiation pattern which can fit some chipless RFID applications. Although it is easy to install with no electronic circuits required, it can not provide accurate tag localization. Furthermore, it picks up multi-path signals alongside with the tag signal in case of tag misalignment. However, the electronic beam steering prototype with dynamic beam pattern can overcome these problems. Moreover, exploiting the spatial diversity among tags locations, the number of tags in the interrogation zone can be reduced smartly. Thus, the reading errors resulted from the collisions among

tags are reduced spatially. In this section, a novel beam scanning RA antenna is implemented for acquiring these unique features in the chipless RFID readers. The electronic components, wide scanning angles are implanted with the novel cell criteria. The following subsection provides some explanation and simulation results related to the cell and the RA design evolutions.

4.6.1 Cell Design

A novel convenient cell is developed for the beam steering RA antenna. This cell enables control on its resonance position electronically utilizing a single varactor diode, which is integrated on top for simple manufacturing and biasing as described in Fig.4.26. Therefore, the varactor capacitance values are employed to change the re-radiated phase by modifying the electrical length of the dipole. So, the phase of the single element is dynamically governed by using only a voltage control to the varactor.

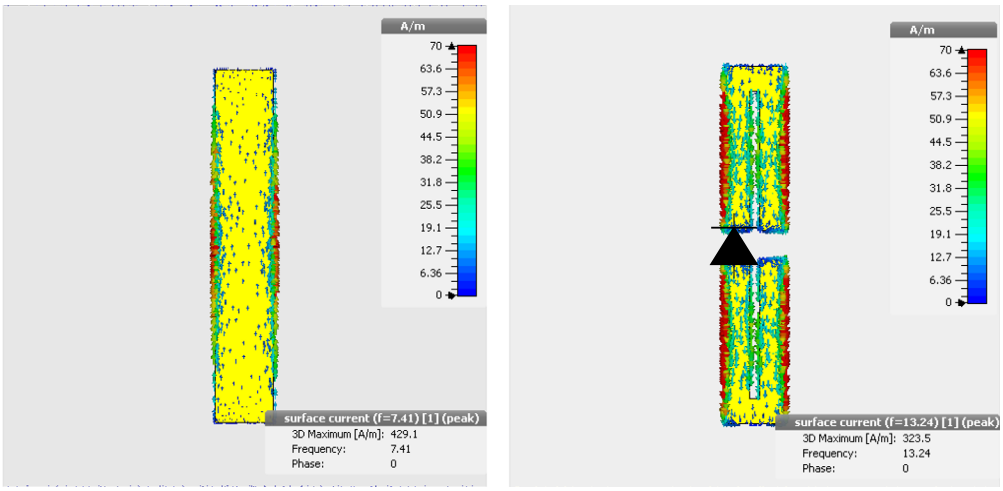

(a) (b)

Figure 4.26: The beam steering cell evolutions: (a) Half wave length dipole current distribution. (b) The proposed cell structure.

The developed cell is described in Fig. 4.26. First, the dipole current distribution is calculated as illustrated in Fig. 4.26 to determine the best position of the varactor diode, as it should highly influence the reflected phase. The dipole length behavior resembles a half wavelength resonance, where the current is maximum at the middle edges and minimum at the ends of the dipole. Therefore, the dipole is splitted to surface mount the varactor diode. Moreover, as the dipole current is concentrated at the outer edges, the dipole is slotted from the middle. The split and slot approaches in the dipole design provide significant improvement to

the performance of the re-radiation losses, the bandwidth enhancement, the phase linearity and range increment.

The reflection phase variation at discrete capacitance values with frequency is illustrated in Fig. 4.27, where 300 degrees tuning phase range is achieved with linear phase curve from 5 GHz to 6 GHz. This novel capability which is phase and frequency reconfigurability fulfills the FC chipless RFID system with independent beam scanning at each frequency point. Hence, the UWB operation is attained while keeping low complexity and cost.

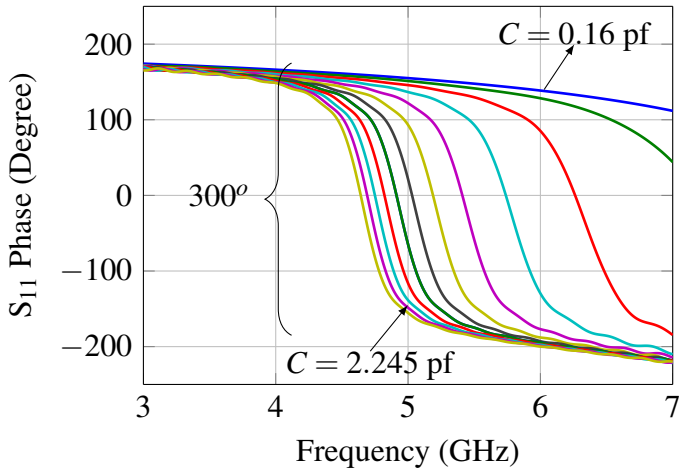

Figure 4.27: The tuned phase curves for the beam steering cell at different capacitance values of the SM2019 varactor diode.

The utilized varactor diode is the off shelf SMV2019 with capacitance values ranging from 0.16 pf to 2.245 pf. The relation between the varactor capacitances and the related applied reversed voltage can be obtained by numerical curve fitting.

4.6.2 Beamsteering RA Antenna Simulations

The beam steering RA antenna which consists of 10×10 cells is implemented in CST. The values of the progressive phase distributions of the RA surface are controlled by loading each cell with a varactor diode on the specified position. Hence, these tuning varactors introduce a small shift in the dipoles resonant frequencies and in accordance to that the reflection phases of the RA cells are changed, so allowing a dynamic phase control of the RA surface. Thus, the radiation pattern of the RA antenna can be steered at any frequency lying in the tuning range from 5 GHz to 6 GHz and the capability of steering simultaneous multi-beams is also achievable. Furthermore, the beam steering RA antenna is 4 times greater in gain and 4 times narrower in

beam-width than the feeder antenna as described in Fig. 4.29. Lastly, the achieved scanning range is ±50° as illustrated in Fig.4.28 at 5.5 GHz.

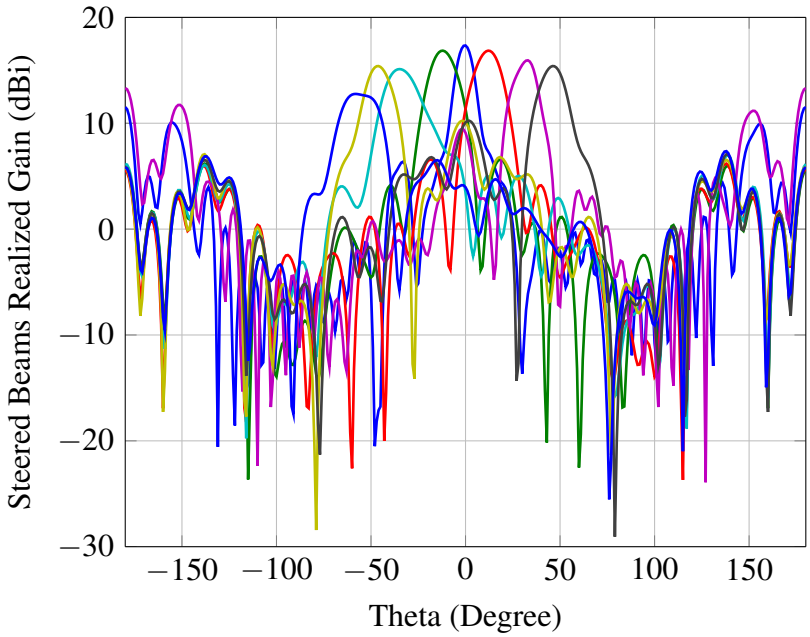

Figure 4.28: The beam steering RA antenna simulated radiation patterns with (−50° to 50°) steering angles at 5.5 GHz

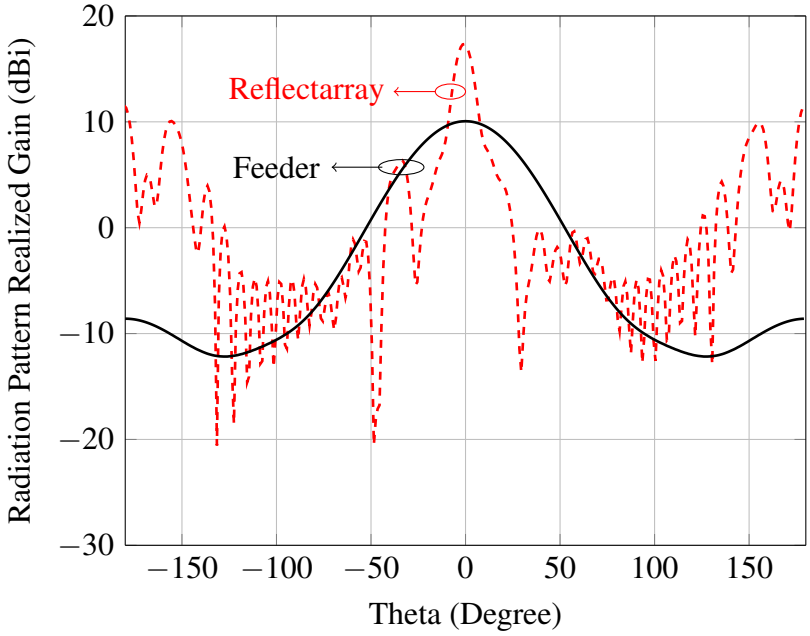

Figure 4.29: The beam steering RA antenna radiation pattern vs the utilized feeder pattern at 5.5 GHz and 0°.

4.7 Conclusion

In this work, novel RA antennas are introduced to be utilized in the chipless RFID readers. The advantages of the presented high gain pencil beam RA antennas are exploited to increase the reading range and enhance the tag detection. Special considerations are devoted to the design simplicity, enlarge the operating bandwidth, improve the spatial resolution, minimize the re-radiation losses and reduce the SLL. Hence, a wideband RA antenna with a small feeder distance is demonstrated first. This developed prototype achieves 300 MHz bandwidth centered at 5.8 GHz. Moreover, the RA produced beam is four times narrower than the feeder beam and thus 6 dB higher in gain with -10 dB SLL. The second developed prototype exploits a designed constant phase center horn antenna to feed the RA surface. Therefore, an UWB RA antenna based on double circular ring resonator cell is demonstrated. Measurements illustrate that the FBW of the developed UWB RA antenna is 37 % covering all the feeder bandwidth and thus fulfilling the requirements of the FC chipless RFID systems. Accordingly, multiple bits accommodation is enabled. Furthermore, the radiated beam is 15° HPBW, 19 dBi gain and -10 dB SLL. Therefore, the developed UWB RA antenna is successfully integrated with the physically modulated tags and a reading range of 1 m is achieved. To the best of the author knowledge, this is the highest reading range achieved in the FC chipless RFID systems, considering real-world indoor environment and software defined radio reader. Afterward, an UWB dual polarized RA is proposed to be utilized with the depolarized tags. The cross polarization isolation level is less than 40 dB. Consequently, the reading range and the detection reliability are enhanced. Finally, an electronic beam scanning RA antenna is demonstrated to be employed in the chipless RFID reader for the first time. Therefore, the cell phases are adjusted to reconfigure the beam to the tag direction electronically. Moreover, this two-dimensional beam steering RA antenna provides large scanning range of $\pm 50°$ with high resolution up to 10° and low SLL less than -10 dB.

5 Novel Nonlinear Physically Modulated Chipless RFID Tags

The main objectives of this chapter are to completely isolate the environmental clutter reflections, increase the reader coverage, and exclude the inevitable calibration measurements required for the conventional chipless RFID systems. These objectives are attained while exploiting the nonlinearity generated from a single unbiased diode integrated with the tag structure. The nonlinearity principle relies on interrogating the tag with a prescribed set of frequency combinations while the tag replies with its unique ID at another frequencies. Therefore the tag-ID is determined based on the used interrogation tones and the exploited nonlinear product. First, the single tone harmonic radar tags are introduced. In this regard, the reader scans the available tags by sending predefined fundamental tones. Among these tones, the tag receives only one and retransmits its corresponding second harmonic representing the tag-ID. Thus, the bandwidth of the tag receiving antenna determines the maximum number of single tone coded tags. In other words, the narrower is the band-pass filter provided by the tag receiving antenna or integrated into it, the more the frequencies that can be used for coding. Afterward, the multi-tone harmonic radar tags are presented aiming at increasing the coding capacity. In this concern, the tag implements the NPM scheme in the second harmonics of the interrogation fundamentals. In this scheme, each realized notch is surrounded by two band edge peaks defining the notch position. Therefore, the tag is interrogated with the fundamental tones of these notches and peaks to determine the existence or non-existence of a particular notch. Hence, the position of these harmonic notches determines the tag-ID, and thus the coding capacity is increased. After that, the mixer based tags are demonstrated, where two simultaneous closely spaced frequencies are utilized for tag interrogation. Then, the designed dual-band tag antenna maximally receives these two tones and delivers them to the diode. Hence, the diode generates the corresponding mixing combinations. Based on the implemented filtering scheme, the retransmitted frequency can be the sum, the difference or even a combination if the interrogation tones exceed two. Herein, the up-converting

mixer product of the used frequency pairs is figured out by the tag transmitting antenna and retransmitted back towards the reader representing the tag-ID. The last introduced category is based on the inter-modulation communication principle, where two co-located frequencies illuminate the tag which respond at an inter-modulated frequency. These inter-modulated products offer a small frequency offset from their fundamentals. Therefore, the minimum frequency difference between the interrogation signals is determined by the antenna filtering ability. In the proposed tag categories the position of the generated peaks or notches is utilized in encoding the tag-ID. Moreover, the phase encoding scheme is proposed and can be exploited to increase the code space. Eventually, the concluding remarks are introduced.

5.1 Introduction

In the previous chapters, the environmental clutter response is mitigated by utilizing the depolarizing tags [11, 14] and employing the high gain pencil beam RA antenna [43, 44] in the reader side. Other methodologies that can also be exploited are the channel equalization [3], the time gating and the reference calibration measurements [14]. All the techniques mentioned above are quite challenging with the multi-tag scenario and when the tag is in proximity to conductive-dielectric objects or operating in dynamic/time-variant environments. Furthermore, the calibration task becomes more complicated if more than one linear polarization is used, because the detection environment has to be well known for each polarization.

This chapter uses the nonlinearity in the tag side to break through these limitations. In literature, few kinds of research are addressing the nonlinearity with the RFID tags. However, the objectives were to track ground insects [57], sense a physical parameter like temperature [58, 59]..etc. The introduced work, in contrast, exploits the nonlinearity with the chipless RFID systems to suppress the environmental reflections, exclude the calibration measurements and attain a high reading range. Moreover, the proposed nonlinear tags are high coding capacity with novel frequency position and phase encoding schemes.

First, the nonlinear tag framework is introduced in Section 5.2. This Section explains the nonlinear device selection, the matching, and the system co-simulation, where the full wave EM simulations are combined with the circuit harmonic balance analysis. Afterward, the single and the multi-tone harmonic radar tags are proposed, and the simulation and the measurement results of each type are demonstrated in Section 5.3. The mixer based tags are presented in Section 5.4, while the inter-modulation based tags are introduced Section 5.5. Moreover, the

antenna requirements for each tag category, the suppression level of the undesired tones and the associated filtering requirements are clarified. Section 5.6 illustrates the capability of phase modulation for the nonlinear chipless RFID system. Finally, a concluding discussion and remarks are presented.

5.2 Non linear Tag Framework

The diode is a two port network where the nonlinearity is acquired from the nonlinear I-V relationship governed by Eq. 5.1:

$$I = I_s \left(e^{\alpha V} - 1\right) \tag{5.1}$$

where I_s is the diode saturation current, $\alpha = q/nkT$, q is the electron charge, k is the Boltzmann's constant, T is the temperature in Kelvin, V is the voltage drop across the diode, n is the ideality factor which determines the quality of the diode structure. The diode output current can be driven using Taylor series in eq. 5.2:

$$I = a_0 + a_1 V + a_2 V^2 + a_3 V^3 + ... \tag{5.2}$$

Assuming that the diode applied voltage is $V = A\cos(\omega_1 t) + B\cos(\omega_2 t)$ and ignoring the Direct Current (DC) term, the output current is expressed in eq. 5.3:

$$\begin{aligned} I = {} & a_1(A.Cos(\omega_1 t) + B.Cos(\omega_2 t)) + a_2(A.Cos(\omega_1 t) + B.Cos(\omega_2 t))^2 + \\ & a_3(A.Cos(\omega_1 t) + B.Cos(\omega_2 t))^3 + .. \end{aligned} \tag{5.3}$$

The second order terms are illustrated in eq.5.4, while the third order terms are explained in eq. 5.5:

$$2^{nd}\ terms = \frac{a_2}{2}(A^2\cos(2\omega_1 t) + B^2\cos(2\omega_2 t)) + a_2 AB(\cos(\omega_1 + \omega_2)t + \cos(\omega_1 - \omega_2)t) \tag{5.4}$$

$$\begin{aligned} 3^{rd} terms = {} & \frac{a3}{4}(A^3\cos 3\omega_1 t + B^3\cos 3\omega_2 t + 3A^2 B(\cos(2\omega_1 + \omega_2)t) + \\ & AB(\cos(2\omega_1 - \omega_2)t) + 3AB^2(\cos(\omega_1 + 2\omega_2)t) + AB(\cos(\omega_1 - 2\omega_2)t)) + .. \end{aligned} \tag{5.5}$$

Hence, these nonlinear components generated by the diode are exploited for tag identification, robust detection and so on.

5.2.1 Diode Selection

Choosing the appropriate diode for the desired objectives is a trade off between cost, sensitivity, conversion efficiency and operating frequency range. Schottky diodes are the best suitable candidate since they are one side diffusion (metal junction), so no barrier potential to exceed. The disadvantage of the Schottky diodes is that the reverse leakage current is relatively higher than the conventional p-n junction diodes. However, this reverse current can be prohibited with the aid of the embedded filter. During the work of this thesis, the zero biasing HSMS-2850 Schottky diode is chosen due to its high sensitivity and low-cost packaging. Therefore, this diode is well suited for the mass production applications such as chipless RFID tags. The diode circuit model as described in Fig.5.1 consists of series inductor L_s and resistor R_s connected to parallel junction resistance R_j and capacitance C_j. Besides, parasitics of the cheapest (SOT-323) packaging are included. These parasitics are the inductance L_p and capacitance C_p.

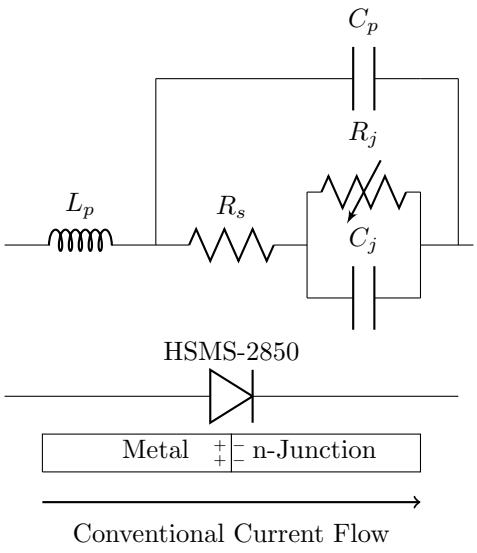

Figure 5.1: Nonlinear device model and circuit elements.

5.2.2 Diode Matching

The input impedance of the diode is quite far from the typical 50 Ω employed in the microwave circuits and to get most of the power into the diode; a matching network is necessary. The challenges are that the input impedance of the diode and the matching network elements vary with the input power, frequency, temperature and the other ambient conditions. However, in the case of narrow band operation, appropriate stubs can be employed to provide matching at a

certain frequency point as shown in Fig.5.2. Therefore, the scattering parameters of the diode circuit model under matched and unmatched conditions is shown in Fig.5.3.a. These results elucidate that the stub matching can be suitable for the single tone harmonic radar tags where the tag captures only one fundamental frequency and produce a maximum at the corresponding second harmonic. This matching circuit assumes that the diode is zero biased; however, the junction resistance and capacitance vary with the applied voltage, so the input impedance varies too.

The Conversion Loss (CL) that relates the output power of the desired frequency to the input power of the fundamental, as defined by Eq.5.6 is better at low input power as shown in Fig. 5.3.b and it gets worse beyond 0 dBm input power. Thus, the higher is the available power at the diode input; the lower is the conversion loss but, the worse is the matching and vice versa.

$$CL(\text{dB}) = P_{\text{in}_{\text{fund}}}(\text{dBm}) - P_{\text{out}_{\text{harm}}}(\text{dBm}) = -CG(\text{dB}) \tag{5.6}$$

where $P_{\text{in}_{\text{fund}}}$ is the power in fundamental tone, $P_{\text{out}_{\text{harm}}}$ is the power of the corresponding second harmonic and CG is the conversion gain.

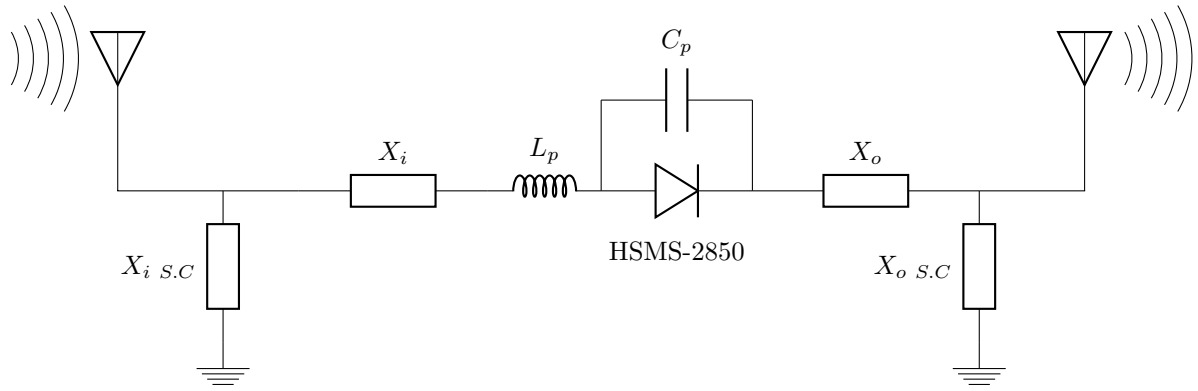

Figure 5.2: Narrow band matching circuit diagram.

On the other hand, for wideband matching the multiple quarter wavelength Chebyshev transformers [58] can be used at the expense of unwieldy tag size. Therefore, to retain the tag compactness and simplicity, the matching networks are excluded. The simulation results explained in Fig. 5.3.b determine how far the CL can be improved if a matching network is employed.

The diode is placed on a capacitive gap along 50 Ω transmission line without matching circuits to measure the CL. The measured CL as illustrated in Fig.5.4 lies between -25 dBm to

-48 dBm corresponding to 10 to -30 dBm diode input power. However the second harmonic CL for the same diode in [60] lies between -45.4 dBm to -72 dBm and the corresponding input power is from 0 to -10 dBm. This enhancement resulted from the exploitation of the diode parasitics and the utilization of the capacitive gap along the transmission line to somehow minimize the diode reflections over the objected frequencies. Consequently, the CL is within the same range of the matched diode introduced in [58].

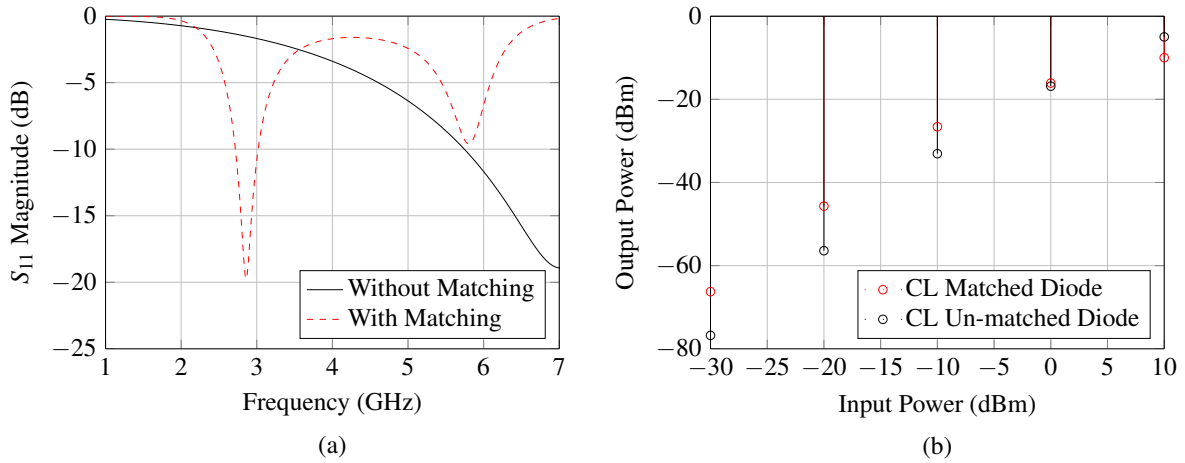

Figure 5.3: HSMS-2850 circuit simulation: (a) S_{11} magnitude for the diode circuit model with and without matching conditions. (b) CL for the matched and the unmatched diode with respect to the input power at 2.9 GHz.

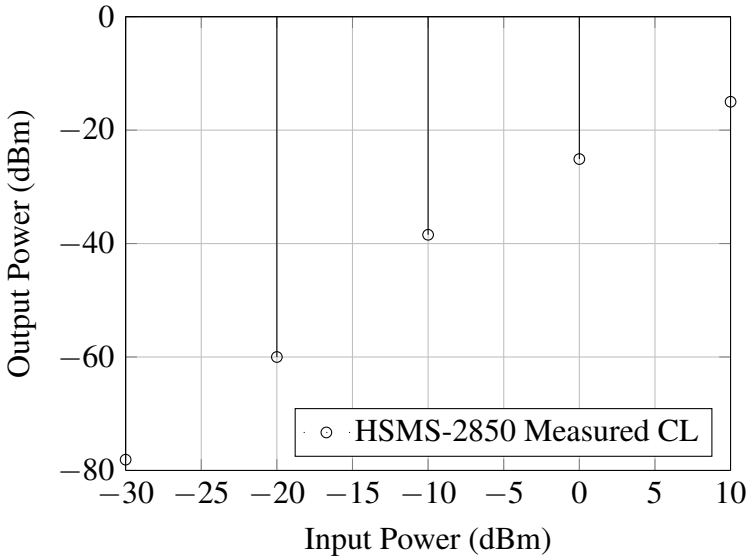

Figure 5.4: Measured CL for the HSMS-2850 diode at 2.9 GHz with different input power levels.

5.2.3 Simulation Environment

The complete system simulation setup is combining the reader antennas, the tag transmitting and receiving antennas, the diode fixture, and nonlinearity in the co-simulation environment. Thus, the EM simulation enables including the incident power density, incoming wave direction and the integration effects in the nonlinear circuit simulation. Hence, the results obtained from the EM simulation (S-parameters) are included in the nonlinear Harmonic Balance (HB) analysis that analyzes the spectral lines produced from the tag. Therefore, the circuit co-simulation with the EM simulation outperform the analysis method in [61] which approximate the tag circuit using Thevenin equivalent theorem.

5.2.4 Link Budget and Power Analysis

The Friis transmission formula is used to calculate the link budget and power analysis for the reader to tag communication and the tag to reader replay. Considering the harmonic radar tags, the total received power in the reader side is calculated based on Eq. 5.7:

$$P_r = P_t G_t G_r (\frac{\lambda_f}{4\pi r})^2 G_{tf} G_{th} (\frac{\lambda_h}{4\pi r})^2 (PLF)(CL) \tag{5.7}$$

$$P_r = P_t + G_t + G_r - L_f + G_{tf} + G_{th} - L_b - CL - PLF \tag{5.8}$$

where P_r is the reader received power, P_t is the transmitted power, G_t is the transmitting antenna gain, G_r is the receiving antenna gain, λ_f is the fundamental tone wavelength, G_{tf} is the tag receiving antenna gain, G_{th} is the tag transmitting antenna gain, λ_h is the harmonic tone wavelength and PLF denotes the polarization loss factor.

With the same analogy, the link budget analysis can be applied to the multi-tone harmonic, mixer and inter-modulation tags. Therefore, the diode CL variation is calculated at different input frequencies as shown in Fig. 5.5 and assuming that the diode input power is -10 dBm. It is illustrated in Fig. 5.5 that the measured CL varies with frequency. The CL lies between -26.6 dBm to -30.5 dBm corresponding to the input frequencies from 1 GHz to 3 GHz. Thus, the maximum reading range can be estimated considering reader sensitivity P_{rmin} using Eq. 5.9:

$$r_{max} = \frac{1}{4\pi} (\frac{P_t G_t G_r G_{df} G_{dh} \lambda_f^2 \lambda_h^2 (CL)(PLF)}{P_{rmin}})^{\frac{1}{4}} \tag{5.9}$$

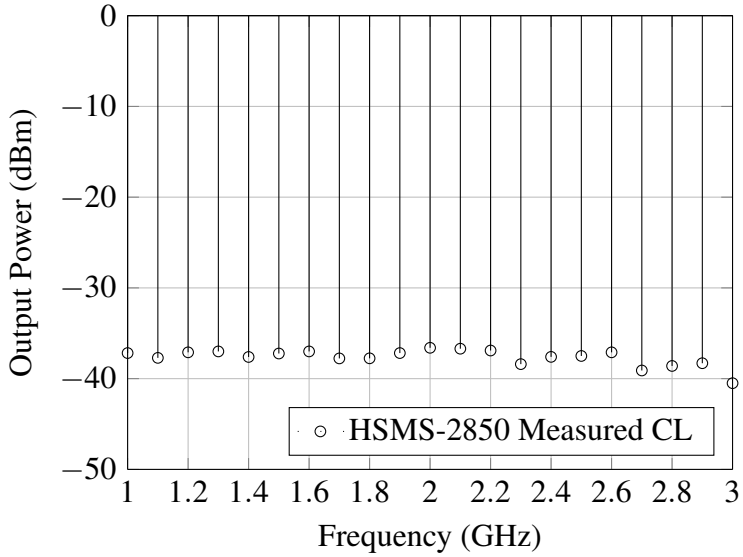

Figure 5.5: Measured CL variation at the second harmonic of the frequency range from 1 GHz to 3 GHz for the HSMS-2850 diode at −10 dBm input power.

5.3 Harmonic Radar Tags

In this section, the single tone harmonic radar tag is presented. The tag design, simulations, and measurements are demonstrated. Afterward, the multi-tone interrogation is explored. Therefore, the multi-bit information is enabled without the need of the IC. As a consequence the system description and the tag design, simulations are illustrated. Furthermore, the real world measurements are demonstrated.

5.3.1 Single Tone Harmonic Radar Tags

The introduced tag consists of two specified patch antennas integrated with a single unbiased diode that generates the nonlinear response as depicted in Fig.5.6. The designed narrow band preselecting and filtering tag antenna is depicted in Fig.5.7. This patch is characterized with width W, length L, and realized on Ro5870 substrate with $\varepsilon_r = 2.33$ and thickness $h = 1.58$ mm. The initial patch dimensions are determined using Eqs. 5.10 - 5.11. After that, the patch parameters are best optimized for minimum return loss and maximum gain.

The fundamental patch antenna is designed at 2.9 GHz and thus the corresponding second harmonic retransmitting antenna is designed at 5.8 GHz. The simulated and measured S_{11} for

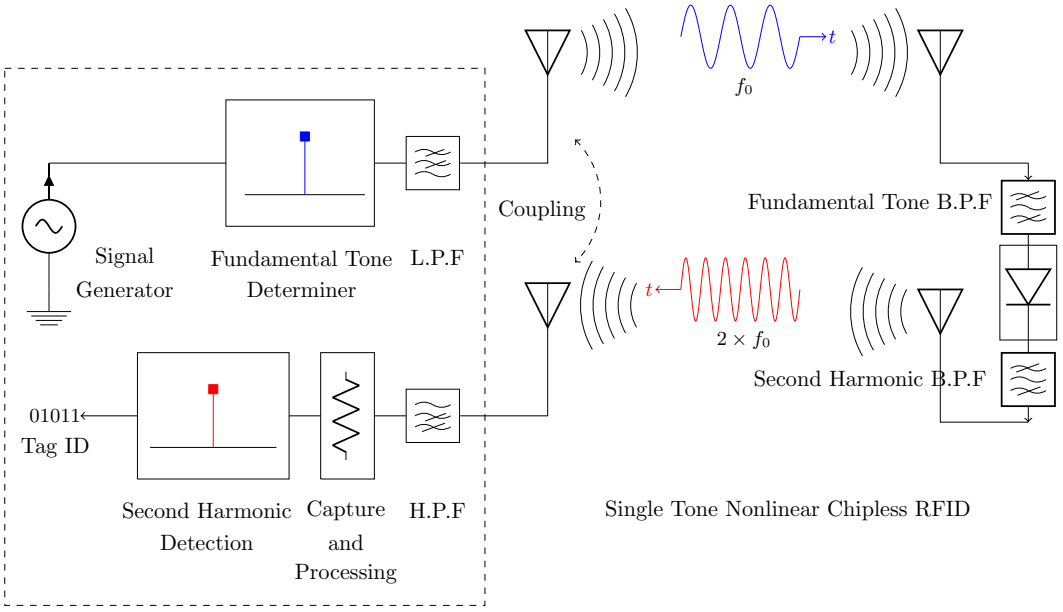

Figure 5.6: One-bit harmonic radar nonlinear chipless RFID system description.

both antennas are in a good match as explained in Fig. 5.8. Furthermore, the second harmonic of the fundamental antenna is minimized with the aid of the step in width impedances.

$$W = L = \frac{c}{(2f\sqrt{\varepsilon_r})},\ H = \frac{0.88 \times L}{2} \tag{5.10}$$

$$Y = \frac{W}{5},\ X = Z = \frac{2 \times W}{5} \tag{5.11}$$

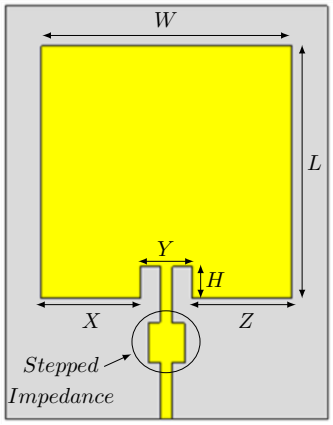

Figure 5.7: One-bit harmonic radar tag receiving antenna with step in width impedance to minimize the harmonics.

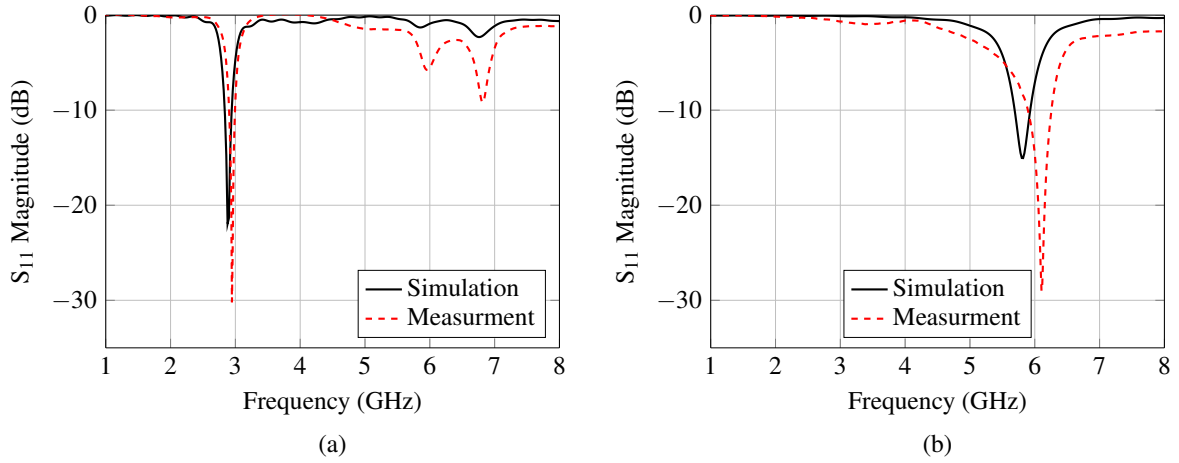

Figure 5.8: One-bit harmonic radar tag antennas simulations and measurements: (a) Simulated and measured return loss for the fundamental patch antenna. (b) Simulated and measured return loss for the corresponding second harmonic patch antenna.

5.3.2 Complete Tag Simulation and Indoor Measurements

The complete tag is integrated, and the EM simulation is performed to include the influence of integration, polarization mismatch and tag reading distance into account as illustrated in Fig. 5.9.a. Afterward, the tag is co-simulated with the harmonic balance analysis to acquire the spectral lines and the corresponding diode conversion loss. The reader transmitted power is 20 dBm, and the tag is placed at 50 cm apart from the reader antennas. The total received power at the double frequency is -54.384 dBm as shown in Fig. 5.10.a which is verified with the link budget and power analysis. Thus, the estimated CL is approximately -25 dBm.

The indoor measurement setup as explained in Fig.5.9 uses two LPDA antennas for transmitting the fundamental and receiving the second harmonic signal. Thus, the transmitting antenna is connected to a signal generator with 20 dBm output power, and the receiving antenna is connected to a spectrum analyzer to catch the tag backscattered second harmonic tone. The tag is placed in the broadside direction of the LPDA antennas at 50 cm distance. Thus, the forward path loss is $L_f = -41.7$ dB and the backward path loss is $L_b = -47.7$ dB. The polarization mismatch is approximately equal to $\cos\theta = 0.692$. The measured diode CL at 2.9 GHz is -38.6 dB as illustrated in Fig. 5.5, which is less than the simulated one by -13 dBm. Lastly, the complete tag spectral line measurements as explained in Fig. 5.10.b verifies the tag operation and agrees well with the link budget analysis and power calculations.

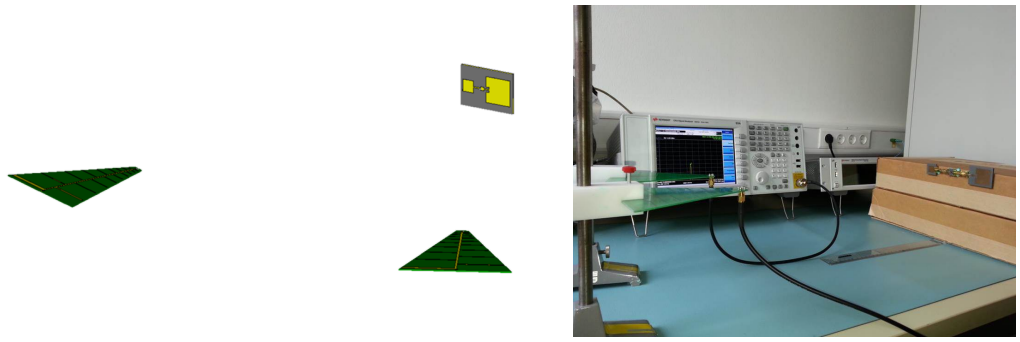

(a) (b)

Figure 5.9: Single tone harmonic radar simulation and measurement setup: (a) EM and harmonic balance simulation setup utilizing CST co-simulation. (b) System indoor measurement setup.

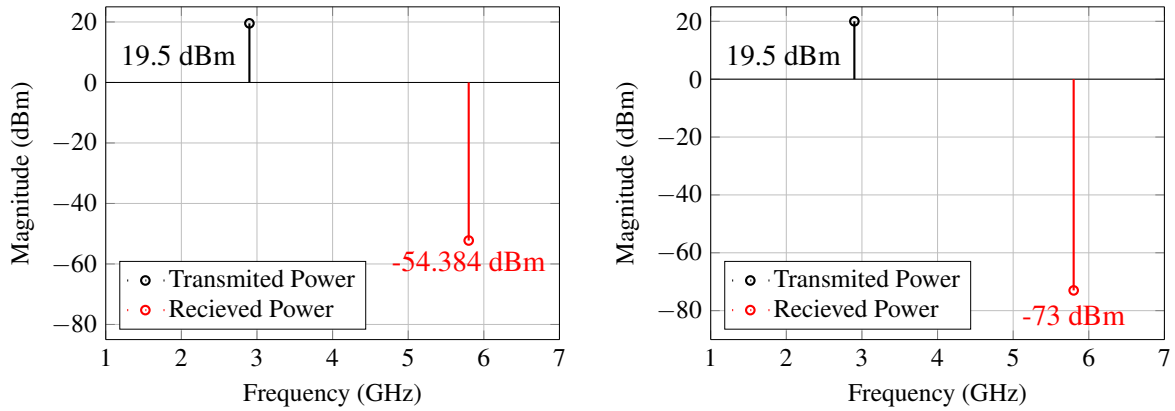

Figure 5.10: Single tone harmonic radar nonlinear simulation and measurement results: (a) Simulated transmitted and received power spectral lines. (b) Measured received power at 5.8 GHz while transmitting 2.9 GHz with 19.5 dBm power.

5.3.3 Multi-tone Harmonic Radar Tags

The multi-tone harmonic radar approach relies on interrogating the tag with a prescribed set of fundamental tones in time regulated methodology, and the tag implements notches in the second harmonic of these fundamentals as described in Fig. 5.11. Each notched frequency is surrounded by two band edge peaks defining the notch position. Hence, three different interrogation frequencies are used to determine the existence or non-existence of a particular notch. Accordingly, the second harmonic of the intermediate frequency is at the notch position and the second harmonics of the other two fundamental tones are at the surrounding peaks. Hence, the position of these harmonic notches determine the tag-ID, and thus the coding capacity is increased.

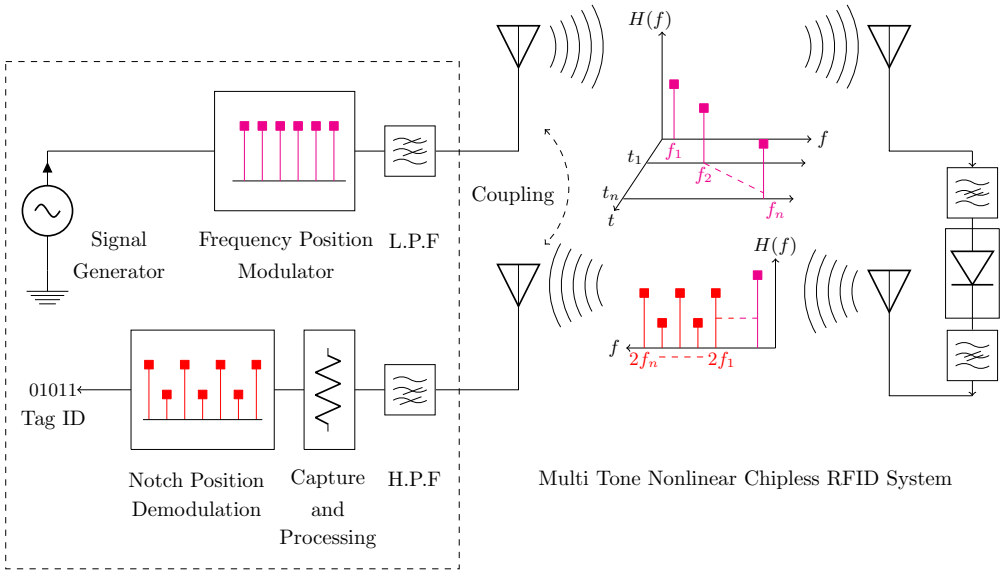

Figure 5.11: Multi-tone harmonic radar nonlinear chipless RFID system description.

The tag consists of receiving antenna, two multi-stop band filters before and after the nonlinear element and transmitting antenna as shown in Fig.5.11. One key feature of the introduced tag structure is that it is completely planar based on CPW technology which provides easy series or parallel integration of the nonlinear element as depicted in Fig 5.12.

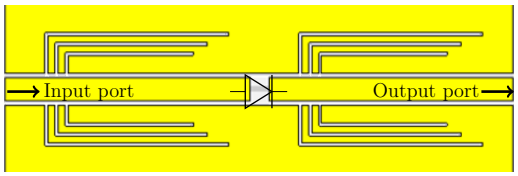

(a) Series connection

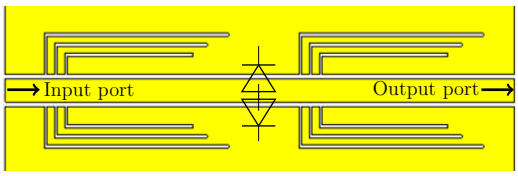

(b) Parallel conection

Figure 5.12: Multi-tone series and parallel diode integration capability: (a) Diode series connection configuration. (b) Parallel connection configuration.

First, the tag receiving CPW UWB monopole antenna catches the fundamental tones which pass through the first multi-stop band filter. This filter blocks the diode reverse leakage harmonics from retransmission. Afterward, these fundamental tones are conveyed to the diode for generating

the harmonic frequencies. These converted frequencies are delivered to the second multi-stop band filter which implements the physical encoding scheme and generates the tag-ID. Finally, the resultant notches and peaks at the second harmonic frequencies are retransmitted back by the tag transmitting antenna. The used fundamental tones are within the frequency range of 1.5 GHz to 3 GHz, so the tag receiving antenna operates in this range. In accordance with that, the tag transmitting antenna operates from 3 GHz to 6 GHz. The simulated and measured reflection coefficient of the tag antennas as demonstrated in Fig.5.13 satisfy these requirements.

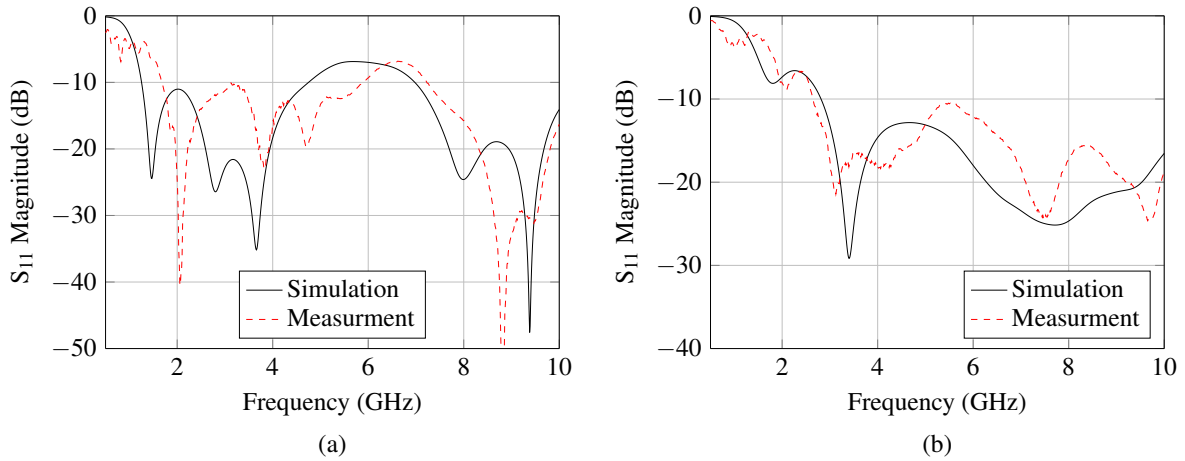

Figure 5.13: Multi-tone harmonic radar tag antennas: (a) Receiving CPW UWB monopole antenna simulation and measurement. (b) Simulated and measured return loss for the tag transmitting antenna.

6-bit tag prototype is designed, simulated and measured to prove the concept. First, this prototype filtering operation is verified in the presence of the diode. Therefore, both fundamental and harmonic tones are being entered from one side, and their corresponding output is being observed at the same frequency. The prototype measured response is illustrated in Fig.5.14, where the 6 notches are clearly defined. Afterward, the input side of this prototype is connected to a signal generator with 0 dBm output power, and the prototype output is analyzed using spectrum analyzer as demonstrated in Fig. 5.15. The input fundamentals are from 1.5 GHz to 3 GHz and thus propagate through the prototype without being notched. However, the 6 notches which symbolize the tag coding bits are observed at the second harmonic frequencies of these fundamentals from 3 GHz to 6 GHz. The power reached the diode is about −10 dB, consequently, the CL is about -28 dBm. The measured second harmonics which are generated from feeding the introduced prototype with their corresponding fundamentals as shown in Fig. 5.15 verifies the multi-tone harmonic radar approach. However, the sixth notch is diminished because of the

asymmetry filter response and also the notches are slightly shifted right. Therefore, the number of coding notches is reduced to three to ensure a uniform filter response at their corresponding input fundamental tones.

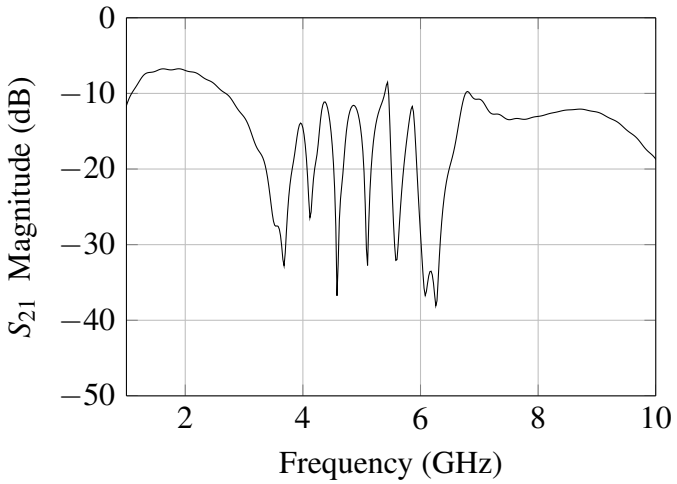

Figure 5.14: Multi-tone 6-bit prototype linear measurements.

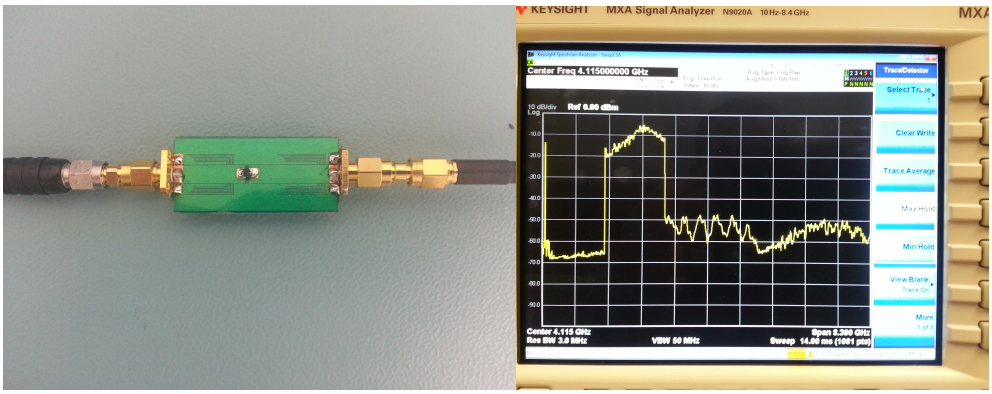

Figure 5.15: Multi-stop band filter 6-bit prototype which is integrated with the diode and connected to a signal generator with 0 dBm output power from one side and to spectrum analyzer from the other side.

The complete tag is integrated as demonstrated in Fig.5.16. Two LPDA antennas are connected to the generator and the spectrum analyzer which are acting as the reader with 20 dBm transmitted power. Hence, the tag is placed in the broadside directions of the reader antennas to verify the tag operation. Three harmonic notches are implemented in the frequency range from 3 GHz to 6 GHz as explained in Fig.5.16. Consequently, the interrogation fundamentals are from 1 GHz to 3 GHz. Therefore, the retransmitted harmonic peaks and notches that codify the tag-ID are shown in Fig.5.17.

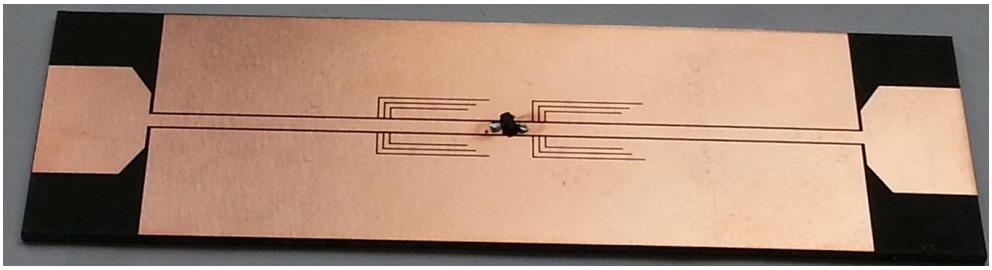

Figure 5.16: Multi-tone harmonic radar complete tag structure clarifying the 3-bit code.

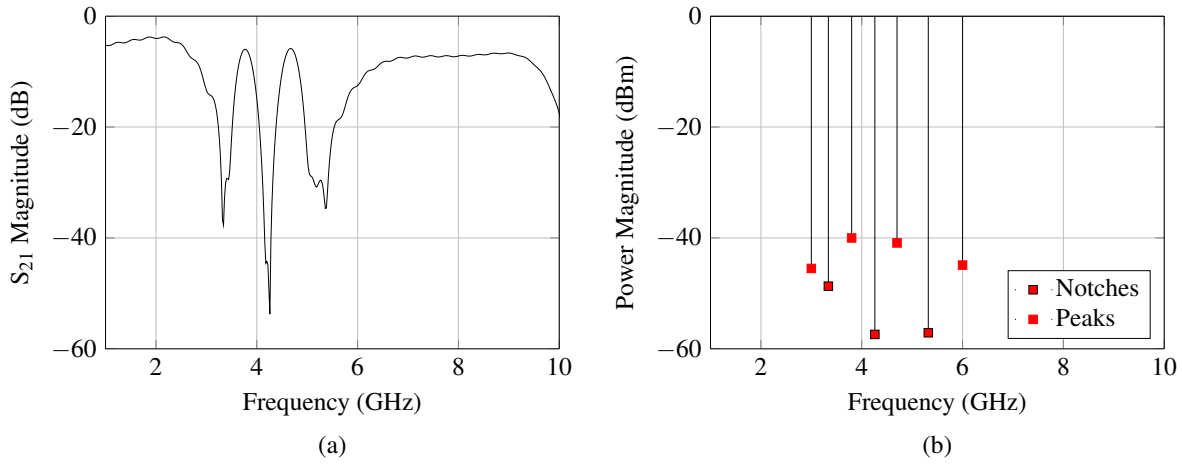

Figure 5.17: Multi-tone harmonic radar measurement: (a) Scattering parameters (linear measurements) (b) Power spectral lines (nonlinear measurements).

The introduced multi-tone harmonic radar tag reading range is about 20 cm for -90 dB reader sensitivity. This small coverage is due to the following reasons. The first one is that the tag antennas are UWB operation. Therefore, their gain is about 1.5 dB. The second reason is that the integrated tag antennas influence the notches at the second harmonic frequencies regarding their dynamic level. Moreover, the two multi-stop band filters insertion loss is about -10 dB. Therefore, for the sake of size miniaturization, and loss reduction the first band stop filter can be excluded by using appropriate tag receiving antenna. This antenna has to prohibit the diode reverse leakage on the expense of reducing the coding frequency range. Moreover, a reference tag should be used for calibration which is a limiting factor. Thus, introducing coding peaks is more robust and easier to be detected.

5.4 Novel Mixer Tags

In this section the nonlinear mixer based tags are introduced, where two co-located frequencies are exploited in tag interrogation. The tag, in turn, receives these two tones and generates the corresponding nonlinear combinations. After that, the tag transmitting antenna figures out the desired tone to be transmitted back towards the reader. The figured out mixer product can be the sum or the difference. However, the exploited mixer product is the sum which leads to smaller tag transmitting antenna. Therefore, the block diagram of the introduced up-converting mixer based nonlinear chipless RFID system is clarified in Fig. 5.18.

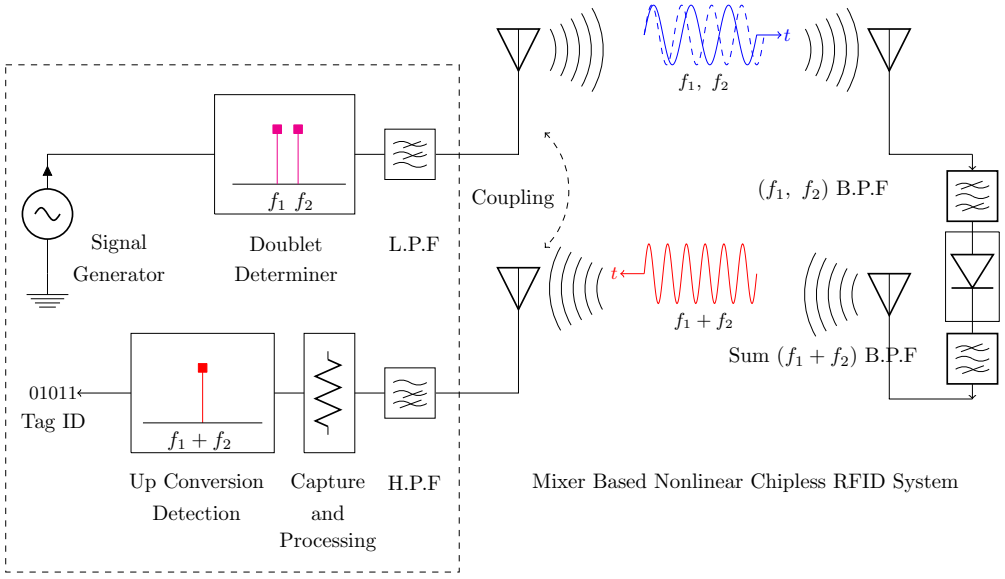

Figure 5.18: Nonlinear mixer based chipless RFID system description.

The mixer's tag receiving antenna should operate over two closely spaced frequency bands to be able to capture the two co-located interrogating tones. Therefore, this dual-band antenna has to operate with similar features at the two working bands, concerning the radiation pattern, polarization, impedance matching, and the other antenna parameters. However, the design of such antenna is not a straightforward matter. One approach to realize a dual-band antenna is to have two patches with two distinct radiating resonator lengths. These two resonators can be stacked or connected with $\lambda/2$ separation space. The lowest resonance frequency determines the space length and the overall tag footprint. Therefore, this approach yields a significant tag size and a complex antenna structure. Another method to design a dual-band antenna is to use the metamaterial structures. The incorporation of these structures while engineering the dispersion

diagram of the different modes enables nearby resonances with small antenna size [62]. The propagation constant of such antenna consists of Right Hand (RH) and Left Hand (LH) sections. The LH sections are inversely proportional to frequency, and thus the propagation constant equation can be written as following:

$$\beta L_n = \beta_n^{RH} d + \beta_n^{LH} d = k_1 f_n d - \frac{k_2}{f_n} l = n\pi \tag{5.12}$$

Where d is the RH section length, l is the LH section length, k_1 and k_2 are constants. Thus, for M unit cells LH sections, the propagation mode value n takes values $n = -M+1, -M+2, ...0, +1, +2, ...$ Therefore the dual-band operation can be attained with $M = 2$ and $n = \pm 1$. Although, the metamaterial antennas are small size, but, the gain, and radiation efficiency are still lower than the microstrip patch antennas [62]. Hence, these approaches mentioned above are not preferred.

The exploited approach is to have an initial patch of ordinary shape and embed appropriate current perturbation to this shape with suitable slots or slits [63]. The slots are engineered to provide control over the patch modes which are satisfying the condition of $\beta L_n = n\pi$. Thus, the fundamental mode is TM_{100}, the following mode is the TM_{200} which has a broadside null and so this mode can not be employed for the second band. The next subsequent mode is the TM_{300}, which has similar radiation properties like the fundamental one, but it introduces grating lobes beside the main lobe. Furthermore, the resonance frequency of this mode is relatively spaced from the fundamental one by a ratio of approximately 3 [63]. However, this frequency separation can be altered by reactive loading the microstrip antenna and thus the grating lobes can be minimized. Therefore, a rectangular microstrip antenna is designed first with fundamental resonance frequency at 2.3 GHz as shown in Fig.5.20.a. It is observed that the TM_{200} and TM_{300} modes resonances are spaced from the fundamental mode by a ratio of 1.91 and 2.82 respectively. Moreover, the TM_{200} radiation pattern consists of two major lobes with a null in the broadside directions. However, the TM_{300} radiation pattern consists of three major lobes as shown in 5.21.a. So, the TM_{300} mode is most similar to the fundamental mode with one main lobe and two grating lobes. Thus, two reactively loaded slots are etched inside the microstrip antenna as illustrated in Fig.5.19. These narrow slits are placed near and parallel to the radiating edges where the TM_{100} current is minimum, so the current distribution of the fundamental mode is conserved and slightly perturbed. Hence, the f_{100} is delicately reduced from 2.3 to 2.19. However, these two slits are strongly affected the TM_{300}. Therefore, the TM_{300} currents circulate these slits

introducing a resonant condition near the edges null. Consequently, the resonance frequency of the TM_{300} is reduced.

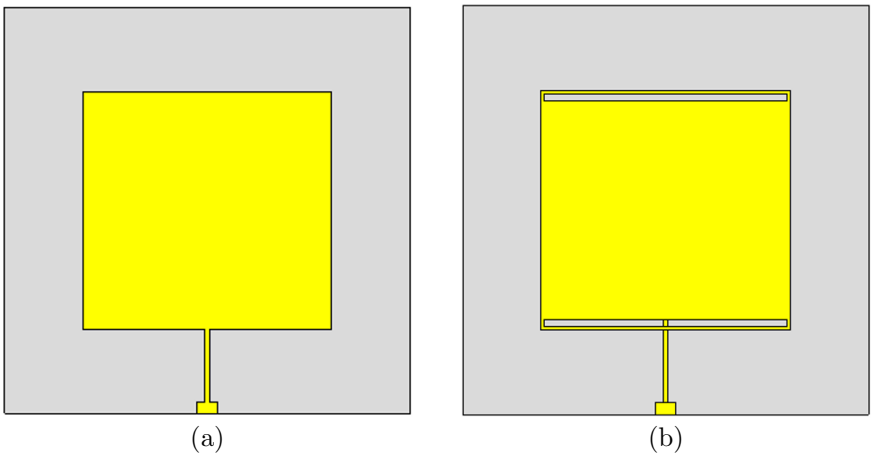

Figure 5.19: Geometry evolutions for the designed patches: (a) Geometry of the rectangular patch antenna. (b) Dual-band rectangular patch antenna with slots reactive loading.

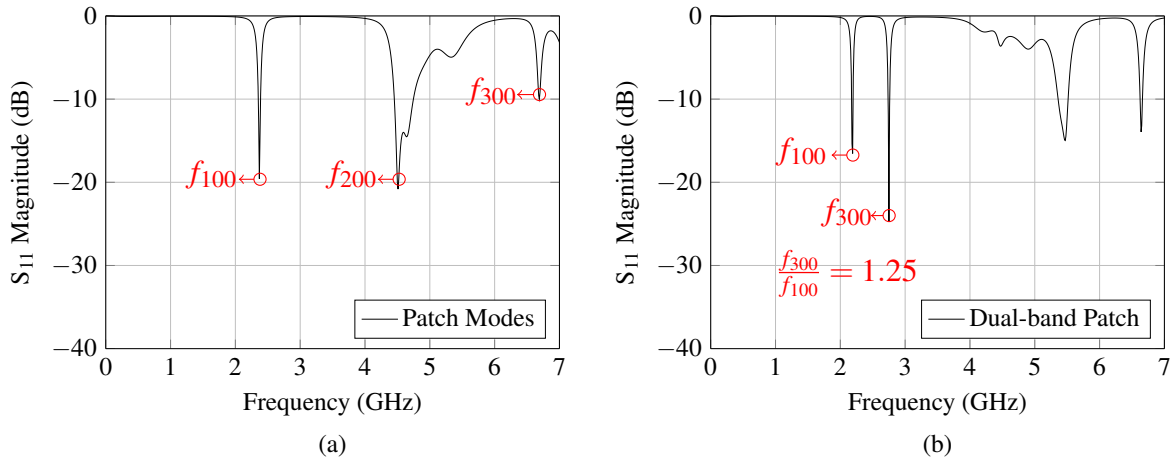

Figure 5.20: Resonance frequencies for the designed microstrip patch antennas: (a) Reflection coefficient for the microstrip antenna illustrating the resonance frequencies of the different modes. (b) Return loss for the designed dual-band antenna.

The achieved frequency f_{300}/f_{100} ratio is about 1.25 as shown in Fig. 5.20.b. It is clearly noticed that both resonance modes are radiating linear polarized waves in the broadside directions with quite similar antenna parameters as depicted in Fig. 5.21. Moreover, the -10 dB FBW for both bands is likely the same. Therefore, the two co-located interrogation tones are arbitrary chosen, but the minimum resonances separation ratio which is 1.25 should be respected. Thus the complete up-converting mixer based tag is integrated for both linear and nonlinear simulations.

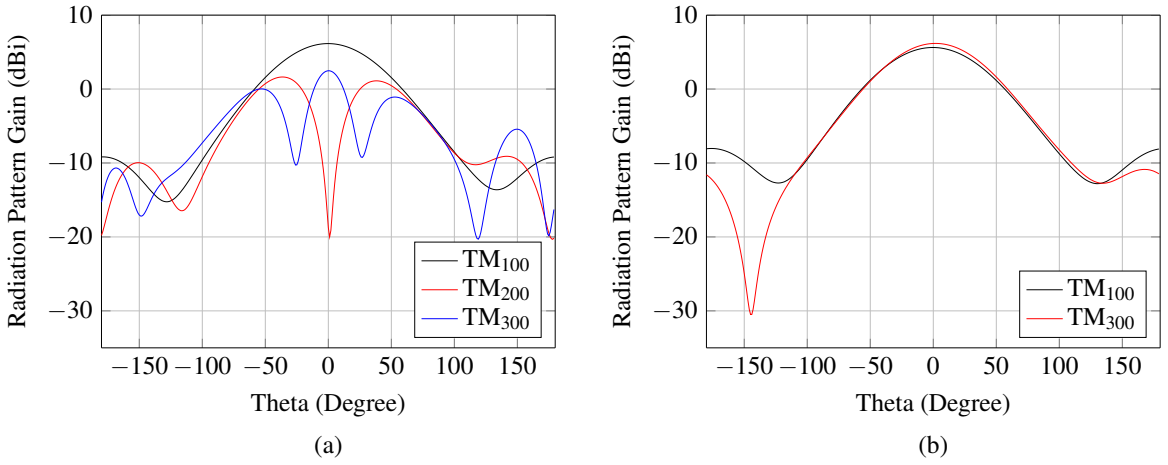

Figure 5.21: Simulated radiation pattern for the designed microstrip antennas: (a) Radiation pattern for the single band antenna and the corresponding modes. (b) Radiation pattern for the dual-band antenna illustrating quite similar radiation properties at each band.

The simulation setup is described in Fig.5.22, where the tag receiving and transmitting, antennas are connected through the HSMS-2850 diode in the middle. Hence, the tag is placed in the broadside direction of the two LPDA antennas to perform the full wave simulation of the complete system as shown in Fig.5.22. The full wave simulation for the tag receiving antenna verifies its dual-band operation at 2.2 GHz and 2.75 GHz. Also, it confirms that the tag transmitting antenna operates at 4.95 GHz as shown in Fig. 5.22.a.

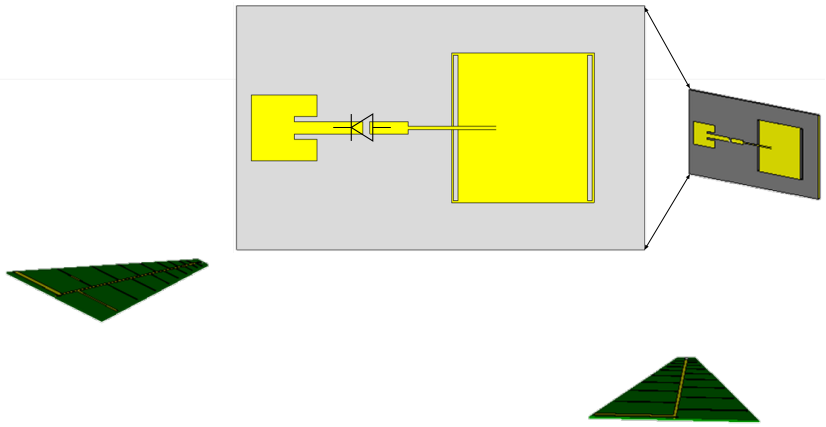

Figure 5.22: Mixer based tag full wave simulation setup.

After verifying the full wave simulation, the harmonic balance analysis is conducted where the two closed frequencies $(1.25, 1.75)$ are used for interrogating the tag as shown in Fig.5.24. Hence, the tag receiving antenna catches these two frequencies and convey them to the diode

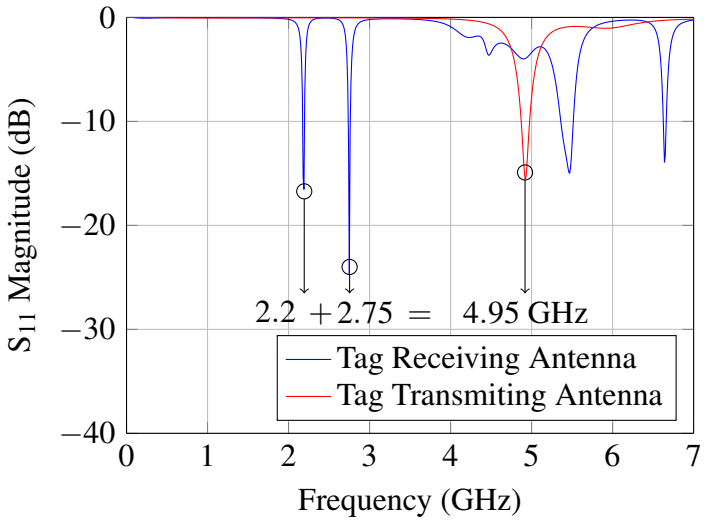

Figure 5.23: Reflection coefficients for the receiving and transmitting mixer based tag antennas illustrating the up-converting mixing operation.

input. The diode, in turn, generates all the mixing products of these two tones and deliver the information to the tag transmitting antenna. The tag transmitting antenna is matched at the addition of these two tones. Thus, this frequency sum is maximally transmitted towards the reader LPDA antenna. The spectral lines at the reader side are illustrated in Fig. 5.25 where the transmitted power is 20 dBm and the CL is about -20 dBm. The received tag response is about −60 dBm, which is verified by the link budget and power analysis.

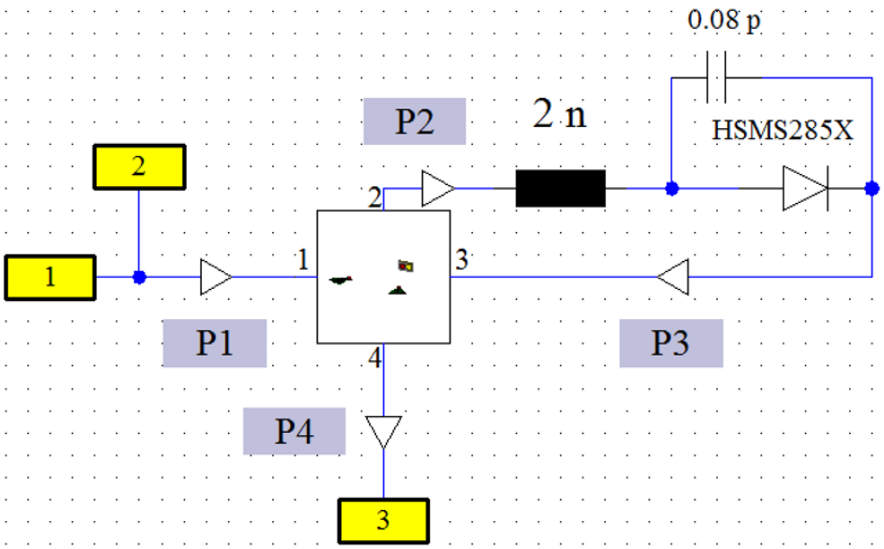

Figure 5.24: Mixer based tag harmonic balance analysis setup.

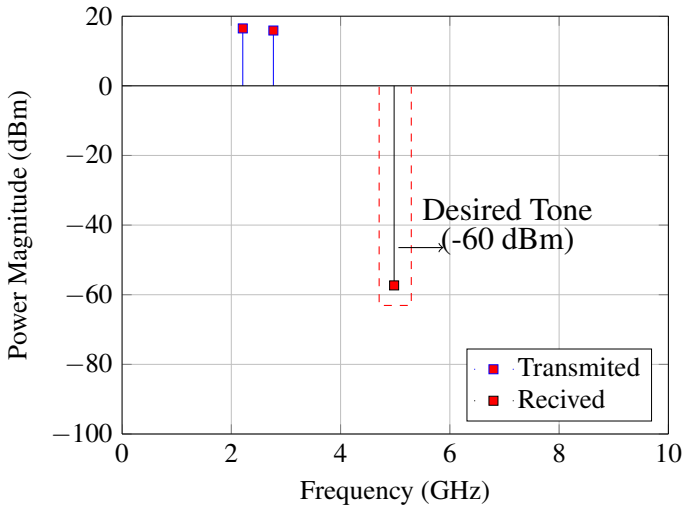

Figure 5.25: Spectral lines for the mixer based tag.

5.5 Novel Inter-modulation Tags

The inter-modulation communication principle is illustrated in Fig. 5.26 where two simultaneous arbitrary tones are utilized for tag interrogation. The generated inter-modulated products are relatively close to the interrogation frequencies as described in Fig. 5.26, so it is less frequency span than the harmonic and mixer tags. Thus, it can be better comply with the existing regulations with less expensive circuits and so on. However, the disadvantage is that the inter-modulated tones are based on the diode third order nonlinear terms, which is higher CL than the second order terms.

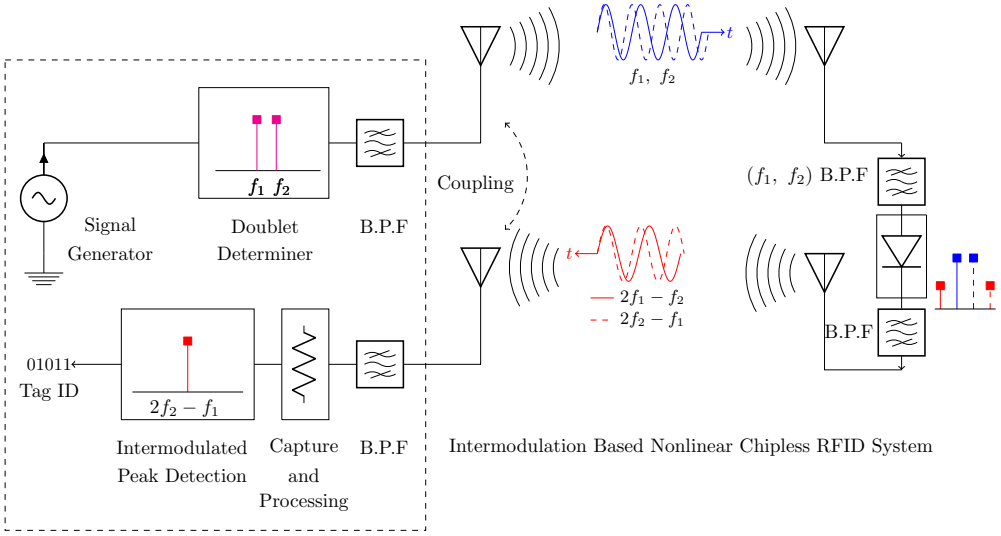

Figure 5.26: Nonlinear inter-modulation based chipless RFID system description.

The dual-band microstrip antenna introduced in the former section is used for the tag receiving antenna. Therefor, the interrogation frequencies are kept the same frequency ratio which is 1.25. Hence, the introduced tag is interrogated by two co-located frequencies and the diode, in turn, generates the Inter Modulation (IM) products of these two tones. Afterward, the tag transmitting antenna as illustrated in Fig. 5.27 retransmits the upper IM product. The harmonic balance analysis is conducted, and the tag spectral lines are explained in Fig. 5.28. These results illustrate that the IM simulated CL is about -35 dBm which is less than the second order products by -15 dBm.

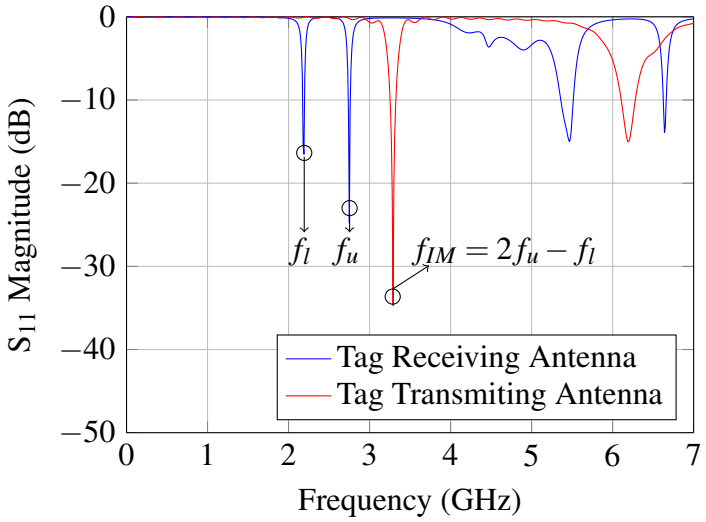

Figure 5.27: Inter-modulation based tag transmitting and receiving antennas.

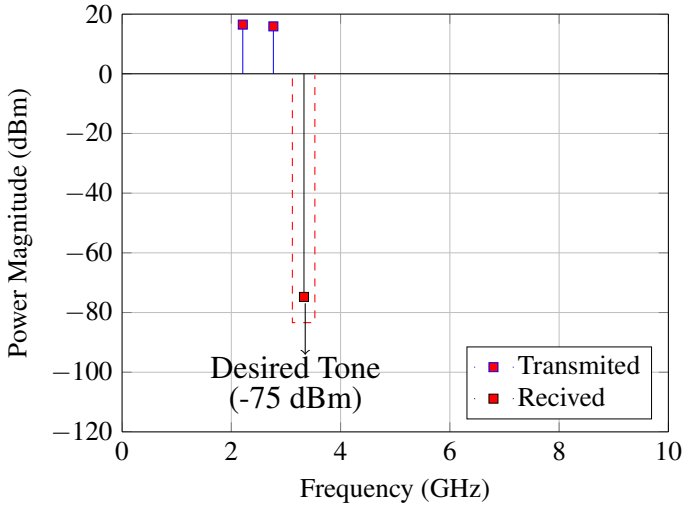

Figure 5.28: Inter-modulation based tag response illustrating that the upper inter-modulated component is maximally transmitted from the tag towards the reader.

5.6 Phase Encoding Schemes

In this section, the possibility of encoding data in the relative phase difference between the exploited nonlinear diode products is presented. Thus, the relative phase encoding can be applied on the generated harmonics, mixed or inter-modulated tones. The presented phase modulation scheme is illustrated in Fig.5.29, where the generated second harmonic tone undergoes a relative phase shifter that produces at the end two similar tones with 180° phase difference. However, these different phase states can take any other values. Therefore, the coding capacity and the detection robustness are enhanced.

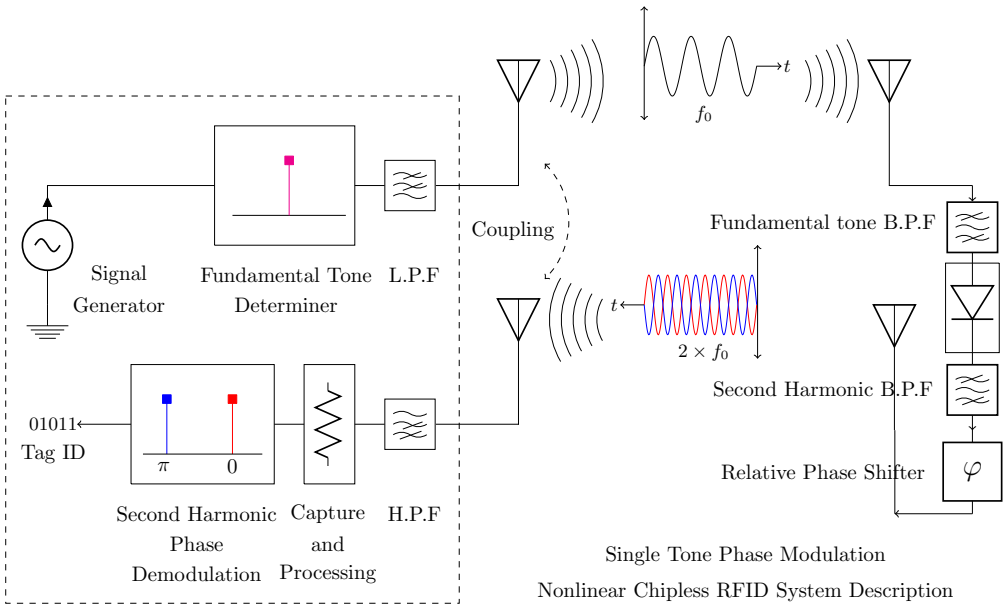

Figure 5.29: Nonlinear phase modulation system description.

The designed phase shifter is implemented in CST design studio. This phase shifter consists of a power splitter that divides the generated tones in a two distinct paths with appropriate lengths. One of these paths is directly radiated by the corresponding tag transmitting antenna. While the other splitted tone is delayed using a particular transmission line length that produces a predetermined relative phase difference with respect to the other tone. Lastly, the generated phase modulated signals are introduced, where the presented two phase states are 0° and 180° as illustrated in Fig.5.30.

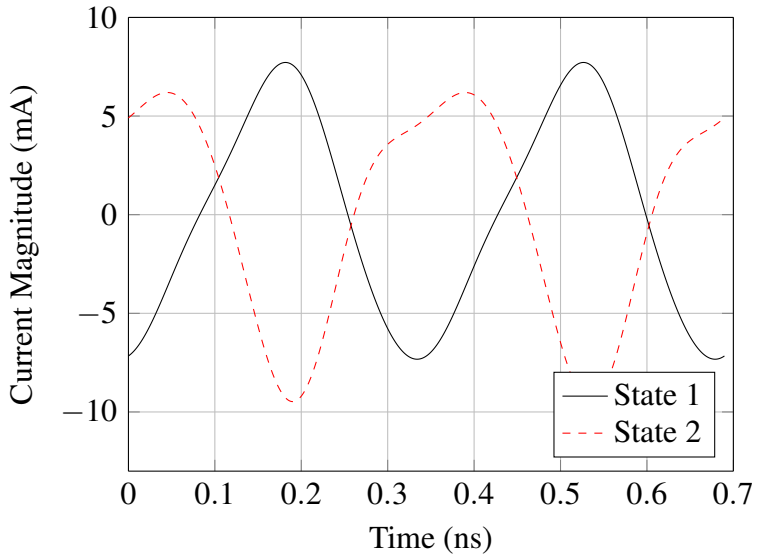

Figure 5.30: Simulated real time signals illustrating a relative phase difference of 180° for the designed transmission line paths.

5.7 Conclusion

In this chapter, novel nonlinear chipless RFID tags are demonstrated. First, the single tone harmonic radar tags are introduced. In this category, the tag receiving antenna is tuned at a predetermined fundamental tone which is conveyed to the tag integrated diode to generate the corresponding harmonics. Hence, the second harmonic is figured out by the tag transmitting antenna which is re-radiated towards the reader representing the tag-ID. Afterward, the multi-tone harmonic radar tags are presented. In this regard, the tags are interrogated with a prescribed set of fundamental tones which are swept over the time in the reader side to avoid the generation of their mixing products in the reader and tag as well. The multi-bit harmonic radar tag consists of receiving antenna, the multi-stop band filter, diode, the same multi-stop band filter and transmitting antenna. First, the tag receiving antenna delivers the fundamental interrogation tones to the first multi-stop band filter that prohibits the retransmission of the diode reverse leakage. Then, these fundamentals are conveyed to the single unbiased diode which performs the frequency conversion. These converted tones are passed through the second multi-stop band filter which implements the NPM in the second harmonic of these fundamentals. Hence, the tag transmitting antenna radiates the second harmonic frequencies. Therefore, the notches that are existing in the second harmonics are representing the tag-ID. One key feature of the multi-bit tag is that it is entirely planar based on CPW technology.

Afterward, a set of distinct frequency pairs are proposed to interrogate the nonlinear tags. The tag itself can be designed to transmit any of the generated nonlinear components maximally. Therefore, the up-converting mixer tag is introduced where the sum of these two tones is maximally generated and transmitted by the tag antenna. Then, an inter-modulation based tag is presented where the tag transmitting antenna maximally transmits the upper inter-modulated component of the interrogation pairs. The inter-modulation communication offers small frequency offset. Finally, the phase modulation capability is introduced. Therefore, not only the presence or absence of a harmonic notch or peak is used in coding the tag-ID, but also the corresponding phase state is considered.

6 CONCLUSION AND FUTURE WORK

This chapter summarizes the thesis contributions and unique features. Furthermore, a future research track is proposed.

6.1 Conclusion

The research focus of this thesis was to break through the handicaps that prevent the realization of the chipless RFID technology. The achievements that had been accomplished during the work of this dissertation are organized in three important chapters. In the first chapter, novel chipless RFID tags are developed considering the tag compactness, printing, coding capacity, operating frequency range and reading robustness. In the second chapter, novel reader antenna system is proposed for increasing the reading coverage and enhancing the detection. The third chapter exploits the nonlinear tag response to completely isolate the environmental reflections and thus improve the reading coverage. Moreover, a significant immunity against tagged item materials is acquired.

Chapter 3 focus is the chipless RFID tag where innovative physically modulated tags are presented. First, NPM printable tags with novel encoding techniques are proposed. Accordingly, the coupling between resonators is preserved while activating or deactivating a specific resonance. Moreover, the number of encoding resonators could be increased and so the coding bits without increasing the tag size. Therefore, 14-bit coding capacity is achieved for the RCS-based tags, and 18-bit coding capacity is acquired for the retransmission based tags. However, their literature counterpart, the coding capacity is less with bigger tag size and larger working frequency range. Furthermore, the orthogonal configuration of the retransmission tag antennas minimizes the cross talks between the reader interrogation antennas and also the environmental clutter reflections. After that, the notch width parameter is exploited to increase the coding capacity and enhance the coding efficiency by encoding 4-bits per single resonator. Thus, 72 coding capacity is achieved.

Moreover, a smart resonator arrangement is utilized to minimize the coupling effects. Therefore, the resonators could be adjusted independently without increasing the tag size. Afterward, the co/cross polarizing tags are introduced where the depolarized plane is exploited to increase the coding capacity. Therefore, 100 coding capacity is achieved in 3 GHz bandwidth. Up to the author's knowledge, this is the highest coding capacity that can be reached with this occupied frequency range and tag size. Furthermore, the depolarized tag response is exploited to minimize the environmental reflections and thus enhance the reading robustness. Finally, the practical feasibility of the proposed physically modulated tags is demonstrated. Table 6.1 summarizes the significant features of the proposed physically modulated tags.

Table 6.1: Summary of the proposed physically modulated chipless RFID tags

Resonator Type	Physical Modulation	No. Bits per Single Element	Tag Size (cm^2)	Coding Capacity (bits)	Coding Density ($bits/cm^2$)	Frequency Range (GHz)
Circular Ring [12]	**NPM**	**1**	**4×4**	**14**	**1.11**	**2-5**
L-Shape DGS [11]	**NPM**	**1**	**5×8**	**18**	**0.45**	**3-9**
Dipole, ring and patch [13]	**NWM**	**4**	**4.5×5**	**72**	**3.6**	**2-5**
Crossed Dipole [14]	**OO-N/P N/P-P**	**4**	**4.5×4.5**	**100**	**4.8**	**2-5**

In chapter 4, novel RA antennas are introduced to be utilized with the chipless RFID readers. The advantages of the presented high focusing beam antenna are exploited to isolate the background and thus enhance the tag detection. Furthermore, the introduced high gain RA antennas significantly increase the reading range. Special considerations are devoted to the design simplicity, enlarge the operating bandwidth, improve the spatial resolution, minimize the re-radiation losses and reduce the SLL. Hence, a wide-band RA antenna with a small feeder distance is demonstrated first. This developed prototype achieves 300 MHz bandwidth centered at 5.8 GHz. Moreover, the RA generated beam is four times narrower than the feeder beam and thus 6dB higher in gain with -10 dB SLL. The second developed prototype exploits a designed constant phase center horn antenna to feed the RA surface. Therefore, an UWB RA antenna based on double circular ring resonator cell is demonstrated. Measurements illustrate

that the FBW of the developed UWB RA antenna is 37 % covering all the feeder bandwidth and thus fulfilling the requirements of the FC chipless RFID systems. Accordingly, multiple bits accommodation is enabled. Furthermore, the radiated beam is 15° HPBW, 19 dBi gain and −10 dB SLL. Therefore, the developed UWB RA antenna is successfully integrated with the physically modulated tags and a reading range of 1 m is achieved. To the best of my knowledge, this is the highest reading range achieved in the FC chipless RFID systems, considering real-world indoor environment and software defined radio reader. Afterward, an UWB dual polarized RA is proposed to be utilized with the depolarized tags. The cross polarization isolation level is less than 40 dB. Consequently, the reading range and the detection reliability are enhanced. Finally, an electronic beam scanning RA is demonstrated to be employed in the chipless RFID reader for the first time. Therefore, the cell phases are adjusted to reconfigure the beam to the tag direction electronically. Moreover, this two-dimensional beam steering RA antenna provides large scanning range of ±50° with high resolution up to 10° and low SLL less than -10 dB.

In chapter 5, the nonlinear tags are introduced where the nonlinearity is attained by utilizing a single unbiased diode which is integrated into the tag structure. First, the single tone harmonic radar tags are introduced, where the tag is composed entirely of receiving and transmitting antennas that are connected through the diode. Thus, the tag receiving antenna is tuned at a predetermined fundamental tone which is maximally received and conveyed to the tag integrated diode to generate the corresponding harmonics. Hence, the tag transmitting antenna is matched at the relevant second harmonic which is re-radiated towards the reader representing the tag-ID. Therefore, the coding capacity is considered to be 1-bit information for each tag and thus the number of tags is based on the receiving antenna bandwidth besides the occupied coding spectrum that is reserved for the fundamental tones. Afterward, the multi-tone harmonic radar tags are presented, where a multi-bit information could be encoded. In this regard, the tags are interrogated with a prescribed set of fundamental tones which are swept over the time in the reader side to avoid the generation of their mixing products in the reader and tag as well. The multi-bit harmonic radar tag consists of receiving antenna, the multi-stop band filter, diode, the same multi-stop band filter and transmitting antenna. First, the tag receiving antenna delivers the fundamental interrogation tones to the first multi-stop band filter that prohibits the retransmission of the diode reverse leakage. Then, these fundamentals are conveyed to the single unbiased diode which performs the frequency conversion. These converted tones are passed through the second multi-stop band filter which implements the NPM in the second harmonic of these fundamentals. Hence, the tag transmitting antenna radiates the encoded second harmonic frequencies. Therefore,

the notches that exist in the second harmonics are representing the tag-ID. One key feature of the multi-bit tag is that it is completely planar based on the CPW technology.

Afterward, a set of distinct frequency pairs is exploited to interrogate the nonlinear tags. The tag itself is designed to maximally receives one of these two co-located frequency pairs and convey them to the integrated diode. The diode, in turn, generates the corresponding nonlinear combinations. Afterward, the tag transmitting antenna figures out one of these nonlinear products. In this regard, the up-converting mixer tag is introduced, where the exploited mixed sum leads to a smaller tag transmitting antenna. Hence, the combined sum of the two interrogation tones is maximally transmitted by the tag transmitting antenna. Afterward, the inter-modulation based tags are presented aiming at reducing the occupied frequency span. In this concern, the upper inter-modulated component of the interrogation pairs is maximally transmitted by the tag transmitting antenna representing the tag-ID. Lastly, the relative phase encoding is exploited to increase the coding capacity and enhance the tag detection. Hence, the relative phase differences enable utilizing a single tone to include different phase states and thus the coding capacity is increased. Therefore, not only the presence or absence of a harmonic notch or peak is utilized in encoding the tag-ID, but also the corresponding relative phase is considered.

The unique contributions presented in the thesis and the corresponding realized testbeds lead to significant advancement in the chipless RFID systems.

6.2 Future Work

This section summarizes the future research work trends in these subsequent points:

1. **Sensing:** The concept of a thing applies to the chipless RFID tags that are introduced in the thesis. Therefore, the technology will not be limited to object identification, but it will strongly participate in the upcoming IoT technology. Hence, the tag can be developed to relay physical information of the environment such as temperature, humidity, pressure, water level and so on.

2. **3-D angularly stable, ultra-long-range and bendable tag:** The concept of 3-D angularly stable is to have a tag with isotropic radiation pattern, which is independent on the angles of interrogation. However, the tag radiation pattern is directive and the directivity increase with frequency and also with the number of encoding resonators. One idea to present 2-D angular stable radiation pattern is to apply the Van-Atta Reflectarray concept, where

the tag backscatters in the same direction of the incident wave. Therefore, the tag can provide immunity against bending and the reading range can be further increased with the inclusion of multiple antennas in the tag side.

3. **Reader development:** Developing chipless RFID reader is of great interest, in order to precisely detect the tag-ID in noisy environments. This aspired reader is also capable of communication with the nonlinear tags. To this aim, the reader components are important to operate linearly, the oscillator transmitting and receiving channels important to be isolated to avoid the local leakage. Therefore, the reading coverage can be enhanced while exploiting the signal processing and detection techniques.

LIST OF PUBLICATIONS AND AWARDS

Publications derived from this dissertation

The following list of publications are derived from the results presented in this dissertation.

Journal Papers

[1] **M. Khaliel**, A. El-Awamry, A. Fawky, and T. Kaiser, " A Novel Design Approach for Co/Cross-Polarizing Chipless RFID Tags of High Coding Capacity, " *IEEE Journal of Radio Frequency Identification (Volume: PP, Issue: 99),* Oct. 2017.

[2] **M. Khaliel**, A. El-Awamry, A. Fawky, and T. Kaiser, " Long Reading Range for the Frequency Coded Chipless RFID System Based on Reflectarray Antennas, " *International Journal of Microwave and Wireless Technologies (Major Revesion Round),* Nov. 2017.

[3] A. El-Awamry, **M. Khaliel**, A. Fawky, and T. Kaiser, " Adaptive Spectrum Scanning Techniques for Reducing the Identification Time of the Frequency Coded Chipless RFID System, " *Transactions on Emerging Telecommunications Technologies (DOI: 10.1002/ett.3173),* March 2017.

[4] M. Elhadidy, A. El-Awamry, **M. Khaliel**, A. Fawky, and T. Kaiser, " Real-World Testbed for Multi-Tag UWB Chipless RFID System based on a Novel Collision Avoidance MAC Protocol, " *Transactions on Emerging Telecommunications Technologies (DOI: 10.1002/ett.3124),* Oct. 2017.

Conference Papers

[1] **M. Khaliel**, A. El-Awamry, A. Fawky, and T. Kaiser, " Long reading range chipless RFID system based on reflectarray antennas, " *European Conference on Antennas and Propagation (EuCAP), Paris, France,* 2017.

[2] **M. Khaliel**, A. Fawky, A. El-Awamry, Abd-Elhady Mahmoud, and T. Kaiser, " Printable, high coding capacity chipless RFID tags for low-cost item tagging, " *IEEE International Conference on Networking, Sensing, and Control (ICNSC), Calabria, Italy,* 2017.

[3] A. Fawky, A. El-Awamry, **M. Khaliel**, and T. Kaiser, " Novel notch detection techniques for Frequency Coded chipless RFID, " *IEEE International Conference on Networking, Sensing, and Control (ICNSC), Calabria, Italy,* 2017.

[4] A. El-Awamry, A. Fawky, **M. Khaliel**, and T. Kaiser, " A novel adaptive spectrum scanning technique for reducing the identification time of the UWB chipless RFID system, " *IEEE International Conference on Networking, Sensing, and Control (ICNSC), Calabria, Italy,* 2017.

[5] A. Fawky, **M. Khaliel**, A. El-Awamry, and T. Kaiser, " Frequency coded chipless RFID tag localization using multiple antennas, " *European Conference on Antennas and Propagation (EuCAP), Paris, France,* 2017.

[6] A. El-Awamry, **M. Khaliel**, A. Fawky, and T. Kaiser, " A novel multi-tag identification technique for frequency coded chipless RFID systems based on look-up-table approach, " *European Conference on Antennas and Propagation (EuCAP), Paris, France,* 2017.

[7] A. El-Awamry, **M. Khaliel**, A. Fawky, M. El-Hadidy, and T. Kaiser, " Novel notch modulation algorithm for enhancing the chipless RFID tags coding capacity, " *IEEE International Conference on RFID, San Diego, CA,* 2015, pp. 25-31.

[8] A. Fawky, **M. Khaliel**, A. El-Awamry, M. El-Hadidy, and T. Kaiser, " Novel pseudo-noise coded chipless RFID system for clutter removal and tag detection, " *IEEE International Conference on RFID, San Diego, CA,* 2015, pp. 100-104.

[9] K. Hasan, **M. Khaliel**, M. El-Hadidy, and T. Kaiser, " Design an adaptive electronically beamsteering reflectarray antenna for RFID systems, " *IEEE International Symposium on Antennas and Propagation USNC/URSI National Radio Science Meeting, Vancouver, BC,* 2015, pp. 2157-2158.

[10] **M. Khaliel**, A. El-Awamry, A. Fawky, M. El-Hadidy, and T. Kaiser, " A novel co/cross-polarizing chipless RFID tags for high coding capacity and robust detection, " *IEEE International Symposium on Antennas and Propagation USNC/URSI, National Radio Science Meeting, Vancouver, BC,* 2015, pp. 159-160.

[11] **M. Khaliel**, M. El-Hadidy, and T. Kaiser, “ Printable depolarizing chipless RFID tag based on DGS resonators for suppressing the clutter effects, " *European Conference on Antennas and Propagation (EuCAP), Lisbon,* 2015, pp. 1-5.

[12] M. El-Hadidy, A. El-Awamry, A. Fawky, **M. Khaliel**, and T. Kaiser, “ A novel collision avoidance MAC protocol for multi-tag UWB chipless RFID systems based on Notch Position Modulation, " *European Conference on Antennas and Propagation (EuCAP), Lisbon,* 2015, pp. 1-5.

[13] A. El-Awamry, **M. Khaliel**, A. Fawky, M. El-Hadidy, and T. Kaiser, “ Novel adaptive sliding window algorithm reducing latency for multi-tag chipless RFID systems, " *International Symposium on Antennas and Propagation USNC/URSI, National Radio Science Meeting, Vancouver, BC,* 2015, pp. 206-206.

[14] B. Nagy, A. Fawky, **M. Khaliel**, M. El-Hadidy, and T. Kaiser, “ MISO beamforming for RFID systems via second-order cone programming, " *European Conference on Antennas and Propagation (EuCAP), The Hague,* 2014, pp. 2808-2811.

[15] A. Fawky, **M. Khaliel**, M. El-Hadidy, and T. Kaiser, “ UWB chipless RFID system performance based on real world 3D-deterministic channel model and ZF equalization, " *European Conference on Antennas and Propagation (EuCAP), The Hague,* 2014, pp. 2808-2811.

[16] **M. Khaliel**, A. Fawky, M. El-Hadidy, and T. Kaiser, “ UWB Reflectarray antenna for chipless RFID applications, " *31st National Radio Science Conference (NRSC), Cairo,* 2014, pp. 17-20.

[17] M. El-Hadidy, B. Nagy, A. Fawky, **M. Khaliel**, and T. Kaiser, “ Evaluation of UWB chipless RFID system performance considering indoor multipath propagation channel and real world aspects, " *Progress In Electromagnetic Research (PIERS) Proceedings, Stockholm,* August 12-15, 2013, pp.616 - 620.

[18] M. El-Hadidy, B. Nagy, **M. Khaliel**, A. Fawky, and T. Kaiser, “ Novel Methodology for increasing the reading range of the UWB passive RFID chipless tags considering power regulations, " *Progress In Electromagnetic Research (PIERS) Proceedings, Stockholm,* August 12-15, 2013, pp.630 - 632.

Organized IEEE Workshops

[1] "Chipless RFID Future and Challenges," 2015 9th European Conference on Antennas and Propagation (EuCAP), Lisbon, 2015

[2] "Chipless RFID System and Testbed: Reader and Tag Antennas, Reader and Tag Design, Multi-Tag Scenarios, Modulation, Clutter Effects and Channel Estimation, Signaling and Real-world Testbed," Radio Science Meeting (Joint with AP-S Symposium), 2015 USNC-URSI, Vancouver, BC, Canada, 2015

Awards

1. Awarded a three year Deutscher Akademischer Austauschdienst (DAAD) PhD. student scholarship under the Deutsch-Arabische Forschungspartnerschaft program grants in ID4EGYPT Project.

2. **Best paper award** of the 15th IEEE International Conference on Communications Systems (ICCS 2016) with the paper entitled "Wideband Hybrid Analog-Digital Beamforming Massive MIMO Systems Based on Rotman Lens".

3. The paper "Long Reading Range Chipless RFID System Based on Reflectarray Antennas," is nominated for the **best student paper award** of the 11th European Conference on Antennas and Propagation (EuCAP) conference 2017.

4. The paper "A Novel Collision Avoidance MAC Protocol for Multi-Tag UWB Chipless RFID Systems based on Notch Position Modulation," is nominated for the **best student paper award** of the 9th European Conference on Antennas and Propagation (EuCAP) conference 2015.

Related work by the author

1. Y. Gao, **M. Khaliel**, Feng Zeng, and T. Kaiser, " Rotman Lens Based Hybrid Analog-Digital Beamforming in Massive MIMO Systems: Array Architectures, Beam Selection Algorithms and Experiments, " *IEEE Transactions on Vehicular Technology (Volume: 66, Issue: 10)* Oct. 2017.

2. Y. Gao, **M. Khaliel**, and T. Kaiser, “ Wideband hybrid analog-digital beamforming massive MIMO systems based on Rotman lens, " *IEEE International Conference on Communication Systems (ICCS), Shenzhen, China, 2016.*

3. S. EL-Rabaie, H. A. Sharshar, M. Yassien, and **M. Khaliel**, “ Minutarized metamaterial narrow bandpass filters using CRLH transmission line CL – loaded approach, " *Minoufia Journal of Electronic Engineering Research (MJEER), Janauary 2012, Vol.22, No. 1*

4. S. EL-Rabaie, H. A. Sharshar, M. Yassien, and **M. Khaliel**, “ Investigation to metamaterial transmission line filters based on the CL-loaded approach, " *Minoufia Journal of Electronic Engineering Research (MJEER), Janauary 2012, Vol.22, No. 1.*

BIBLIOGRAPHY

[1] M. M. Khan, F. A. Tahir, M. F. Farooqui, A. Shamim, and H. M. Cheema, "$3.56 - bits/cm^2$ compact inkjet printed and application specific chipless rfid tag," *IEEE Antennas and Wireless Propagation Letters*, vol. 15, pp. 1109–1112, 2016.

[2] A. Attaran and R. Rashidzadeh, "Chipless radio frequency identification tag for iot applications," *IEEE Internet of Things Journal*, vol. 3, no. 6, pp. 1310–1318, Dec 2016.

[3] A. Fawky, M. Khaliel, A. El-Awamry, M. El-Hadidy, and T. Kaiser, "Novel pseudo-noise coded chipless rfid system for clutter removal and tag detection," in *RFID (RFID), 2015 IEEE International Conference on*, April 2015, pp. 100–104.

[4] M. El-Hadidy, A. El-Awamry, A. Fawky, M. Khaliel, and T. Kaiser, "A novel collision avoidance mac protocol for multi-tag uwb chipless rfid systems based on notch position modulation," in *Antennas and Propagation (EuCAP), 2015 9th European Conference on*, April 2015, pp. 1–5.

[5] Rubayet-E-Azim, N. Karmakar, and E. Amin, "Short time fourier transform (stft) for collision detection in chipless rfid systems," in *2015 International Symposium on Antennas and Propagation (ISAP)*, Nov 2015, pp. 1–4.

[6] R. Rezaiesarlak and M. Manteghi, "A new anti-collision algorithm for identifying chipless rfid tags," in *2013 IEEE Antennas and Propagation Society International Symposium (APSURSI)*, July 2013, pp. 1722–1723.

[7] R. E. A. Anee and N. C. Karmakar, "Anti-collision methods for chipless rfid systems," in *2015 Asia-Pacific Microwave Conference (APMC)*, Dec 2015, vol. 2, pp. 1–3.

[8] S. Dey, J. K. Saha, and N. C. Karmakar, "Smart sensing: Chipless rfid solutions for the internet of everything," *IEEE Microwave Magazine*, vol. 16, no. 10, pp. 26–39, Nov 2015.

[9] R. Rezaiesarlak and M. Manteghi, *Chipless Rfid: Design Procedure and Detection Techniques*, Springer, 2014.

[10] N. Karmakar, *Design of Portable Smart Antenna System for RFID Reader: A New Approach*, pp. 301–316, Wiley-IEEE Press, 2010.

[11] M. Khaliel, M. El-Hadidy, and T. Kaiser, "Printable depolarizing chipless rfid tag based on dgs resonators for suppressing the clutter effects," in *Antennas and Propagation (EuCAP), 2015 9th European Conference on*, April 2015, pp. 1–5.

[12] A. Fawky, M. Khaliel, A. El-Awamry, M. El-Hadidy, and T. Kaiser, "Novel pseudo-noise coded chipless rfid system for clutter removal and tag detection," in *RFID (RFID), 2015 IEEE International Conference on*, April 2015, pp. 100–104.

[13] A. El-Awamry, M. Khaliel, A. Fawky, M. El-Hadidy, and T. Kaiser, "Novel notch modulation algorithm for enhancing the chipless rfid tags coding capacity," in *RFID (RFID), 2015 IEEE International Conference on*, April 2015, pp. 25–31.

[14] M. Khaliel, A. El-Awamry, A. Fawky, M. El-Hadidy, and T. Kaiser, "A novel co/cross-polarizing chipless rfid tags for high coding capacity and robust detection," in *Antennas and Propagation USNC/URSI National Radio Science Meeting, 2015 IEEE International Symposium on*, July 2015, pp. 159–160.

[15] M. Popperl, C. Carlowitz, M. Vossiek, C. Mandel, and R. Jakoby, "An ultra-wideband time domain reflectometry chipless rfid system with higher order modulation schemes," in *2016 German Microwave Conference (GeMiC)*, March 2016, pp. 401–404.

[16] O. M. Haraz, M. Ashraf, S. Alshebili, M. R. AlShareef, and H. M. Behairy, "Uwb monopole antenna chipless rfid tags using 8-bit open circuit stub resonators," in *2016 21st International Conference on Microwave, Radar and Wireless Communications (MIKON)*, May 2016, pp. 1–4.

[17] M. Schueler, C. Mandel, M. Puentes, and R. Jakoby, "Metamaterial inspired microwave sensors," *Microwave Magazine, IEEE*, vol. 13, no. 2, pp. 57–68, March 2012.

[18] S. Preradovic, I. Balbin, N.C. Karmakar, and G.F. Swiegers, "Multiresonator-based chipless rfid system for low-cost item tracking," *Microwave Theory and Techniques, IEEE Transactions on*, vol. 57, no. 5, pp. 1411–1419, May 2009.

[19] B. Nikfal and C. Caloz, "Hybrid time-frequency rfid system," in *Microwave Symposium Digest (MTT), 2012 IEEE MTT-S International*, June 2012, pp. 1–3.

[20] A. Vena, E. Perret, and S. Tedjini, "Rfid chipless tag based on multiple phase shifters," in *Microwave Symposium Digest (MTT), 2011 IEEE MTT-S International*, June 2011, pp. 1–4.

[21] S. Genovesi, F. Costa, A. Monorchio, and G. Manara, "Chipless rfid tag exploiting multi-frequency delta-phase quantization encoding," *IEEE Antennas and Wireless Propagation Letters*, vol. 15, pp. 738–741, 2016.

[22] A. Vena, A.A. Babar, L. Sydanheimo, M.M. Tentzeris, and L. Ukkonen, "A novel near-transparent ask-reconfigurable inkjet-printed chipless rfid tag," *Antennas and Wireless Propagation Letters, IEEE*, vol. 12, pp. 753–756, 2013.

[23] O. Rance, R. Siragusa, P. Lemaître-Auger, and E. Perret, "Toward rcs magnitude level coding for chipless rfid," *IEEE Transactions on Microwave Theory and Techniques*, vol. PP, no. 99, pp. 1–11, 2016.

[24] C.M. Nijas, U. Deepak, P.V. Vinesh, R. Sujith, S. Mridula, K. Vasudevan, and P. Mohanan, "Low-cost multiple-bit encoded chipless rfid tag using stepped impedance resonator," *Antennas and Propagation, IEEE Transactions on*, vol. 62, no. 9, pp. 4762–4770, Sept 2014.

[25] M. Polivka, J. Havlicek, M. Svanda, and J. Machac, "Improvement in robustness and recognizability of rcs response of u shaped strip-based chipless rfid tags," *IEEE Antennas and Wireless Propagation Letters*, vol. PP, no. 99, pp. 1–1, 2016.

[26] T. Noor, A. Habib, Y. Amin, J. Loo, and H. Tenhunen, "High-density chipless rfid tag for temperature sensing," *Electronics Letters*, vol. 52, no. 8, pp. 620–622, 2016.

[27] F. Costa, A. Monorchio, and G. Manara, "An equivalent-circuit modeling of high impedance surfaces employing arbitrarily shaped fss," in *Electromagnetics in Advanced Applications, 2009. ICEAA '09. International Conference on*, Sept 2009, pp. 852–855.

[28] F. Costa, S. Genovesi, and A. Monorchio, "A chipless rfid based on multiresonant high-impedance surfaces," *IEEE Transactions on Microwave Theory and Techniques*, vol. 61, no. 1, pp. 146–153, Jan 2013.

[29] M.A. Islam, Y. Yap, N. Karmakar, and A.K.M. Azad, "Orientation independent compact chipless rfid tag," in *RFID-Technologies and Applications (RFID-TA), 2012 IEEE International Conference on*, Nov 2012, pp. 137–141.

[30] M.S. Bhuiyan, A. Azad, and N. Karmakar, "Dual-band modified complementary split ring resonator (mcsrr) based multi-resonator circuit for chipless rfid tag," in *Intelligent Sensors, Sensor Networks and Information Processing, 2013 IEEE Eighth International Conference on*, April 2013, pp. 277–281.

[31] Y.F. Weng, S.W. Cheung, T.I. Yuk, and L. Liu, "Design of chipless uwb rfid system using a cpw multi-resonator," *Antennas and Propagation Magazine, IEEE*, vol. 55, no. 1, pp. 13–31, Feb 2013.

[32] S. Preradovic, S. Roy, and N. Karmakar, "Fully printable multi-bit chipless rfid transponder on flexible laminate," in *Microwave Conference, 2009. APMC 2009. Asia Pacific*, Dec 2009, pp. 2371–2374.

[33] M. A. Matin, *Ultra Wideband - Current Status and Future Trends*, InTech, 2012-10-03.

[34] K.P. Ray and Y. Ranga, "Ultrawideband printed elliptical monopole antennas," *Antennas and Propagation, IEEE Transactions on*, vol. 55, no. 4, pp. 1189–1192, April 2007.

[35] Chaozhu Zhang, Jing Zhang, and Lin Li, "Triple band-notched uwb antenna based on sir-dgs and fork-shaped stubs," *Electronics Letters*, vol. 50, no. 2, pp. 67–69, January 2014.

[36] A.N. Ghazali and S. Pal, "Microstrip based uwb filter with controllable multiple notches and extended upper stopband," in *Emerging Trends in Communication, Control, Signal Processing Computing Applications (C2SPCA), 2013 International Conference on*, Oct 2013, pp. 1–5.

[37] A. Liu, *Rf Mems Switching and Integrated Switching Circuits: Microsystems, Import*, Springer-Verlag, Berlin, Heidelberg, 2007.

[38] Mohamed El-Hadidy, Ahmed El-Awamry, Abdelfattah Fawky, Maher Khaliel, and Thomas Kaiser, "Real-world testbed for multi-tag uwb chipless rfid system based on a novel collision avoidance mac protocol," *Transactions on Emerging Telecommunications Technologies*, vol. 27, no. 12, pp. 1707–1714, 2016, ett.3124.

[39] Ettus Research, "Universal Software Radio Peripheral[online]. available:," 2016.

[40] Ettus Research, "USRP-RF Daughter Board. [online]. available:," 2016.

[41] A. El-Awamry, A. Fawky, M. El-Hadidy, and T. Kaiser, "Smart notch detection techniques for robust frequency coded chipless rfid systems," in *2015 9th European Conference on Antennas and Propagation (EuCAP)*, May 2015, pp. 1–5.

[42] A. Vena, E. Perret, and S. Tedjni, "A depolarizing chipless rfid tag for robust detection and its fcc compliant uwb reading system," *IEEE Transactions on Microwave Theory and Techniques*, vol. 61, no. 8, pp. 2982–2994, Aug 2013.

[43] M. Khaliel, A. Fawky, M. El-Hadidy, and T. Kaiser, "Uwb reflectarray antenna for chipless rfid applications," in *Radio Science Conference (NRSC), 2014 31st National*, April 2014, pp. 17–20.

[44] Khaled Hasan, Maher Khaliel, Mohamed El-Hadidy, and Thomas Kaiser, "Design an adaptive electronically beamsteering reflectarray antenna for rfid systems," in *Antennas and Propagation USNC/URSI National Radio Science Meeting, 2015 IEEE International Symposium on*, July 2015, pp. 2157–2158.

[45] Mohamed El-Hadidy, B. Nagy, M. Khaliel, A. Fawky, E. Abdallah, H. Elhennawy, and Thomas Kaiser, "Novel methodology for increasing the reading range of the uwb passive rfid chipless tags considering power regulations," *PIERS 2013 Stockholm: Paris, France, 1 - 4 April 2012August 12-15, 2013 Stockholmproceedings*, 2013.

[46] FCC UWB regulations part 15, "Federal communications commission, da 07-198, 47 c.f.r. §§ 15.511 and 15.521(g, washington, d.c. 20554.," 26 January 2007.

[47] John Huang and José A. Encinar, "Reflectarray antennas," in *John Wiley & Sons, Inc.*, 2008.

[48] J. Shaker, M.R. Chaharmir, and J. Ethier, *Reflectarray Antennas: Analysis, Design, Fabrication, and Measurement:*, Antennas and Propagation. Artech House, 2013.

[49] Lu Guo, Peng-Khiang Tan, and Tan-Huat Chio, "Design of an x-band reflectarray using double circular ring elements," in *Antennas and Propagation (EuCAP), 2013 7th European Conference on*, 2013, pp. 2947–2950.

[50] R. Florencio, J.A. Encinar, R.R. Boix, V. Losada, and G. Toso, "Reflectarray antennas for dual polarization and broadband telecom satellite applications," *Antennas and Propagation, IEEE Transactions on*, vol. 63, no. 4, pp. 1234–1246, April 2015.

[51] P. Nayeri, Fan Yang, and A.Z. Elsherbeni, "Bifocal design and aperture phase optimizations of reflectarray antennas for wide-angle beam scanning performance," *Antennas and Propagation, IEEE Transactions on*, vol. 61, no. 9, pp. 4588–4597, 2013.

[52] F. Venneri, S. Costanzo, and G. Di Massa, "Design and validation of a reconfigurable single varactor-tuned reflectarray," *Antennas and Propagation, IEEE Transactions on*, vol. 61, no. 2, pp. 635–645, 2013.

[53] S.V. Hum, M. Okoniewski, and R.J. Davies, "Realizing an electronically tunable reflectarray using varactor diode-tuned elements," *Microwave and Wireless Components Letters, IEEE*, vol. 15, no. 6, pp. 422–424, 2005.

[54] L. Boccia, G. Amendola, and G. Di Massa, "Performance improvement for a varactor-loaded reflectarray element," *Antennas and Propagation, IEEE Transactions on*, vol. 58, no. 2, pp. 585–589, 2010.

[55] Constantine A. Balanis, *Antenna Theory: Analysis and Design*, Wiley-Interscience, 2005.

[56] A. Ludwig, "The definition of cross polarization," *IEEE Transactions on Antennas and Propagation*, vol. 21, no. 1, pp. 116–119, Jan 1973.

[57] Zuo-Min Tsai, Pei-Hung Jau, Nai-Chung Kuo, Jui-Chi Kao, Kun-You Lin, Fan-Ren Chang, En-Cheng Yang, and Huei Wang, "A high-range-accuracy and high-sensitivity harmonic radar using pulse pseudorandom code for bee searching," *Microwave Theory and Techniques, IEEE Transactions on*, vol. 61, no. 1, pp. 666–675, Jan 2013.

[58] B. Kubina, J. Romeu, C. Mandel, M. Schussler, and R. Jakoby, "Harmonic chipless sensor exploiting wireless autonomous communication and energy transfer," in *Wireless Power Transfer Conference (WPTC), 2014 IEEE*, May 2014, pp. 24–27.

[59] V. Palazzi, F. Alimenti, P. Mezzanotte, M. Virili, C. Mariotti, G. Orecchini, and L. Roselli, "Low-power frequency doubler in cellulose-based materials for harmonic rfid applications," *Microwave and Wireless Components Letters, IEEE*, vol. 24, no. 12, pp. 896–898, Dec 2014.

[60] C. Mariotti, F. Alimenti, M. Virili, G. Orecchini, P. Mezzanotte, and L. Roselli, "Harmonic chipless sensor exploiting wireless autonomous communication and energy transfer," in *Wireless Power Transfer Conference (WPTC), 2014 IEEE*, May 2014, pp. 24–27.

[61] K. Rasilainen, J. Ilvonen, A. Lehtovuori, J.-M. Hannula, and V. Viikari, "On design and evaluation of harmonic transponders," *Antennas and Propagation, IEEE Transactions on*, vol. 63, no. 1, pp. 15–23, Jan 2015.

[62] Y. Dong and T. Itoh, "Metamaterial-based antennas," *Proceedings of the IEEE*, vol. 100, no. 7, pp. 2271–2285, July 2012.

[63] Kai Fong Lee, *Microstrip patch antennas*, Imperial College Press [u.a.], London [u.a.].